SUPPORTING INFORMATION

Data-Driven Pursuit of Electrochemically Stable 2D Materials with Basal Plane Activity toward Oxygen Electrocatalysis

Xiangyu Guo[a,d,g,h], Shengli Zhang[b,*], Liangzhi Kou[f], Chi Yung Yam[d,e,j], Thomas Frauenheim[d,e,i], Zhongfang Chen[c,*], Shiping Huang[a,*]

[a] State Key Laboratory of Organic–Inorganic Composites, Beijing University of Chemical Technology, Beijing 100029, China

[b] MIIT Key Laboratory of Advanced Display Materials and Devices, Ministry of Industry and Information Technology, Institute of Optoelectronics & Nanomaterials, Nanjing University of Science and Technology, Nanjing 210094, China

[c] Department of Chemistry, University of Puerto Rico, Rio Piedras, San Juan, Puerto Rico 00931, United States

[d] Beijing Computational Science Research Center (CSRC), Beijing 100193, China

[e] Shenzhen JL Computational Science and Applied Research Institute, Shenzhen 518110, China

[f] School of Mechanical, Medical and Process Engineering, Queensland University of Technology, QLD, 4000, Australia

[g] Bremen Center for Computational Materials Science, University of Bremen, Bremen 28359, Germany

[h] Institute for Functional Intelligent Materials, National University of Singapore, Singapore, 117544, Singapore

[i] School of Science, Constructor University, Bremen 28759, Germany

[j] Shenzhen Institute for Advanced Study, University of Electronic Science and Technology of China, Shenzhen, 518000, China

Corresponding E-mails:

E-mail: zhongfangchen@gmail.com

E-mail: zhangslvip@njust.edu.cn

E-mail: huangsp@mail.buct.edu.cn

Supplementary Summary

Data availability

Atomic structures used in this study will be provided at the following GitHub repository: https://github.com/ChaunceyGuo?tab=repositories

Computational methods

Spin-polarized first-principles calculations were carried out using the Perdew−Burke−Ernzerhof (PBE) functional within the generalized gradient approximation (GGA), [1] as implemented in Vienna Ab Initio Simulation Package (VASP). [2] The valence electrons were expanded as plane wave with a kinetic energy cutoff of 400 eV. The convergence thresholds were set as 1.0×10^{-5} for energy and 2.0×10^{-2} eV Å^{-1} for atomic force. The Brillouin zone was sampled by Monkhorst−Pack mesh using *k*−points of 0.04*2π Å^{-1} which was achieved by the pre-and post-processing program of VASKIT. [3] To eliminate the periodic interactions between the adjacent images, a vacuum space of 15 Å was used in the perpendicular direction of the 2D plane, and a supercell scheme was adopted when a unit cell has a lattice less than 6 Å to minimize the periodic interactions between reaction species. To describe the van der Waals interactions, DFT-D3 method with the standard parameters by Grimme *et al*. was employed. [4]

Electronic transport property of electrical conductivity ($\sigma_{\alpha\beta}$) was calculated by combining ab initio band structures and Boltzmann transport theory within the constant relaxation time approximation. This procedure solves Boltzmann equation by interpolating a band structure and implementing the required integrations, whose accuracy was demonstrated earlier. [5] Here, the relaxation time was set as 3.0 10^{-13} s following the previous work. [6] The K-Spacing Value during this calculation is set to be 0.005*2π Å^{-1}. The $\sigma_{\alpha\beta}$ a function of temperature (T) and chemical potential (μ) described as:

$$\sigma_{\alpha\beta}\ (\mathrm{T}, \mu) = \frac{1}{\Omega}\int \sigma_{\alpha\beta}(\varepsilon)\left[-\frac{\partial f_{\mu}(T,\varepsilon)}{\partial \varepsilon}\right] d\varepsilon$$

where Ω represents the volume of the unit cell. f_{μ} is the Fermi distribution, ε is the band energy which obtained from computed band structure.

The free energy landscapes and reaction pathways along the oxygen electrocatalysis on the basal plane of 2D materials were investigated in conjunction with the computational hydrogen electrode (CHE) model. [7] The vibrational contributions, including zero-point energy, enthalpy, and entropy, were obtained by the harmonic approximation at a temperature of 298.15 K. Since the current computational framework is difficult

to describe low-frequency modes properly, we set up a threshold value of 50 cm^{-1} to reduce these unphysically large entropy contributions. [8, 9] Solvation-induced energy change for the adsorption of reaction species, i.e., OOH*, O* and OH*, were considered according to the previous investigations, which were estimated to be 0.3, 0.0, and 0.3 eV, respectively. [10-12] This correction is based on the fact that each H_2O in the liquid phase can create two donors and one acceptor hydrogen bonds with adjacent molecules, which stabilize the molecules by ~0.45 (3*0.15) eV. As OOH* and OH* are able to create two hydrogen bonds with H_2O, it will be stabilized by ~0.3 eV when solvated. And no clear hydrogen bonds were formed around the O* sites, hence no correction was applied for O* adsorption. To verify the effectiveness of this correction, we have also adopted an implicit solvation model[13] to calculate the adsorption free energy of oxygen containing species using the $NbSe_2$ as prototype (see Fig. S69). The computational results obtained from these two methods are close to each other, which indicate the current calculations could well capture the reaction profiles and thus estimate the catalytic performance.

To well evaluate the electrochemical stability of 2D materials, we performed grand-canonical density functional theory (GC-DFT) computations to model the electrode−electrolyte interface under the specific electrode potential, as implemented in JDFTx. [14] We employed the PBE exchange correlation functional with GBRV ultrasoft pseudopotentials[15] at a kinetic energy cutoff of 20 Hartrees (*ca*. 544 eV) for wavefunctions and 100 Hartrees for the charge density. The charge-asymmetric nonlocally determined local-electric (CANDLE) solvation model was utilized to describe the effect of liquid water. [16] The ionic screening of net charges caused by the constant electrode potential was realized with 1M (mol L^{-1}) Na^+ and F^- components in the fluid model, which displayed high accuracy in capturing the solvation of highly charged negative and positive solutes. [17] Other numerical parameters, including *k*-point sampling, cell sizes, convergence criteria, *etc*. are similar to the VASP calculations.

Decomposition energy and exfoliation energy

The decomposition energy and the exfoliation energy were extracted from 2DMatPedia database. The exfoliation energy (E_{exf}), defined as the average energy per atom required to remove a layer from a layered bulk material, was calculated by $E_{exf} = E_{2D} - E_{bulk}$, where E_{2D} and E_{bulk} are the energies (per atom) of the 2D material and its layered bulk counterpart, respectively. The decomposition energy is defined as the energy required (per atom) to decompose a 2D material into the most stable compound(s) at its chemical composition without consideration of the corresponding layered bulk of the given 2D material.

Evaluation of the dissolution potential of materials

Under the reaction conditions with the involvement of electrolyte and external electrode potential, a material could undergo a decomposition or a dissolution depending on its redox characteristic. The dissolution potential (U_{diss}) of different sites in a material can be correlated by their thermodynamically favorable dissolution events that readily occur under acidic conditions (more details are given in Table S7). For instance, we assumed that the tellurium can be dissolved through $Te \rightarrow Te^{4+} + 4\,e^{-}$, the sulfur/selenium atoms can be changed into the sulfurous acid/selenousacid via $S/Se + 3\,H_2O \rightarrow H_2SO_3/H_2SeO_3 + 4\,H^{+} + 4\,e^{-}$, and most metals can be converted into metal ions through $M(s) \rightarrow M^{x+}(aq) + x\,e^{-}$. This is slightly different from the principle of the Pourbaix diagram. For instance, the thermodynamically favorable dissolution products of the Se and S are identified as the H_2SeO_4 and H_2SO_4, respectively. Here, the use of H_2SO_3 and H_2SeO_3 instead of H_2SeO_4 and H_2SO_4 was actually considered the possible oxidation process in the early stage. We note that elements might involve continuous oxidation steps to realize the final products. For example, Se and S will be first oxidized into XO_3^{2-} (X= S, and Se), and then coupled with the other oxygen group to form the XO_4^{2-}. Since the transformation of XO_3^{2-} into XO_4^{2-} is easy to occur due to the metastable nature of XO_3^{2-}. The evaluation of the oxidation process of these elements at their early stage could be more valuable to assess electrochemical stability. Thus, we selected H_2SO_3 and H_2SeO_3 as the important dissolution products of the S and Se, instead of using H_2SeO_4 and H_2SO_4. A similar oxidation process was also found in the Pt dissolution, where Pt is first oxidized into PtO_4 and then reduced into Pt(OH) [18]

Based on the dissolution process, we evaluated the U_{diss} of different 2D materials. The computational workflow to identify the potential dissolution sites was shown in Fig. S66. In detail, we divided the studied materials into three types according to surface structure: 1) material is terminated by a single element with the same coordination configuration, such as 2H and 1T phases of TMDs. 2) the basal plane is formed by a single element but has different coordination configurations, for example, 1T' phase of TMDs. 3) the basal plane has different elements and shows different coordination characteristics, such as MPX_3 systems (M is metal, X is S, Se or Te). For the type 1 structures, the dissolution potential can be directly computed through the GC-DFT simulation. For example, the chalcogenide sites (such as S, Se and Te) were selected for the evaluation of the electrochemical dissolution of TMDs since they are terminated by the chalcogenide elements. But for the type 2 configurations, we first carried out the simple binding energy analysis to identify

the weak binding sites, then we employed GC-DFT for the following evaluation. For materials with different elements located in the basal plane (i.e., type 3 materials), we initially compared their redox potentials and selected the element that more easily to undergo the dissolution/oxidation. Then, detailed analyses including binding energy calculation were performed. In general, the selection is highly associated with the surface configuration, and the redox nature of the elements, and only the most unstable sites were selected for the evaluation to realize the key dissolution process at the early stage of the reaction.

Note that it is difficult for the current DFT framework to well predict the free energy of ions properly. In this work, the free energy of the ions was computed from the electronic energy of elemental atoms in their bulk phase *via* the experimental determined standard reduction potential (U_0 vs SHE). For example, for a metal element, this yields

$$F_{M^{x+}(aq)} = E_{M(s)} - N_e^M\,\mu + x|e|U_0 + k_B T \ln[M^{x+}]$$

where $F_{M^{x+}(aq)}$ is the grand free energy of $M^{x+}(aq)$ at the concentration of $[M^{x+}]$ mol L^{-1}, N_e^M is the number of valence electrons of metal atom, and μ is electron absolute energy referred to the vacuum level (for the CANDLE solvation model, μ_{SHE} is −4.66 V, which is different from the experimentally measured value of −4.44 V). Here, considering the actual operating condition, the dissoluble $M^{x+}(aq)$ in the electrolyte is typically small, which is in the order of 10^{-3} ~ 10^{-6} mol L^{-1}. [19, 20] A concentration correction was applied, which was set to be 10^{-6} mol L^{-1}.

Assuming that metal dissolution in the 2D material follows the equation

$$M_n(s) \rightarrow M_{n-1}(s) + M^{x+}(\mathrm{aq}) + xe^-,$$

and the corresponding grand free energy change of metal dissolution as a function of electrode potential can be written as

$$\Delta F = F_{M^{x+}(aq)} + x\,(\mu - \mu_{SHE}) + F_{M_{n-1}(s)} - F_{M_n(s)}$$

where the potential-dependent grand free energies of catalyst before and after metal dissolution (i.e., $F_{M_n(s)}$ and $F_{M_{n-1}(s)}$) were obtained by fitting the relative free energies at electrode potential of 0 and 2.0 V *vs* SHE following the previous works, [9, 21, 22] and described as

$$F_{M(s)}(U) = k_x U + F_{M(s)}(0\,V\ vs.SHE)$$

It requires $\Delta F < 0$ to suppress the metal dissolution on the 2D materials, and thus the threshold potential of dissolution (U_{diss}) can be readily computed when $\Delta F = 0$. Similar procedures can be used to estimate the U_{diss} of the other active sites (see Table S7).

We note that shifting the concentration of $[M^{x+}]$ from 1.0 mol L^{-1} to 10^{-6} mol L^{-1} can slightly change the values of U_{diss}. The computational results before and after correction is around 0.1 V in most of the cases, and larger changes occur on the $PtPb_4$ (0.19 V), $VAg(PSe_3)_2$ (0.25 V), $CrGeTe_3$ (0.17 V), $AgHO_2$ (0.22 V), and $Te_2Pd_3Pb_2$ (0.16 V). The detailed values of U_{diss} with/without concentration correction are listed in Table S7.

Coverage effect on the catalytic activity of ORR and OER

To study the effect of adsorbate-adsorbate interactions on the catalytic activity of ORR and OER, two adsorption types, including single-side adsorption (only one side of basal plane as the reaction area), and double-side adsorption, were considered on the 2D PtTe and $NbSe_2$ monolayers. Here, the PtTe and $NbSe_2$ were selected to study the adsorbate-adsorbate interactions because: 1) both of them have excellent activity for oxygen electrocatalysis as demonstrated by our computations; 2) they display different characteristics for adsorption of oxygen-containing species, in which the PtTe monolayer shows strong binding towards reaction species (*i.e.*, OOH*, O*, and OH*) with OH*→H_2O as the potential limiting step (PDS) for ORR; while the $NbSe_2$ monolayer exhibits weak binding with OOH*, O*, and OH*, and the O_2→OOH* step is identified as the PDS of ORR.

According to our computations (Fig. S70a and S70b), when the reaction species coverage increases from low to high, the adsorption free energy of OOH*, O*, and OH* generally becomes more positive in both single- and double-side adsorption types, indicating that the interactions between the 2D materials and reaction intermediates are weakened. In particular, the coverage effect is more pronounced for the adsorption of O* than those of OOH* and OH* due to the strong band hybridization between O* and materials.

However, for the single-side adsorption, the coverage-induced potential difference is relatively small (with *ca.* 0.1 V derivation on the U_L value). The adsorbate-adsorbate interactions may not significantly affect the catalytic activity of the 2D materials in this adsorption mode. In comparison, the effect of the adsorbate-adsorbate interactions highly depends on the binding strength between the adsorbate and the material in the double-side adsorption.

Specifically, for the weak binding system of $NbSe_2$ monolayer, the U_L value of ORR/OER can be changed into 0.36/1.86 V in the double-side mode, and by comparison with the single-side adsorption, it is found that the coverage effect on the OER tends to be small, and the computed U_L values are in the range of 1.86−2.00 V, similar to those in the single-side mode (1.81−2.00 V). Whereas the adsorbate-adsorbate interactions can induce a largest derivation of 0.44 V on the U_L values of ORR, from 0.80 eV in the single-side mode to 0.36 V in the double-side adsorption, leading to a reduced catalytic activity. Such derivation between the two adsorption types is caused by the coverage-induced free energy change for OOH* adsorption, in which the adsorption free energy of OOH* on the $NbSe_2$ monolayer goes from 4.12 eV at the coverage of 12.5% in the single-side adsorption to 4.55 eV at the coverage of 37.5% in the double-side adsorption.

For the strong binding system of PtTe monolayer, the coverage-induced potential difference on ORR is insignificant due to the neglected free energy change for OOH* adsorption (Fig. S70a). However, for OER, with the change of the O* binding strength along different coverage, the U_L value decreases from *ca.* 2.20 V in the single-side adsorption to 1.76 V in double-side mode, suggesting that double-side adsorption can improve the catalytic performance of OER on the strong binding system.

In general, the above investigations suggest different approaches can be used to improve the catalytic performance, depending on the binding strength between the oxygen-containing species and the catalytic surface. For systems featuring weak binding for O*, OH*, and OOH*, for example, those with $O_2 \leftrightarrow$OOH* step as the PDS of ORR, tuning the adsorption type into single-side adsorption could help maintain their catalytic activity. For instance, by increasing catalytic layer from monolayer to bilayer and forming van der Waals interactions, the reactions in the interlayer can be inhibited, accordingly the coverage effects can be reduced, and the catalytic performance be well kept (see Fig. S70c). In addition, modulating the anchoring configurations of 2D materials on the catalytic substrates could be helpful to maintain/improve the catalytic performance of 2D materials. For example, by contacting the 2D monolayers with catalytic substrates using their basal planes (Fig. S70d), the double-side adsorption type could also be prohibited. Differently, for the strong binding systems (*e.g.*, PtTe), it would be better to use the well separated monolayer as the catalyst and take advantage of the double-side adsorption to further tune/improve catalytic performance.

Reaction kinetics of 2D materials for the oxygen electrocatalysis

The kinetic simulation of oxygen electrocatalysis were performed on the 2D materials using the PtTe and $NbSe_2$ as the prototypes (see Fig. S5). The climbing image nudged elastic band (CI-NEB) method was used

for finding saddle points and minimum energy pathways during the oxygen electrocatalysis by inserting six NEB images between the initial and final states. [23] Explicit $H_5O_2^+$ was used as the proton source, positioned above each surface of the materials. A linearized Poisson−Boltzmann implicit solvation model was used to neutralize the nonzero charge in the simulation, as implemented in VASPsol. [13] Here, we applied a plate-capacitor based approach[24] to extrapolate reaction energetics to constant potentials by correcting for the work function change via the following equation:

$$\Delta G = \Delta G_0 + \beta\,\overline{\Phi} = \Delta G_0 + (q_2 - q_1)\ \left(\frac{\Phi_1+\Phi_2}{2}\right)$$

where ΔG_0 is the free energy change of the two states at the potential of zero charge (PZC)), β is the charge transfer coefficient representing the potential dependence of the shift in energy between two given states. It is described by the difference in stored charge (q) between the two states within the capacitor model. Following the previous scheme, we employed Bader charge analysis to estimate β as the difference in the net charge of the catalyst surface from the transition state (TS) to the reaction's final state (FS). Moreover, to compare Φ to a potential experimental scale, the absolute potential reference of the standard hydrogen electrode was applied as $U_{SHE} = \Phi - 4.60$ V. The detailed reaction profiles of ORR on the PtTe and $NbSe_2$ were displayed in Fig. S5.

At the 0.0 V vs. SHE (i.e., overpotential η=1.23 V), the free energy changes along the ORR on these two surfaces are downhill without any kinetic barriers, indicating the reaction can proceed spontaneously. With the upshift of the external electrode potential (U) to the theoretical limiting potential (U_L, 0.83 V for PtTe, and 0.76 V for $NbSe_2$) and the equilibrium potential (U_{eq}, 1.23 V) of ORR, the kinetic barriers are arisen on both systems but yield different elementary steps.

On the PtTe surface (see Fig. S5a), the reaction is restricted in the step of OOH* protonation into O* (OOH* + H+/e- → O* +H_2O), and no distinguishable barriers are available in the other steps within the potential range, including O_2 to OOH*, O* to OH*, and OH* to H_2O. On the basis of the capacitor model, we estimate that the charge transfer coefficient β is about 0.75. The activation free energy ($\Delta G^{\ddagger}$) as the function of U follows the equation of $\Delta G^{\ddagger}$ = -0.36 + 0.75 U. Simply, we can evaluate that the kinetic barrier of OOH* protonation step is 0.26 eV at the condition of U_L and 0.56 eV at the U_{eq}, respectively.

Similarly, we accessed the kinetic limitations on the $NbSe_2$ surface (see Fig. S5b), The protonation of O* into OH* (O* + H^+/e^- → OH*) is identified as the rate-limiting step. The β is estimated by 0.34, and the corresponding kinetic barriers at the potential of U_L and U_{eq} are 0.18 eV and 0.34 eV, respectively. Such kinetic

barriers are in the same order as that on the Pt(111) (cat. 0.18 eV at the potential of U_L), and can be overcome at room temperature.

Generally, both previous studies and our own computations indicate that the kinetic contribution to oxygen electrocatalysis is insignificant, which might not dramatically change the activity trends obtained from the thermodynamic evaluation. Thus, the computational results presented in this manuscript could be credible and help to discover the potential catalysts and identify the active sites. Yet, based on catalytic activity analysis and electrochemical stability evaluation, we can conclude that simply predicting the catalytic activity and selectivity of catalysts could be insufficient to describe their overall performance; the stability issue of materials represents another central issue that should be carefully considered to preserve the active sites under the operating conditions. Therefore, to achieve a rational framework to identify candidate materials for experimental validation, *establishing effective methods to assess both catalytic activity and electrochemical stability* is very important, which is the focus of this study.

Table S1 Details about the 45 experimental synthesized 2D monolayers, including their formula, space group, decomposition energy, exfoliation energy, ID in Materials Project database, and reference of reported work.

Formula	Space group	Decomposition energy (meV/atom)	Exfoliation energy (meV/atom)	Obtained from	Reference
C	P6/mmm	2.1	67.0	mp-48	Science 2014, 306, 666–9
BN	$P6_3/mmc$	0.1	0.1	mp-7991	Nat. Mater. 2010, 9, 430–435
P	Pmna	42.5	109.4	mp-157	ACS Nano 2014, 8, 4033–4041
NbS_2	P-6m2	3.9	92.5	mp-10033	Nanoscale, 2017,9, 16607-16611
$NbSe_2$	P-6m2	5.1	5.1	mp-7597	Nat. Commun. 2017, 8, 394
$NbTe_2$	P-3m1	47.7	106.3	mp-1018150	Adv. Funct. Mater. 2019, 29, 1806611
VTe_2	P-3m1	22.6	98.2	mp-1008626	
$TaTe_2$	C2/m	17.6	114.0	mp-1967	
WTe_2	P2_1/m	0	84.6	mp-22693	2D Mater. 2017, 4 021008 Nano Lett. 2017, 17, 2, 878–885 Nanoscale, 2016, 8, 2309-2316
$MoSe_2$	P-6m2	1.9	78.3	mp-1634	ChemPhysChem, 2014, 15, 1592-1598
WSe_2	P-6m2	1.7	77.7	mp-1821	
$MoTe_2$	P-6m2	3.8	89.1	mp-602	Nano Lett. 2014, 14, 6231–6236
WS_2	P-6m2	1.6	56.4	mp-224	Nano Lett. 2013, 13, 3447–3454
C_3N_4	P-6m2	86.5	82.2	mp-971684	Carbon 2014, 80, 213-221
MoS_2	P-6m2	2.1	76.3	mp-2815	Sci. Rep. 2013, 3, 1866
ZrS_2	P-3m1	0	89.4	mp-1186	J. Am. Chem. Soc. 2015, 137, 7051–7054
$ZrSe_2$	P-3m1	0	95.4	mp-2076	Appl. Sci. 2016, 6 264
HfS_2	P-3m1	0	86.4	mp-985829	Adv. Mater. 2015, 27 7881–7
TaS_2	P-1	16.6	90.4	none	Chem. Mater. 2016, 28 7613–8
$TaSe_2$	P-6m2	3.8	69.3	mp-500	Nano Lett. 2018, 8 689–94
VSe_2	P-3m1	0	86.0	mp-694	Chem. Commun. 2016, 52 9228–31
VS_2	P-6m2	0	78.7	mp-1013525	Adv. Funct. Mater. 2020, 30, 2000240
$PtSe_2$	P-3m1	0	88.7	mp-1115	Nano Lett. 2015, 15 4013–8
PtS_2	P-3m1	0	97.7	mp-762	Adv. Mater. 2016, 28 2399–407

TiS_2	P-3m1	2.0	88.4	mp-2156	Nat. Mater. 2015, 14, 622–627
$TiSe_2$	P-3m1	0	92.3	mp-2194	Adv. Mater. 2018, 30, 1704382
ReS_2	P-1	0	71.5	mp-572758	Nat. Commun. 2014, 5, 3252
$PdSe_2$	P2_1/c	8.0	166.7	mp-2418	J. Am. Chem. Soc. 2017, 139, 14090–14097
InSe	P-6m2	1.9	63.7	mp-22691	2D Mater. 2018, 5, 025019
GaTe	P-6m2	8.3	58.5	mp-10009	2D Mater. 2018, 2, 035010
GaSe	P-6m2	2.1	43.6	mp-1943	2D Mater. 2018, 2, 035010
TiS_3	Pmmn	0	54.2	mp-9920	Adv. Mater. 2015, 27, 2595-2601
$HfTe_3$	Pmmn	25.5	88.9	mp-1025459	Adv. Electron. Mater. 2016, 2, 1600324
CrI_3	P-31m	0	89.2	none	Nature 2017, 546, 270–273
BiI_3	P-31m	9.2	95.7	mp-22849	ACS Appl. Mater. Interfaces 2021, 13, 25918–25925
FeSe	P4/nmm	0	85.5	mp-20311	Phys. Rev. B 2011, 84, 020503
MoO_3	P2_1/m	32.9	38.9	mp-510584	Nano Lett. 2017, 17, 3854–3861
Bi_2Se_3	P-3m1	0	67.7	mp-541837	Nano Lett. 2015, 15, 2645–2651
Bi_2Te_3	P-3m1	0	77.9	mp-34202	ACS Nano 2016, 10, 11442–11448
SnS_2	P-3m1	3.7	81.7	mp-1170	ACS Nano 2019, 13, 8265–8274
GaS	P-6m2	1.3	39.3	mp-2507	Nano Lett. 2013, 13, 1649-1654
ReS_2	P-1	0	71.5	mp-572758	Adv. Mater. 2020, 32, 2001890
$ReSe_2$	P-1	0	74.5	mp-541582	Nano Res. 2018, 11, 1787–1797
$PtTe_2$	P-3m1	0	145.7	mp-399	Nat. Commun. 2017, 8, 257
$CrTe_2$	P2_1/m	28.3	28.3	none	Nat. Commun. 2021, 12, 2492

Table S2. Structural and electronic information of 339 candidate materials which screened from the band structure analysis, including space group, band gap, decomposition energy, exfoliation energy, Electrical conductivity, and Identity number in materials project database. Note that the ground state of the layered materials might be changed due to the update of database, which would slightly change the values of the decomposition and exfoliation energies.

Formula	Space group	Band gap (meV)	Is gap direct?	Decomposition compound(s)	Decomposition energy (meV/atom)	Exfoliation energy (meV/atom)	Electrical conductivity (Ω^{-1} m^{-1} s^{-1})	Identity number in MP
$Eu(ReO_4)_2$	P-3	314	No	\	0	68	4.19E-10	mp-754760
$HfFeCl_6$	P312	94	No	$FeCl_3$ + Fe + $HfCl_4$	18	70	3.07E-03	mp-28220
Gd_2CCl_2	P-3m1	493	No	$Gd_5C_2Cl_9$ + $Gd_4C_2Cl_3$ + C	0	41	2.19E+00	mp-29394
$PdSeO_3$	C2/m	452	Yes	$PdSeO_3$	22	67	8.31E+00	mp-546684
Gd_2Br_3	C2/m	149	No	$GdBr_3$ + Gd	9	100	2.35E+01	mp-618813
$VCuO_4$	Pmma	290	No	Cu_2O_3 + V_2O_5	71	111	3.57E+01	mp-510733
$CuBrO_2$	P2/m	0	No	Br_2O_3 + Cu_2O_3 + Br	27	143	2.04E+02	mp-996993
$CuBrO_2$	P222_1	458	Yes	Br_2O_3 + Cu_2O_3 + Br	36	56	2.04E+02	mp-997011
$CuSbS_2$	Pmc2_1	373	Yes	\	0	144	3.39E+02	mp-4468
$CeP_3H_8O_7$	P-1	311	No	H_2O + $CePO_4$ + H_2 + P	49	42	3.44E+02	mp-505610
ZrI_2	P2_1/m	432	No	\	0	77	6.06E+02	mp-570506
K_2As_2Pd	Pmma	423	Yes	\	0	156	7.35E+02	mp-8147
$ZrSe_2$	P-3m1	458	No	\	0	95	9.32E+02	mp-2076
$FeCl_2$	P-3m1	0	No	\	0	64	9.76E+02	mp-23229
$TiGeTe_6$	P2_1/m	412	No	\	0	101	9.93E+02	mp-574169
Nb_2GeTe_4	Pbam	430	No	\	0	80	1.20E+03	mp-29073
In_2Se_3	P-3m1	492	No	In_2Se_3	48	51	1.34E+03	mp-1017565
K_2P_2Pd	Pmma	401	No	\	0	172	2.53E+03	mp-7505
$_2$-Feb	P-3m1	0	No	\	0	73	3.45E+03	mp-22880
TiS_3	Pmmn	275	Yes	\	0	54	3.66E+03	mp-9920
$Ge_4Te_7As_2$	P-3m1	422	No	Te_3As_2 + GeTe	19	33	7.93E+03	mp-568730
$ZrSe_3$	Pmmn	448	No	\	0	54	8.45E+03	mp-1683
La_2GeI_2	P-3m1	402	No	\	0	48	1.05E+04	mp-570597
FeI_2	P-3m1	0	No	\	0	81	1.08E+04	mp-571122
NbS_3	P2_1/m	406	No	NbS_3	0	46	1.36E+04	mp-562100
CeI_3	Pmmn	30	No	\	0	98	1.56E+04	mp-1025426
$TaSe_2$	P-3	159	No	$TaSe_2$	7	92	3.10E+04	mp-542495
$Ge_5(Te_4As)_2$	P-3m1	322	No	Te_3As_2 + GeTe	19	25	4.04E+04	mp-28487

$CuSeO_3$	P2_1/c	134	No	$Cu_4Se_3O_{10}$ + $CuSe_2O_5$	36	36	5.70E+04	mp-22688
$CuSbSe_2$	Pmc2_1	152	Yes	\	0	152	5.86E+04	mp-20331
$MoCl_3$	C2/m	126	Yes	$MoCl_5$ + $MoCl_2$	60	70	7.41E+04	mp-22853
C	P6/mmm	0	Yes	C	2	67	7.55E+04	mp-48
$Li_2NbP_4O_{13}$	P-1	262	No	$Nb_2(PO_4)_3$ + $LiPO_3$ + P_2O_5 + P	70	36	7.79E+04	mp-673156
Rb_2O	P31m	316	No	Rb_2O	10	51	1.29E+05	mp-776922
$HfSe_3$	Pmmn	360	No	\	0	47	1.43E+05	mp-15622
Y_2GeI_2	P-3m1	157	No	\	0	45	1.88E+05	mp-676315
$Sc_6C_2I_{11}$	P-1	386	No	\	0	78	3.31E+05	mp-541102
TiIN	Pmmn	31	Yes	\	0	44	5.04E+05	mp-27848
CeBrO	P4/nmm	0	No	\	0	63	5.82E+05	mp-754112
CeBrO	P-3m1	0	No	CeBrO	19	38	5.82E+05	mp-755464
$Ge_3(BiTe_3)_2$	P3m1	0	No	Bi_2Te_3 + GeTe	38	37	5.94E+05	mp-540687
$AgSb_2F_{12}$	P-1	454	No	\	0	29	7.49E+05	mp-14653
CrP_2S_7	C2	36	No	P_2S_5 + P_2S_7 + Cr_5S_8	32	56	7.87E+05	mp-768680
$CuTeO_3$	P2_1/c	1	Yes	CuO + TeO_2	69	148	7.91E+05	mp-558696
$Li_2CrP_4O_{13}$	P-1	343	Yes	$LiCrP_2O_7$ + $LiPO_3$ + $Cr(PO_3)_3$ + O_2	60	36	8.17E+05	mp-705053
CuH_2SeO_5	P-1	0	No	$CuSeO_4$ + H_2O	44	120	8.37E+05	mp-23955
$MnPSe_3$	P-31m	450	Yes	\	0	73	8.94E+05	mp-8695
CuHClO	P2_1/c	19	No	H_2O + CuO + $CuCl_2$	75	82	9.63E+05	mp-643743
$V_2P_4S_{13}$	P-1	129	No	P_4S_9 + VS_2	12	69	9.94E+05	mp-620190
$Li_2Cu_2F_7$	P-1	150	No	$LiCu_2F_6$ + LiF	68	53	1.16E+06	mp-753090
$SrSbSe_2F$	P4/nmm	58	Yes	SrSe + Sb_2Se_3 + SrF_2	29	58	1.16E+06	mp-556194
BiTe	P-3m1	0	No	Bi_4Te_3 + Bi_2Te_3	6	33	1.17E+06	mp-23224
$Li_2Cr_3(CO_3)_6$	P-1	0	No	CrO_2 + $LiCr(CO_3)_2$ + CO_2	71	70	1.18E+06	mp-763398
Mn_2F_7	P2/c	215	Yes	MnF_3 + MnF_4	52	41	1.24E+06	mp-765923
$CrTe_3$	Pmna	279	No	$CrTe_2$ + Te	21	97	1.30E+06	mp-540922
$NbTe_4Ir$	P2_1/m	28	No	\	0	103	1.34E+06	mp-505164
$AgIrF_7$	Pmc2_1	0	No	\	0	85	1.36E+06	mp-662534
Nb_3Cl_8	P3m1	236	No	\	0	72	1.37E+06	mp-29950
$CuMoO_4$	P1	430	No	MoO_3 + CuO	52	134	1.45E+06	mp-619545
La_2Br_5	P2_1/m	412	No	$LaBr_2$ + $LaBr_3$	6	101	1.46E+06	mp-28571
$Bi_2Te_5Pb_2$	P-3m1	0	No	TePb + Bi_2Te_4Pb	64	48	1.51E+06	mp-569044

$Cu(IO_3)_2$	P2_1/m	426	No	$Cu(IO_3)_2$	20	68	1.53E+06	mp-556582
$CuSeO_3$	P-1	0	No	$Cu_4Se_3O_{10}$ + $CuSe_2O_5$	20	54	1.60E+06	mp-560049
$LiWCl_6$	P3	74	No	WCl_4 + WCl_6 + LiCl	17	75	1.64E+06	mp-570512
$ZrTe_5$	Pmmn	22	Yes	\	0	90	1.65E+06	mp-605
$Zn(InS_2)_2$	P3m1	0	No	$Zn(InS_2)_2$	76	59	1.66E+06	mp-22253
$MnSbSe_2I$	P2/m	73	No	$Mn(SbSe_2)_2$ + MnI_2	72	189	1.67E+06	mp-570268
Nb_3I_8	P3m1	293	No	\	0	99	1.69E+06	mp-27772
$VAg(PS_3)_2$	P2/c	0	No	P_4S_7 + VS_2 + P_4S_3 + Ag_3PS_4	29	67	1.70E+06	mp-6462
CeZnPO	P-3m1	0	No	\	0	142	1.74E+06	mp-13207
Nb_3SiTe_6	Pmc2_1	0	No	$NbTe_2$ + Nb_2SiTe_4	10	94	1.79E+06	mp-505137
$AgBi_2F_{12}$	P-1	363	No	\	0	31	1.89E+06	mp-28965
Ta_2PtSe_7	P2_1/m	14	No	$Ta_2Pt_3Se_8$ + $TaSe_3$ + $PtSe_2$	3	80	1.91E+06	mp-14474
$TaTe_4Ir$	P2_1/m	24	No	\	0	98	1.92E+06	mp-17287
Nb_3GeTe_6	Pmc2_1	0	No	$NbTe_2$ + Nb_2GeTe_4	12	94	1.93E+06	mp-28754
CrS_2	P-3m1	0	No	\	0	53	1.99E+06	mp-755263
$CuAgO_2$	P2/m	0	No	$CuAgO_2$	73	193	2.03E+06	mp-7237
Ta_3SiTe_6	Pmc2_1	0	No	\	0	92	2.06E+06	mp-505206
$Cu_2H_2CO_5$	P2_1/c	0	No	CuO + H_2O + CO_2	60	100	2.10E+06	mp-504588
CuH_2SO_5	P-1	233	No	\	0	113	2.17E+06	mp-24522
$CrPO_5$	P-1	377	No	$CrPO_4$ + O_2	44	26	2.18E+06	mp-773520
$_3$-Feb	P-31m	40	No	\	0	81	2.22E+06	mp-23232
$FeCl_3$	P-31m	395	No	\	0	69	2.23E+06	mp-583463
VCl_3	P-31m	1	Yes	VCl_2 + VCl_4	0	73	2.23E+06	mp-28117
$TiAgF_6$	P-1	208	No	AgF_2 + TiF_4	54	119	2.23E+06	mp-10810
Sc_7Cl_{10}	C2/m	0	No	\	0	69	2.37E+06	mp-27513
$Ta_2Te_5Pd_3$	Pmn2_1	0	No	\	0	85	2.42E+06	mp-28934
$Li_2FeP_4O_{13}$	P-1	47	No	$LiFeP_2O_7$ + $LiFe(PO_3)_4$ + $LiPO_3$ + O_2	74	40	2.43E+06	mp-763647
ZrBr	P-3m1	0	No	\	0	55	2.54E+06	mp-504594
Te_2OsCl_{12}	P-1	0	No	\	24	44	2.59E+06	mp-28866
La_2I_5	P2_1/m	254	No	\	0	92	2.61E+06	mp-30282
$HfTe_5$	Pmmn	0	No	\	0	89	2.65E+06	mp-1168
Cu_3OF_5	P2_1	0	No	CuF_2 + Cu_2O_3 + O_2	58	76	2.71E+06	mp-755255

$Ce_4C_2Br_5$	Pmmm	0	No	Ce_2C_3 + $Ce_5C_2Br_9$ + Ce	7	105	2.72E+06	mp-574262
$Li_2Cu_2F_5$	P2_1/m	101	No	CuF_2 + LiF + Cu	60	54	2.83E+06	mp-762270
$MnSbSe_2Br$	Pmc2_1	115	No	$Mn(SbSe_2)_2$ + $MnBr_2$	80	195	2.84E+06	mp-567478
$Er(ReO_4)_2$	P-3	0	No	$Er(ReO_4)_3$ + ReO_3 + Er_2O_3	26	86	2.85E+06	mp-755194
BiSe	P-3m1	0	No	Bi_2Se_3 + Bi	8	26	2.87E+06	mp-27902
$CuMoF_6$	P-1	0	No	MoF_6 + CuF_2 + MoF_3	73	108	2.91E+06	mp-611706
H_4W	P4/nmm	23	No	W + H_2	16	25	2.95E+06	mp-1078595
$RuCl_3$	P-31m	3	Yes	$RuCl_3$	33	74	2.98E+06	mp-570997
$TaCoTe_2$	P2_1/c	9	Yes	$Ta(CoTe)_2$ + $TaTe_2$	12	75	3.24E+06	mp-28846
Er_6I_7	C2/m	0	No	Er + ErI_3	59	69	3.24E+06	mp-571258
$CuH_2(SeO_3)_2$	P2_1/c	72	Yes	\	0	93	3.35E+06	mp-24164
Pr_2Br_5	P2_1/m	349	No	\	0	93	3.44E+06	mp-23169
$Ta_4Co_2PdSe_{12}$	C2/m	6	No	\	0	82	3.48E+06	mp-505133
TbCl	P-3m1	0	No	Tb_2Cl_3 + Tb	53	53	3.52E+06	mp-27923
$CuTeO_4$	P2/m	0	No	$CuTeO_4$	25	125	3.56E+06	mp-755455
K_2RuBr_6	Pmn2_1	0	No	\	0	none	3.62E+06	mp-1097045
$VAg(PSe_3)_2$	C2	95	No	Ag_2PSe_3 + V_2Se_9 + VSe_2 + PSe	12	72	3.63E+06	mp-6543
KFe_2S_3	Pmma	0	No	\	0	138	3.66E+06	mp-22035
MnF_4	P2_1/c	32	Yes	\	0	48	3.74E+06	mp-765921
Nb_2Se_3	P2_1/m	11	No	Nb_3Se_4 + $NbSe_2$	48	137	3.76E+06	mp-2330
$Pr(ReO_4)_2$	P-3	0	No	\	0	92	3.84E+06	mp-754632
Ta_2NiS_5	Pmmn	0	No	\	0	72	3.96E+06	mp-28308
$CrGeTe_3$	P-31m	484	No	GeTe + Cr_5Te_8 + Te	0	89	4.01E+06	mp-541449
Nb_9IrSe_{20}	P-1	0	No	$IrSe_2$ + $NbSe_2$	45	68	4.03E+06	mp-675290
Ta_2NiSe_5	Pmmn	0	No	\	0	73	4.03E+06	mp-541070
TiS_2	P-3m1	26	No	\	0	88	4.05E+06	mp-2156
$NiPS_3$	P-31m	47	No	P_4S_7 + NiPS + Ni_3S_4	64	61	4.05E+06	mp-676040
TbBr	P-3m1	0	No	$TbBr_3$ + Tb	16	47	4.06E+06	mp-27924
$TiCl_3$	C2/m	0	No	$TiCl_3$	5	61	4.15E+06	mp-569756
$AgRuF_7$	P2_1/c	0	No	\	0	31	4.28E+06	mp-17588
$LiNi(PS_3)_2$	P312	31	No	P_4S_9 + Li_3PS_4 + P_4S_7 + Ni_3S_4	36	63	4.30E+06	mp-557500
$TiBr_3$	C2/m	0	No	\	2	79	4.31E+06	mp-28214
Fe_4S_5	P4/n	0	No	FeS + FeS_2	59	2	4.35E+06	mp-850083
$TaSe_3$	P2_1/m	0	No	\	0	65	4.39E+06	mp-29652

Sc_5Cl_8	P2/m	0	No	\	1	79	4.45E+06	mp-542449
Pr_2I_5	P2_1/m	155	No	\	0	88	4.53E+06	mp-22854
Nb_4IrSe_{10}	P-1	0	No	$IrSe_2$ + $NbSe_2$	38	86	4.54E+06	mp-675326
$CrCuO_4$	Pmma	116	No	Cr_5O_{12} + Cu_2O_3 + O_2	69	127	4.58E+06	mp-504927
KFe_2Se_3	Pmma	0	No	FeSe + $KFeSe_2$	68	129	4.69E+06	mp-1095516
ZrCl	P-3m1	0	No	\	0	52	4.71E+06	mp-27440
$La_2(BiO_2)_7$	P1	0	No	$La_2Bi_2O_7$ + $La_{10}Bi_8O_{27}$ + Bi_2O_3	77	37	4.83E+06	mp-753524
$NbCoTe_2$	P2_1/c	0	No	$NbCoTe_2$	7	78	5.25E+06	mp-571471
Tb_5Br_8	P2/m	0	No	$TbBr_3$ + Tb	33	103	5.28E+06	mp-31007
YCl	C2/m	0	No	\	0	37	5.33E+06	mp-23062
YCl	P-3m1	0	No	Y_2Cl_3 + Y	51	54	5.33E+06	mp-540884
$Tl_2Cu_3(SeO_3)_6$	P-1	162	No	\	0	56	5.44E+06	mp-558944
Nb_3IrSe_8	C2	0	No	$IrSe_2$ + $NbSe_2$	11	88	5.45E+06	mp-675066
$Cu_3Te_2(BrO_3)_2$	C2/m	0	No	$CuBr_2$ + CuO + TeO_2	17	41	5.48E+06	mp-572313
$Ag(TeMo)_6$	C2/m	0	No	\	0	76	5.53E+06	mp-29607
$NbCrSe_5$	P2_1/m	0	No	Nb_2Se_9 + Cr_2Se_3 + $NbSe_2$	2	77	5.55E+06	mp-28019
CrI_2	C2/m	253	No	CrI_3 + Cr	0	84	5.58E+06	mp-27215
$Fe(CO_3)_2$	P-3	0	No	CO_2 + Fe_2O_3 + O_2	59	36	5.84E+06	mp-769642
CuF_2	P2_1/c	461	No	\	0	127	5.88E+06	mp-1229
$LiCu(PO_3)_3$	P-1	401	No	$LiCu(PO_3)_3$	71	79	6.04E+06	mp-758797
Ta_2Se_3	P2_1/m	0	No	Ta_2Se + $TaSe_2$	30	123	6.05E+06	mp-9983
TbGaI	P-3m1	0	No	\	0	45	6.23E+06	mp-1025099
Te_2W	P2_1/m	73	No	\	0	84	6.25E+06	mp-22693
$AgClO_2$	P2_1/m	186	No	$AgClO_4$ + AgCl	0	54	6.27E+06	mp-997017
Cu_3OF_5	P-1	0	No	CuF_2 + Cu_2O_3 + O_2	60	72	6.27E+06	mp-755349
$Mn_2Ga_2S_5$	P-3m1	0	No	$Mn(GaS_2)_2$ + MnS	50	26	6.28E+06	mp-1078896
ScHCl	P-3m1	0	No	\	0	35	6.96E+06	mp-24081
$CrBr_2$	C2/m	447	No	$CrBr_3$ + Cr	73	74	7.01E+06	mp-567624
$Cu_3Se_2(ClO_3)_2$	C2/m	0	No	$CuSe_2O_5$ + $Cu_4Se_3O_{10}$ + $CuCl_2$	3	42	7.18E+06	mp-557136
$Cu_3Se_2(ClO_3)_2$	P-1	58	No	$CuSe_2O_5$ + $Cu_4Se_3O_{10}$ + $CuCl_2$	14	49	7.18E+06	mp-557946
VTe_2	C2/m	0	No	\	0	115	7.18E+06	mp-11687
Sc_5CCl_8	P2/m	0	No	\	0	102	7.20E+06	mp-31024

$CrSe_2$	P-3m1	0	No	Cr_2Se_3 + Se	11	113	7.22E+06	mp-1009581
Ag_2IO_6	P-31m	0	No	Ag_3O_4 + AgI_3O_8 + O_2	45	9	7.25E+06	mp-1079032
Sr_2CoClO_3	P4/nmm	0	No	$Sr_3(CoO_3)_2$ + $Sr_2Co_2O_5$ + Sr_4Cl_6O	36	35	7.25E+06	mp-505678
YGaI	P-3m1	0	No	\	0	39	7.39E+06	mp-571210
$TaTe_2$	C2/m	0	No	\	17	114	7.43E+06	mp-1967
$NiPSe_3$	P-31m	0	No	$NiSe_2$ + NiP_2 + Se	64	74	7.45E+06	mp-1079754
AgF_2	P2_1/c	0	No	\	0	150	7.52E+06	mp-7715
$Y_7C_3I_6O$	Pmma	0	No	\	0	31	7.72E+06	mp-554027
$AgHO_2$	Cm	0	No	\	0	126	7.75E+06	mp-996958
$TaFeTe_3$	P2_1/m	0	No	Ta_4FeTe_4 + $FeTe_2$ + $TaTe_2$	24	82	7.80E+06	mp-8848
Ta_2PdSe_6	C2/m	79	No	\	0	89	7.91E+06	mp-8436
Mn_3CuO_8	P-3m1	6	No	Cu_2O_3 + MnO_2 + O_2	61	60	7.99E+06	mp-771841
$Cr(GaS_2)_2$	P-3m1	0	No	GaS + Cr_3GaS_6 + Ga_2S_3	62	36	8.54E+06	mp-985304
$ZrCl_3$	C2/m	173	No	$ZrCl_3$	51	73	8.67E+06	mp-1100795
$Sr_3Co_2Cl_2O_5$	P4/mmm	0	No	$Sr_2Co_2O_5$ + $Sr_5(CoO_3)_4$ + Co_3O_4 + Sr_4Cl_6O	53	8	8.69E+06	mp-24846
$NbFeTe_2$	Pmna	0	No	$NbTe_2$ + Fe	25	82	8.69E+06	mp-616481
Cr_3Te_4	P-3m1	0	No	Cr_5Te_8 + Cr	67	51	8.79E+06	mp-570122
$NbTe_2$	C2/m	0	No	\	0	121	8.81E+06	mp-11675
V_6O_{13}	Pmma	0	No	VO_2 + V_2O_5	63	67	9.07E+06	mp-715617
Tl_2CuF_4	P4/mmm	0	No	\	0	66	9.14E+06	mp-1025338
Ta_2PdS_6	C2/m	162	No	\	0	83	9.39E+06	mp-8435
Sc_5NCl_8	P2/m	0	No	Sc_5Cl_8 + Sc_4NCl_6 + $ScCl_3$	28	98	9.49E+06	mp-31025
LuHCl	P-3m1	0	No	\	0	36	9.49E+06	mp-23896
ErHCl	P-3m1	0	No	\	0	36	9.64E+06	mp-24051
KV_4O_{10}	Amm2	0	No	VO_2 + KV_3O_8	50	61	9.69E+06	mp-767780
Bi_4I	P2/m	0	No	BiI_3 + Bi	76	102	9.72E+06	mp-583234
$CoCl_2$	P-3m1	109	No	$CoCl_2$	0	67	9.82E+06	mp-23240
$MoTe_2$	P2_1/m	0	No	$MoTe_2$	21	87	9.88E+06	mp-7459
ScCl	P-3m1	0	No	Sc_7Cl_{10} + Sc	23	50	9.99E+06	mp-27507
$Ta_3Te_{14}Pd_3$	Pm	0	No	\	0	104	1.02E+07	mp-505132
$LiCu_2(CO_3)_2$	P1	0	No	Cu_2O + Li_2CO_3 + CuO + CO_2	70	53	1.03E+07	mp-760546
Bi_9I_2	P2_1/m	0	No	BiI_3 + Bi	70	97	1.03E+07	mp-28149
Y_4Cl_5	Pmmm	0	No	\	0	80	1.04E+07	mp-23382

$TaNi_2Te_3$	P2_1/m	0	No	\	0	79	1.05E+07	mp-9391
$La_4C_2Br_5$	Pmmm	0	No	\	0	107	1.09E+07	mp-569873
CrSBr	Pmmn	292	Yes	\	0	51	1.09E+07	mp-22998
RbV_4O_{10}	Cmmm	0	No	RbV_3O_8 + VO_2	45	61	1.09E+07	mp-764947
$Sc_7(CCl_5)_2$	C2/m	0	No	\	0	81	1.11E+07	mp-29315
Nb_2Te_3	P2_1/m	0	No	$NbTe_2$ + Nb_3Te_4	38	102	1.13E+07	mp-570451
$CuSi_2P_3$	Pm	0	No	Cu_4SiP_8 + $Cu_{15}Si_4$ + SiP	64	24	1.14E+07	mp-674984
$Y_6C_2I_7$	C2/m	0	No	\	0	55	1.14E+07	mp-23440
$NbSe_3$	P2_1/m	0	No	\	0	57	1.19E+07	mp-525
Na_2ZrN_2	P-3m1	0	No	Zr_3N_4 + NaN_3 + Na	78	43	1.22E+07	mp-1029316
$TaTe_2$	C2/m	0	No	$TaTe_2$	20	113	1.23E+07	mp-601823
$Bi_2Rh_3S_2$	C2/m	0	No	\	0	150	1.25E+07	mp-977592
$CoBr_2$	P-3m1	43	No	\	0	75	1.26E+07	mp-30033
$Mn(InSe_2)_2$	P3m1	0	No	MnSe + In_2Se_3	39	51	1.27E+07	mp-1078140
Nb_2PdS_6	C2/m	0	No	\	0	86	1.29E+07	mp-1080466
$AgClO_2$	P2_1/m	13	No	$AgClO_4$ + AgCl	0	59	1.32E+07	mp-997013
Ta_2Te_3	C2/m	0	No	\	0	78	1.32E+07	mp-542634
$LiCu_3F_{10}$	Pc	0	No	\	0	41	1.32E+07	mp-760825
$NbNiTe_2$	Pmna	0	No	\	0	81	1.32E+07	mp-20506
Nb_3IrS_8	C2	0	No	NbS_2 + IrS_2	28	89	1.33E+07	mp-675367
TaS_3	P2_1/m	0	No	\	0	55	1.36E+07	mp-30527
RbMnAs	P4/nmm	0	No	RbAs + Mn	73	-11	1.37E+07	mp-20242
$Pr_4C_2Cl_5$	Pmmm	0	No	\	0	123	1.39E+07	mp-570498
Na_2HfN_2	P-3m1	0	No	Hf_3N_4 + NaN_3 + Na	76	43	1.45E+07	mp-1029309
Ga_2NiS_4	P-3m1	0	No	Ni_9S_8 + Ni_3S_4 + Ga_2S_3	54	29	1.45E+07	mp-6959
MnS_2	P-3m1	0	No	\	0	59	1.46E+07	mvc-14047
$HfTe_2$	P-3m1	0	No	\	0	103	1.48E+07	mp-32887
$TiSe_2$	P-3m1	0	No	\	0	92	1.48E+07	mp-2194
NaFeAs	P4/nmm	0	No	\	0	105	1.50E+07	mp-22152
$TaNiTe_2$	Pmna	0	No	\	0	82	1.59E+07	mp-19810
CoI_2	P-3m1	0	No	Co + I	19	88	1.66E+07	mp-569610
VBr_2O	Pmmm	408	Yes	VBrO + Br	13	64	1.81E+07	mp-32450
$CuAuO_2$	P2/m	0	No	\	0	182	1.82E+07	mp-996978
$Sr_2Cu(IO)_2$	P4/mmm	0	No	\	0	41	1.87E+07	mp-549487
VS_2	P-6m2	27	No	\	0	78	1.89E+07	mp-1013525
$AlPd_5I_2$	P4/mmm	0	No	\	0	50	1.90E+07	mp-27393
CeSiI	P-3m1	0	No	\	0	43	1.92E+07	mp-29535
AuSe	C2/m	0	No	AuSe	10	74	1.92E+07	mp-570325
Ta_2Se	P4/nmm	0	No	\	0	59	1.93E+07	mp-8732

LaI_2	P4/mmm	0	No	\	0	85	1.96E+07	mp-23194
$Ag(AuS)_2$	Pc	0	No	Ag_3AuS_2 + $AgAuS_2$ + Au_2S	64	98	1.97E+07	mp-35835
EuBrO	P4/nmm	0	No	\	0	59	2.08E+07	mp-504727
$CuBr_2$	C2/m	0	No	\	0	93	2.12E+07	mp-23219
$Sr_2Co(ClO)_2$	P4/mmm	225	No	$Sr_2Co(ClO)_2$	23	54	2.12E+07	mp-560610
RbMnP	P4/nmm	0	No	\	0	46	2.13E+07	mp-21413
$ZrTiTe_4$	P2/m	0	No	$TiTe_2$ + $ZrTe_2$	25	113	2.13E+07	mp-8677
$Ca(TiS_2)_8$	P-3m1	0	No	\	0	40	2.13E+07	mvc-16026
$Sr_2Cu(BrO)_2$	P4/mmm	0	No	\	0	48	2.13E+07	mp-546898
FeSe	P4/nmm	0	No	\	0	85	2.15E+07	mp-20311
$NbSe_2$	P-6m2	0	No	$NbSe_2$	5	93	2.18E+07	mp-7597
VTe_2	P-3m1	0	No	VTe_2	22	98	2.19E+07	mp-1008626
NaMnAs	P4/nmm	0	No	$Mn_{23}As_{16}$ + Na_3As + Mn	73	93	2.20E+07	mp-20612
ZrHCl	P-3m1	0	No	$ZrCl_2$ + ZrH_2	73	33	2.23E+07	mp-1024958
$Ca_2Cu(BrO)_2$	P4/mmm	0	No	\	0	42	2.26E+07	mp-545481
NiI_2	P-3m1	142	No	\	0	79	2.28E+07	mp-27638
$TaSe_2$	P-6m2	0	No	$TaSe_2$	3	69	2.29E+07	mp-500
KMnP	P4/nmm	0	No	\	0	48	2.30E+07	mp-20422
$Sr_2Cu(ClO)_2$	P4/mmm	0	No	\	0	74	2.31E+07	mp-23102
$Ca_2Cu(ClO)_2$	P4/mmm	0	No	Ca_4Cl_6O + $CaCu_3O_4$ + CaO	20	63	2.34E+07	mp-23143
$Na_3(TiS_2)_{10}$	Cm	0	No	\	0	43	2.36E+07	mp-675056
LiFeP	P4/nmm	0	No	\	0	163	2.36E+07	mp-20049
FeS	P4/nmm	0	No	\	0	83	2.41E+07	mp-505531
$CoTe_2$	P-3m1	0	No	\	0	165	2.42E+07	mp-1009641
NbS_2	P-6m2	0	No	\	0	92	2.43E+07	mp-10033
NdI_2	P4/mmm	0	No	\	0	94	2.57E+07	mp-28753
TaS_2	P-6m2	0	No	\	0	88	2.61E+07	mp-1984
Ta_4AgS_8	P2_1/m	0	No	Ta_4AgS_8	0	43	2.66E+07	mp-677597
$NbNiTe_5$	Pmma	0	No	\	0	78	2.76E+07	mp-8999
MnSe	P4/nmm	0	No	MnSe	32	82	2.80E+07	mp-604910
GdBr	P-3m1	0	No	$GdBr_3$ + Gd	70	57	2.84E+07	mp-1064427
Zr_2HBr_2	P2_1/m	0	No	ZrBr + ZrH_2 + $ZrBr_3$	24	41	2.94E+07	mp-642803
VSe_2	P-3m1	0	No	\	0	86	2.95E+07	mp-694
La_2PI_2	P-3m1	0	No	\	0	54	3.00E+07	mp-571647
$TaTe_5Pt$	Pmma	0	No	\	0	70	3.01E+07	mp-14815
AgO_2F	P2_1/m	0	No	\	0	78	3.02E+07	mp-997101
$TaNiTe_5$	Pmma	0	No	\	0	73	3.03E+07	mp-8998
CoSe	P4/nmm	0	No	Co_3Se_4 + Co_9Se_8	16	104	3.04E+07	mp-604908

Sr_2MnClO_3	P4/nmm	0	No	\	0	33	3.05E+07	mp-561903
TiBrO	Pmmn	0	No	Ti_2O_3 + $TiBr_3$	17	40	3.05E+07	mp-23002
La_2PBr_2	P-3m1	0	No	\	0	51	3.20E+07	mp-570988
$TaNi_2TeSe$	Pmma	0	No	\	0	51	3.24E+07	mp-622009
$NbTe_5Pd$	Pmc2_1	0	No	$NbTe_4$ + Te_2Pd + $NbTe_2$	1	83	3.27E+07	mp-28616
$Sr_2Cu(BiO_3)_2$	Pmna	0	No	$SrCuO_2$ + $Sr(BiO_2)_2$	70	37	3.32E+07	mp-555827
$TiTe_2$	P-3m1	0	No	\	0	110	3.34E+07	mp-1907
$Te_2Pd_3Pb_2$	Pmmn	0	No	\	0	135	3.34E+07	mp-605028
Ti_2Te_2P	P-3m1	0	No	\	0	57	3.40E+07	mp-12527
Hf_3Te_2	P4/mmm	0	No	\	0	78	3.43E+07	mp-28919
$TiNbS_4$	P2/m	0	No	TiS_2 + NbS_2	23	93	3.44E+07	mp-34289
$NbTe_2$	P-3m1	0	No	$NbTe_2$	47	106	3.47E+07	mp-1018150
$TiBr_2$	P-3m1	0	No	Ti_7Br_{16} + Ti	38	61	3.50E+07	mp-27785
TiClO	Pmmn	0	No	Ti_2O_3 + $TiCl_3$	15	37	3.55E+07	mp-22992
$Ta(NiTe)_2$	Pmma	0	No	\	0	54	3.56E+07	mp-28667
$Sr_4Mn_3(ClO_4)_2$	P4/mmm	0	No	\	0	26	3.59E+07	mp-25033
$TiCl_2$	P-3m1	0	No	Ti_7Cl_{16} + Ti	55	90	3.63E+07	mp-28116
EuIO	P4/nmm	0	No	\	0	51	3.73E+07	mp-600622
$CeBiS_2O$	P4/nmm	0	No	$Ce_4S_3O_4$ + Bi_2S_3 + Bi	62	71	3.74E+07	mp-610469
LiCoAs	P4/nmm	0	No	\	0	157	3.74E+07	mp-20698
TiSCl	Pmmn	0	No	\	0	60	3.99E+07	mp-1013900
$Ca_3Cu_2(ClO_2)_2$	P4/mmm	0	No	Ca_4Cl_6O + $CaCu_3O_4$ + CaO	7	41	4.09E+07	mp-23095
In_3Te_4	P-3m1	0	No	In_4Te_3 + In_7Te_{10}	36	51	4.11E+07	mp-541885
$Ca_3Cu_2(BrO_2)_2$	P4/mmm	0	No	\	0	26	4.16E+07	mp-545706
Bi_3Se_4	P-3m1	0	No	Bi_2Se_3 + Bi	55	53	4.17E+07	mp-542615
TiOF	Pmmn	0	No	Ti_2O_3 + TiF_3	71	47	4.27E+07	mp-753059
TmI_2	P-3m1	0	No	TmI_3 + Tm	50	90	4.34E+07	mp-29671
CuSe	P4/nmm	0	No	CuSe	71	117	4.36E+07	mp-580226
Sc_2NCl_2	P-3m1	0	No	\	0	41	4.39E+07	mp-28480
NiTe	P-3m1	0	No	Ni_3Te_2 + $NiTe_2$	43	125	4.56E+07	mp-10264
$PtPb_4$	P4/nbm	0	No	\	0	185	4.58E+07	mp-21296
Zr_2Te_2P	P-3m1	0	No	\	0	66	4.67E+07	mp-16765
$NiTe_2$	P-3m1	0	No	\	0	171	4.68E+07	mp-2578
Li_2H_2Pd	P4/mmm	0	No	\	0	109	4.72E+07	mp-644389
PtTe	P-3m1	0	No	\	0	145	4.86E+07	mp-11693
SrCu	P6/mmm	0	No	\	0	180	4.91E+07	mp-1025402
Nb_2CS_2	P-3m1	186	No	Nb_3S_4 + Nb_6C_5 + C	22	54	4.96E+07	mp-4384
ZrSiTe	P4/nmm	0	No	\	0	64	5.12E+07	mp-19917

ZrSiSe	P4/nmm	0	No	\	0	84	5.34E+07	mp-4628
$OsCl_2O$	Pmmm	0	No	\	0	67	5.45E+07	mp-29133
HfSiSe	P4/nmm	0	No	\	0	78	5.50E+07	mp-13962
ZrGeTe	P4/nmm	0	No	\	0	71	5.51E+07	mp-3208
$RuCl_2O$	Pmmm	0	No	\	0	64	5.54E+07	mp-29132
Li_2H_2Pt	P4/mmm	0	No	\	0	108	5.56E+07	mp-644136
YCBr	C2/m	0	No	\	0	34	5.58E+07	mp-643367
$SiTe_2$	P-3m1	0	No	Te + Si	53	91	5.63E+07	mp-2755
TbCBr	C2/m	0	No	\	0	39	5.67E+07	mp-1025023
HfSiTe	P4/nmm	0	No	\	0	63	5.69E+07	mp-13963
Ta_2CS_2	P-3m1	22	No	\	0	42	5.94E+07	mp-7814
$CeTe_3$	P4/nmm	0	No	\	0	62	6.11E+07	mp-571571
$ZrTe_3$	Pmmn	0	No	\	0	95	6.22E+07	mp-2089
LiC_{12}	P6/mmm	0	No	\	0	38	6.31E+07	mp-1021323
$HfTe_3$	Pmmn	0	No	$HfTe_5$ + $HfTe_2$	25	88	6.54E+07	mp-1025459
CuTe	Pmmn	0	No	\	0	79	9.05E+07	mp-20826
$CuAgTe_2$	Pmm2	0	No	Ag_2Te + CuTe + Te	70	93	1.16E+08	mp-2977
$LaTe_3$	P4/nmm	0	No	\	0	57	1.47E+08	mp-1078612
Nd_2Te_5	P4/nmm	0	No	\	0	29	1.60E+08	mp-1119
$PrTe_3$	P4/nmm	0	No	\	0	56	1.60E+08	mp-12351
$NdTe_3$	P4/nmm	0	No	\	0	55	1.60E+08	mp-740
$SmTe_3$	P4/nmm	0	No	\	0	57	1.64E+08	mp-9399
$TbTe_3$	P4/nmm	0	No	\	0	57	1.73E+08	mp-1084847
$LuTe_3$	P4/nmm	0	No	Lu_2Te_3 + Te	9	58	1.73E+08	mp-1080689
$ErTe_3$	P4/nmm	0	No	\	0	57	1.74E+08	mp-1078991
$TmTe_3$	P4/nmm	0	No	\	0	57	1.74E+08	mp-1087512
$HoTe_3$	P4/nmm	0	No	\	0	57	1.75E+08	mp-1078508
$DyTe_3$	P4/nmm	0	No	\	0	57	1.76E+08	mp-1086673
YTe_3	P4/nmm	0	No	\	0	61	1.78E+08	mp-945077
$PrTe_2Se$	P4/nmm	0	No	\	0	52	1.87E+08	mp-30125
$NdTe_2Se$	P4/nmm	0	No	\	0	51	1.91E+08	mp-4437
$LaTe_2Se$	P4/nmm	0	No	\	0	44	2.09E+08	mp-4034

Table S3. Computed free energy of reaction species (with consideration of the effect of solvation), including ΔG (OOH*), ΔG (O*), and ΔG (OH*), theoretical limiting potential (U_L) and potential limiting step (PDS) for the ORR and OER on the 242 possible sites in the 199 candidate materials which screened from catalytic selectivity analysis.

Formula	ΔG (OOH*)	ΔG (O*)	ΔG (OH*)	PDS-ORR	U_L (ORR)	PDS-OER	U_L (OER)
$NbTe_2$	3.95	2.00	0.66	OH*↔H_2O	0.66	OOH*↔O*	1.96
HfSiSe	3.94	1.34	0.48	OH*↔H_2O	0.48	OOH*↔O*	2.60
$HfTe_5$_1	4.59	1.47	1.40	O*↔OH*	0.06	OOH*↔O*	3.12
$HfTe_5$_2	4.87	1.86	1.60	O_2↔OOH*	0.05	OOH*↔O*	3.02
Nb_2PdS_6_1	4.49	1.86	1.17	O_2↔OOH*	0.43	OOH*↔O*	2.64
Nb_2PdS_6_2	4.61	1.97	1.64	O_2↔OOH*	0.31	OOH*↔O*	2.65
$TiTe_2$	4.66	1.47	1.35	O*↔OH*	0.13	OOH*↔O*	3.19
$TiSe_2$	4.64	1.81	1.55	O*↔OH*	0.26	OOH*↔O*	2.83
Ta_2NiS_5	4.73	2003	1.60	O_2↔OOH*	0.19	OOH*↔O*	2.70
Ta_2Te_3	4.67	1.69	1.62	O_2↔OOH*	0.08	OOH*↔O*	2.97
$TaSe_3$	4.44	2.08	1.26	O_2↔OOH*	0.48	OOH*↔O*	2.36
$NbNiTe_5$	4.39	1.73	1.39	O*↔OH*	0.34	OOH*↔O*	2.66
ZrSiSe	4.12	1.58	0.71	OH*↔H_2O	0.71	OOH*↔O*	2.54
$TaNiTe_5$	4.49	1.58	1.33	O*↔OH*	0.26	OOH*↔O*	2.91
Ta_2NiSe_5	4.85	2.02	1.58	O_2↔OOH*	0.07	OOH*↔O*	2.83
TaS_3	4.63	2.07	1.83	O*↔OH*	0.24	OOH*↔O*	2.56
ZrGeTe	4.02	1.18	0.59	OH*↔H_2O	0.59	OOH*↔O*	2.84
FeSe	4.17	1.65	0.49	OH*↔H_2O	0.49	OOH*↔O*	2.52
FeS	4.67	1.53	1.43	O*↔OH*	0.11	OOH*↔O*	3.14
$NbCrSe_5$	4.38	1.75	0.76	OH*↔H_2O	0.54	OOH*↔O*	2.63
TaS_2	4.12	1.65	0.70	OH*↔H_2O	0.70	OOH*↔O*	2.48
NbS_2	3.95	1.55	0.57	OH*↔H_2O	0.57	OOH*↔O*	2.40
$NbCoTe_2$	4.28	1.64	1.13	O*↔OH*	0.51	OOH*↔O*	2.64
Nb_3IrSe_8	4.25	1.74	1.22	O*↔OH*	0.51	OOH*↔O*	2.51
VTe_2	3.85	1.93	0.57	OH*↔H_2O	0.57	OOH*↔O*	1.92
$Te_2Pd_3Pb_2$	3.70	1.97	0.50	OH*↔H_2O	0.50	OOH*↔O*	1.73
CoSe	4.38	1.93	1.23	O_2↔OOH*	0.54	OOH*↔O*	2.45
$TaTe_2$	3.55	1.77	0.29	OH*↔H_2O	0.29	OOH*↔O*	1.79
Te_2Mo	4.09	1.95	0.82	OH*↔H_2O	0.82	OOH*↔O*	2.13
VTe_2	3.09	1.07	-0.10	OH*↔H_2O	-0.10	OOH*↔O*	2.02
ScCl	5.09	1.63	2.42	O*↔OH*	-0.78	OOH*↔O*	3.46
$TiNbS_4$	4.54	1.74	1.34	O_2↔OOH*	0.38	OOH*↔O*	2.80
$TaFeTe_3$	4.07	1.34	0.76	OH*↔H_2O	0.58	OOH*↔O*	2.73
Nb_3IrS_8_1	4.44	1.50	1.09	O*↔OH*	0.42	OOH*↔O*	2.94
Nb_3IrS_8_2	4.53	1.60	1.50	O*↔OH*	0.10	OOH*↔O*	2.93
MnSe	4.70	1.54	1.58	O*↔OH*	-0.04	OOH*↔O*	3.16

$Mn(InSe_2)_2$_1	3.34	0.45	0.63	O*↔OH*	-0.18	OOH*↔O*	2.89
$Mn(InSe_2)_2$_2	4.27	1.84	1.12	O_2↔OOH*	0.65	OOH*↔O*	2.43
TePt	4.02	1.83	0.80	OH*↔H_2O	0.80	OOH*↔O*	2.20
NiTe	4.09	2.00	0.88	O_2↔OOH*	0.83	OOH*↔O*	2.09
$Mn_2Ga_2S_5$	4.84	1.94	2.58	O*↔OH*	-0.64	OOH*↔O*	2.90
$SiTe_2$	4.46	1.99	1.20	O_2↔OOH*	0.46	OOH*↔O*	2.47
$PtPb_4$_1	3.68	1.28	0.47	OH*↔H_2O	0.47	OOH*↔O*	2.40
$PtPb_4$_2	3.65	1.83	0.65	OH*↔H_2O	0.65	OOH*↔O*	1.82
$NiTe_2$	4.01	1.60	0.76	OH*↔H_2O	0.76	OOH*↔O*	2.41
Fe_4S_5	3.93	1.83	0.70	OH*↔H_2O	0.70	OOH*↔O*	2.10
$CoTe_2$	3.49	1.02	0.04	OH*↔H_2O	0.04	OOH*↔O*	2.47
$CeBiS_2O$	3.20	0.98	-0.13	OH*↔H_2O	-0.13	OOH*↔O*	2.21
$Cr(GaS_2)_2$	3.53	1.15	0.12	OH*↔H_2O	0.12	OOH*↔O*	2.39
KFe_2Se_3	3.86	0.90	0.64	O*↔OH*	0.25	OOH*↔O*	2.96
Bi_9I_2_1	3.87	1.22	0.69	O*↔OH*	0.53	OOH*↔O*	2.65
Bi_9I_2_2	3.79	1.83	0.62	OH*↔H_2O	0.62	OOH*↔O*	1.96
$LiCu_2(CO_3)_2$	2.59	1.57	-0.53	OH*↔H_2O	-0.53	O_2↔OOH*	2.33
$CuAgTe_2$_1	3.73	1.44	0.35	OH*↔H_2O	0.35	OOH*↔O*	2.29
$CuAgTe_2$_2	3.70	1.50	0.37	OH*↔H_2O	0.37	OOH*↔O*	2.19
CuSe	4.42	1.98	1.23	O_2↔OOH*	0.50	OOH*↔O*	2.44
Na_2HfN_2	2.00	1.42	-1.20	OH*↔H_2O	-1.20	O_2↔OOH*	2.92
Bi_4I_1	3.84	1.83	0.67	OH*↔H_2O	0.67	OOH*↔O*	2.01
Bi_4I_2	3.95	1.92	0.82	OH*↔H_2O	0.82	OOH*↔O*	2.02
VCl_3	4.81	2.10	3.03	O*↔OH*	-0.94	OOH*↔O*	2.72
$TaCoTe_2$	4.38	1.58	1.25	O*↔OH*	0.33	OOH*↔O*	2.80
$ZrTe_5$_1	4.55	1.60	1.40	O*↔OH*	0.20	OOH*↔O*	2.95
$ZrTe_5$_2	4.86	1.86	1.68	O_2↔OOH*	0.06	OOH*↔O*	3.00
$TaTe_4Ir$	4.36	1.91	1.16	O_2↔OOH*	0.56	OOH*↔O*	2.44
TiS_2	4.71	1.90	1.36	O_2↔OOH*	0.21	OOH*↔O*	2.80
VS_2	4.37	1.65	0.91	O_2↔OOH*	0.55	OOH*↔O*	2.72
$NbTe_4Ir$	4.41	1.98	1.21	O_2↔OOH*	0.51	OOH*↔O*	2.43
$LiNi(PS_3)_2$	4.31	1.72	0.99	O_2↔OOH*	0.61	OOH*↔O*	2.60
$SrSbSe_2F$	4.24	1.60	1.04	O*↔OH*	0.57	OOH*↔O*	2.63
Te_2W	4.33	1.97	0.93	O_2↔OOH*	0.59	OOH*↔O*	2.36
$VAg(PSe_3)_2$	3.92	1.34	0.60	OH*↔H_2O	0.60	OOH*↔O*	2.58
Ta_2PdS_6	4.76	1.99	1.42	O_2↔OOH*	0.16	OOH*↔O*	2.76
TiS_3	4.72	1.80	1.83	O*↔OH*	-0.03	OOH*↔O*	2.91
$Ge_5(Te_4As)_2$	4.24	1.73	1.04	O_2↔OOH*	0.68	OOH*↔O*	2.50
Pr_2Br_5_1	2.66	0.57	-0.89	OH*↔H_2O	-0.89	O_2↔OOH*	2.26
Pr_2Br_5_2	3.29	1.28	-0.28	OH*↔H_2O	-0.28	OOH*↔O*	2.01
Pr_2Br_5_3	3.66	1.87	0.22	OH*↔H_2O	0.22	OOH*↔O*	1.79
Pr_2Br_5_4	3.73	1.06	-0.16	OH*↔H_2O	-0.16	OOH*↔O*	2.67
$HfSe_3$	4.76	1.69	1.63	O*↔OH*	0.05	OOH*↔O*	3.07

NbS_3	4.70	2.04	1.52	O_2↔OOH*	0.22	OOH*↔O*	2.65
$Ge_4Te_7As_2$	4.32	1.83	1.17	O_2↔OOH*	0.60	OOH*↔O*	2.49
$ZrSe_3$	4.78	1.75	1.21	O_2↔OOH*	0.14	OOH*↔O*	3.03
$ZrSe_2$	4.76	1.75	1.34	O_2↔OOH*	0.16	OOH*↔O*	3.01
$CuBrO_2$	4.30	1.69	1.79	O*↔OH*	-0.09	OOH*↔O*	2.61
In_2Se_3	4.35	1.51	1.09	O*↔OH*	0.42	OOH*↔O*	2.83
Ti_2Te_2P	4.67	1.82	1.35	O_2↔OOH*	0.25	OOH*↔O*	2.85
Zr_2Te_2P	4.77	1.74	1.55	O_2↔OOH*	0.15	OOH*↔O*	3.02
$Ta_2Te_5Pd_3$_1	4.20	1.64	1.05	O*↔OH*	0.59	OOH*↔O*	2.55
$Ta_2Te_5Pd_3$_2	4.70	2.44	1.36	O_2↔OOH*	0.22	OOH*↔O*	2.25
Ta_4AgS_8	4.48	1.94	1.14	O_2↔OOH*	0.44	OOH*↔O*	2.54
$Ag(TeMo)_6$	4.40	1.62	1.20	O*↔OH*	0.42	OOH*↔O*	2.78
Ta_3SiTe_6	4.61	1.57	1.42	O*↔OH*	0.15	OOH*↔O*	3.04
$NbSe_2$	4.12	2.13	0.83	O_2↔OOH*	0.80	OOH*↔O*	1.99
BiTe	4.28	1.78	1.09	O_2↔OOH*	0.64	OOH*↔O*	2.50
$Ta_3Te_{14}Pd_3$_1	4.26	1.78	1.10	O_2↔OOH*	0.66	OOH*↔O*	2.48
$Ta_3Te_{14}Pd_3$_2	4.16	1.81	1.15	O_2↔OOH*	0.76	OOH*↔O*	2.35
$Ta_3Te_{14}Pd_3$_3	4.28	1.93	1.06	O_2↔OOH*	0.64	OOH*↔O*	2.35
Nb_3SiTe_6	4.58	1.85	1.40	O_2↔OOH*	0.34	OOH*↔O*	2.73
Nb_3GeTe_6	4.51	1.27	1.24	O*↔OH*	0.03	OOH*↔O*	3.24
$Bi_2Rh_3S_2$	3.76	1.73	0.53	OH*↔H_2O	0.53	OOH*↔O*	2.03
$Ge_3(BiTe_3)_2$	4.64	1.34	1.45	O*↔OH*	-0.11	OOH*↔O*	3.30
Nb_4IrSe_{10}_1	4.29	1.21	1.61	O*↔OH*	-0.40	OOH*↔O*	3.08
Nb_4IrSe_{10}_2	4.26	2.26	1.43	O_2↔OOH*	0.66	OOH*↔O*	2.00
Nb_4IrSe_{10}_3	4.85	2.55	1.45	O_2↔OOH*	0.07	OOH*↔O*	2.60
KFe_2S_3	3.96	0.97	0.88	O*↔OH*	0.09	OOH*↔O*	2.98
Nb_9IrSe_{20}_1	4.55	2.02	1.40	O_2↔OOH*	0.37	OOH*↔O*	2.53
Nb_9IrSe_{20}_2	4.80	2.31	1.85	O_2↔OOH*	0.12	OOH*↔O*	2.48
Nb_9IrSe_{20}_3	4.19	2.27	0.93	O_2↔OOH*	0.73	OOH*↔O*	1.91
CeZnPO	3.12	1.22	0.04	OH*↔H_2O	0.04	OOH*↔O*	1.90
Bi_3Se_4	3.61	1.70	0.32	OH*↔H_2O	0.32	OOH*↔O*	1.91
$Bi_2Te_5Pb_2$	4.59	1.78	1.24	O_2↔OOH*	0.33	OOH*↔O*	2.80
Na_2ZrN_2	1.97	1.30	-1.19	OH*↔H_2O	-1.19	O_2↔OOH*	2.95
$CuTeO_3$	4.17	2.06	0.94	O*↔OH*	0.75	OOH*↔O*	2.11
$TiFeTe_6$_1	4.85	1.70	1.63	O*↔OH*	0.07	OOH*↔O*	3.14
$TiFeTe_6$_2	4.67	1.82	1.57	O*↔OH*	0.24	OOH*↔O*	2.86
$TiFeTe_6$_3	4.53	1.96	1.28	O_2↔OOH*	0.39	OOH*↔O*	2.57
$TiFeTe_6$_4	4.39	2.10	1.07	O_2↔OOH*	0.53	OOH*↔O*	2.29
$TbTe_3$	4.77	2.61	2.09	O_2↔OOH*	0.15	OOH*↔O*	2.16
$PrTe_3$	4.81	2.52	1.98	O_2↔OOH*	0.11	OOH*↔O*	2.29
Nd_2Te_5	4.79	2.47	1.66	O_2↔OOH*	0.13	OOH*↔O*	2.32
TbGaI	4.24	2.71	0.85	O_2↔OOH*	0.68	O*↔OH*	1.85
HfSiTe	4.19	0.70	0.79	O*↔OH*	-0.09	OOH*↔O*	3.48

$HoTe_3$	4.70	2.62	1.66	O_2↔OOH*	0.22	OOH*↔O*	2.08
LiC_{12}	4.53	2.14	1.18	O_2↔OOH*	0.39	OOH*↔O*	2.39
$TaNiTe_2$	4.63	2.24	1.29	O_2↔OOH*	0.29	OOH*↔O*	2.39
ZrCl	4.77	2.34	1.62	O_2↔OOH*	0.15	OOH*↔O*	2.43
ZrSiTe	4.28	0.96	0.93	O*↔OH*	0.03	OOH*↔O*	3.32
CuTe	4.43	2.21	1.31	O_2↔OOH*	0.49	OOH*↔O*	2.22
NdI_2	3.76	0.11	0.29	OH*↔H_2O	-0.18	OOH*↔O*	3.65
Ta_2Se	3.54	0.94	0.35	OH*↔H_2O	0.35	OOH*↔O*	2.60
$NdTe_3$	4.49	2.55	2.01	O_2↔OOH*	0.13	OOH*↔O*	2.24
$NbSe_3$	4.73	2.55	1.78	O_2↔OOH*	0.19	OOH*↔O*	2.17
$TaNi_2TeSe$	4.73	2.64	1.29	O_2↔OOH*	0.19	OOH*↔O*	2.09
$SmTe_3$	4.79	2.59	2.07	O_2↔OOH*	0.13	OOH*↔O*	2.20
$HfTe_2$	4.81	0.24	1.05	O*↔OH*	-0.81	OOH*↔O*	4.57
La_2PI_2	4.28	2.37	0.87	O_2↔OOH*	0.64	OOH*↔O*	1.91
$NdTe_2Se$	4.75	2.46	1.44	O_2↔OOH*	0.17	OOH*↔O*	2.29
$Ca(TiS_2)_8$	4.72	2.16	1.38	O_2↔OOH*	0.20	OOH*↔O*	2.56
VSe_2	4.86	2.25	0.94	O_2↔OOH*	0.06	OOH*↔O*	2.61
$PrTe_2Se$	4.76	2.44	1.42	O_2↔OOH*	0.16	OOH*↔O*	2.32
CrS_2	2.58	0.09	-0.66	OH*↔H_2O	-0.66	OOH*↔O*	2.49
YTe_3	4.76	2.60	1.64	O_2↔OOH*	0.16	OOH*↔O*	2.15
EuBrO	3.74	1.92	1.88	O*↔OH*	0.04	OH*↔H_2O	1.88
$TaNi_2Te_3$	4.58	1.17	1.48	O*↔OH*	-0.31	OOH*↔O*	3.41
$Ta(NiTe)_2$	4.62	2.71	1.46	O_2↔OOH*	0.30	OOH*↔O*	1.91
$ErTe_3$	4.75	2.61	1.50	O_2↔OOH*	0.17	OOH*↔O*	2.13
$TaTe_5Pt$_1	4.48	2.24	1.23	O_2↔OOH*	0.44	OOH*↔O*	2.23
$TaTe_5Pt$_2	4.81	2.28	1.48	O_2↔OOH*	0.11	OOH*↔O*	2.53
$LaTe_3$	4.61	2.47	1.88	O_2↔OOH*	0.31	OOH*↔O*	2.14
$LaTe_2Se$	4.56	2.39	1.30	O_2↔OOH*	0.36	OOH*↔O*	2.17
$CeTe_3$	4.96	2.65	1.45	O_2↔OOH*	-0.04	OOH*↔O*	2.30
$NbTe_5Pd$_1	4.47	2.15	1.14	O_2↔OOH*	0.45	OOH*↔O*	2.32
$NbTe_5Pd$_2	4.44	2.22	1.53	O_2↔OOH*	0.48	OOH*↔O*	2.22
$TiBr_3$	4.04	0.27	0.81	O*↔OH*	-0.53	OOH*↔O*	3.76
$TaSe_2$	4.18	2.17	0.90	O_2↔OOH*	0.74	OOH*↔O*	2.01
$TiCl_3$	4.94	0.20	0.30	O*↔OH*	-0.10	OOH*↔O*	4.74
$ZrTe_3$	4.64	1.27	1.17	O*↔OH*	0.10	OOH*↔O*	3.37
AuSe	4.80	2.57	1.81	O_2↔OOH*	0.12	OOH*↔O*	2.23
TbBr	4.03	2.18	0.56	OH*↔H_2O	0.56	OOH*↔O*	1.85
$TaTe_2$	3.79	0.49	0.57	O*↔OH*	-0.09	OOH*↔O*	3.30
CoI_2	3.48	0.67	0.49	O*↔OH*	0.18	OOH*↔O*	2.81
$CuSeO_3$	4.84	2.60	1.58	O_2↔OOH*	0.08	OOH*↔O*	2.23
VTe_2	3.09	1.07	-0.10	OH*↔H_2O	-0.10	OOH*↔O*	2.02
$HfTe_3$	4.54	1.02	0.86	O*↔OH*	0.16	OOH*↔O*	3.52
$ZrTiTe_4$	4.67	0.34	1.36	O*↔OH*	-1.02	OOH*↔O*	4.33

$NbFeTe_2$	3.64	0.68	0.35	O*↔OH*	0.33	OOH*↔O*	2.96
Li_2H_2Pt	2.12	0.27	-0.80	OH*↔H_2O	-0.80	O_2↔OOH*	2.80
$VAg(PS_3)_2$	4.27	0.89	0.74	O*↔OH*	0.15	OOH*↔O*	3.38
Nb_2Te_3_1	3.23	0.17	0.04	OH*↔H_2O	0.04	OOH*↔O*	3.06
Nb_2Te_3_2	4.77	2.34	1.67	O_2↔OOH*	0.15	OOH*↔O*	2.43
$AgHO_2$	3.70	2.38	1.21	O*↔OH*	1.17	OOH*↔O*	1.32
$NbTe_2$	2.19	0.32	-0.39	OH*↔H_2O	-0.39	O_2↔OOH*	2.73
KV_4O_{10}	2.90	1.25	-0.26	OH*↔H_2O	-0.26	O_2↔OOH*	2.02
TmI_2	2.84	0.60	-0.58	OH*↔H_2O	-0.58	OOH*↔O*	2.24
Ga_2NiS_4	4.75	2.43	2.17	O_2↔OOH*	0.17	OOH*↔O*	2.32
LiCoAs	2.63	0.04	-0.63	OH*↔H_2O	-0.63	OOH*↔O*	2.59
V_6O_{13}	3.71	0.72	0.38	O*↔OH*	0.34	OOH*↔O*	2.99
$NiPSe_3$	3.61	0.21	0.32	O*↔OH*	-0.11	OOH*↔O*	3.40
$Ag(AuS)_2$_1	4.13	0.91	0.30	OH*↔H_2O	0.30	OOH*↔O*	3.21
$Ag(AuS)_2$_2	4.16	2.34	.01	O_2↔OOH*	0.76	OOH*↔O*	1.82
$CuSi_2P_3$_1	3.13	0.25	-0.25	OH*↔H_2O	-0.25	OOH*↔O*	2.88
$CuSi_2P_3$_2	4.44	0.66	0.88	O*↔OH*	-0.21	OOH*↔O*	3.78
Cr_3Te_4	4.64	0.96	1.34	O*↔OH*	-0.39	OOH*↔O*	3.68
Nb_2Se_3_1	3.02	0.11	-0.11	OH*↔H_2O	-0.11	OOH*↔O*	2.91
Nb_2Se_3_2	4.59	2.71	1.45	O_2↔OOH*	0.33	OOH*↔O*	1.88
Ta_2PtSe_7_1	4.75	2.05	2.13	O*↔OH*	-0.08	OOH*↔O*	2.70
Ta_2PtSe_7_2	4.58	2.42	1.49	O_2↔OOH*	0.34	OOH*↔O*	2.17
Ta_2PtSe_7_3	4.90	2.12	1.64	O_2↔OOH*	0.02	OOH*↔O*	2.78
Ta_2CS_2	4.81	2.28	1.88	O_2↔OOH*	0.11	OOH*↔O*	2.53
CeI_3_1	3.26	0.53	0.07	OH*↔H_2O	0.07	OOH*↔O*	2.73
CeI_3_2	3.29	1.44	0.79	O*↔OH*	0.65	OOH*↔O*	1.85
TiIN	4.73	2.33	2.70	O*↔OH*	-0.37	OH*↔H_2O	2.70
CrP_2S_7	4.29	0.85	0.54	O*↔OH*	0.31	OOH*↔O*	3.44
$FeBr_3$	4.80	2.63	1.80	O_2↔OOH*	0.12	OOH*↔O*	2.16
$CoBr_2$	4.87	2.55	2.35	O_2↔OOH*	0.05	OH*↔H_2O	2.35
$NiPS_3$	3.86	0.99	0.55	OH*↔H_2O	0.44	OOH*↔O*	2.87
$MnSbSe_2I$	4.06	1.25	0.63	O*↔OH*	0.62	OOH*↔O*	2.81
Ta_2PdSe_6_1	4.67	2.51	1.43	O_2↔OOH*	0.25	OOH*↔O*	2.16
Ta_2PdSe_6_2	4.86	2.58	1.77	O_2↔OOH*	0.06	OOH*↔O*	2.28
$HfFeCl_6$	2.40	2.18	0.24	OH*↔H_2O	0.24	OOH*↔O*	2.22
$MnSbSe_2Br$	3.50	0.36	-0.19	OH*↔H_2O	-0.19	OOH*↔O*	3.13
$MoCl_3$	3.99	0.77	1.75	O*↔OH*	-0.98	OOH*↔O*	3.22
$CuSeSe_2$	3.70	0.71	0.07	OH*↔H_2O	0.07	OOH*↔O*	2.99
$TaSe_2$	4.74	2.14	1.61	O_2↔OOH*	0.17	OOH*↔O*	2.61
CrI_2	4.79	1.32	1.94	O*↔OH*	-0.62	OOH*↔O*	3.47
$CrTe_3$_1	4.40	1.68	2.74	O*↔OH*	-1.06	OH*↔H_2O	2.74
$CrTe_3$_2	4.34	2.35	1.20	O_2↔OOH*	0.58	OOH*↔O*	1.99
Rb_2O	2.84	2.60	-0.17	OH*↔H_2O	-0.17	OOH*↔O*	2.77

$CuSbS_2$	3.80	0.85	0.12	OH*↔H_2O	0.12	OOH*↔O*	2.95
$CrPO_5$	4.67	2.74	2.78	O*↔OH*	-0.04	OH*↔H_2O	2.78
$Sc_6C_2I_{11}$	3.01	1.18	-0.44	OH*↔H_2O	-0.44	O_2↔OOH*	1.91
K_2As_2Pd	3.05	0.94	-0.07	OH*↔H_2O	-0.07	OOH*↔O*	2.11
Nb_2GeTe_4	4.87	2.74	1.67	O_2↔OOH*	0.05	OOH*↔O*	2.13
ZrI_2	4.74	0.34	2.27	O_2↔OOH*	-1.93	OOH*↔O*	4.40
$MnPSe_3$	3.86	1.24	0.58	OH*↔H_2O	0.58	OOH*↔O*	2.62
$PdSeO_3$	4.90	2.76	1.31	O_2↔OOH*	0.02	OOH*↔O*	2.13
$CrGeTe_3$	4.10	2.45	0.86	O_2↔OOH*	0.82	OOH*↔O*	1.64
$DyTe_3$	4.72	2.6	1.65	O_2↔OOH*	0.20	OOH*↔O*	2.11
$LuTe_3$	4.70	2.59	1.57	O_2↔OOH*	0.22	OOH*↔O*	2.11
$Na_3(TiS_2)_{10}$	4.75	2.17	1.39	O_2↔OOH*	0.17	OOH*↔O*	2.58
BiSe	3.96	2.70	0.68	OH*↔H_2O	0.68	O*↔OH*	2.02
Ta_2Se_3	2.84	0.87	0.47	O*↔OH*	0.39	O_2↔OOH*	2.08
In_3Te_4	4.59	2.52	1.28	O_2↔OOH*	0.33	OOH*↔O*	2.07
GdBr	4.19	1.91	0.61	OH*↔H_2O	0.61	OOH*↔O*	2.29
$Li_2Cr_3(CO_3)_6$_1	4.46	2.68	1.98	O_2↔OOH*	0.46	OH*↔H_2O	1.98
$Li_2Cr_3(CO_3)_6$_2	4.47	2.68	3.03	O*↔OH*	-0.35	OH*↔H_2O	3.03
$Zn(InS_2)_2$_1	4.36	2.22	0.67	O_2↔OOH*	0.56	OOH*↔O*	2.15
$Zn(InS_2)_2$_2	4.41	2.54	1.10	O_2↔OOH*	0.51	OOH*↔O*	1.87
$Ta_4Co_2PdSe_{12}$_1	4.83	2.28	1.81	O_2↔OOH*	0.09	OOH*↔O*	2.54
$Ta_4Co_2PdSe_{12}$_2	4.85	2.28	2.04	O_2↔OOH*	0.07	OOH*↔O*	2.57
$Ta_4Co_2PdSe_{12}$_3	4.69	2.71	1.80	O_2↔OOH*	0.23	OOH*↔O*	1.98
$CuH_2(SeO_3)_2$	4.20	2.50	1.77	O_2↔OOH*	0.72	OH*↔H_2O	1.77
$Li_2Cu_2F_5$_1	4.33	2.18	0.31	OH*↔H_2O	0.31	OOH*↔O*	2.14
$Li_2Cu_2F_5$_2	4.11	2.38	0.53	OH*↔H_2O	0.53	OOH*↔O*	1.73
$V_2P_4S_{13}$_1	3.45	0.56	-0.11	OH*↔H_2O	-0.11	OOH*↔O*	2.90
$V_2P_4S_{13}$_2	4.87	0.91	1.78	O*↔OH*	-0.87	OOH*↔O*	3.96
$V_2P_4S_{13}$_3	4.23	0.77	0.99	O*↔OH*	-0.2	OOH*↔O*	3.45
$V_2P_4S_{13}$_4	4.88	0.91	1.68	O*↔OH*	-0.77	OOH*↔O*	3.96
$V_2P_4S_{13}$_5	4.88	0.68	1.57	O*↔OH*	-0.89	OOH*↔O*	4.20
$V_2P_4S_{13}$_6	3.46	0.56	-0.10	OH*↔H_2O	-0.10	OOH*↔O*	2.90
$CuSeO_3$	4.13	2.12	1.13	O_2↔OOH*	0.79	OOH*↔O*	2.01
Nb_3I_8	4.75	2.03	1.92	O*↔OH*	0.11	OOH*↔O*	2.72

Table S4. Computed adsorption free energy of O* and H_2O_2* on the 25 candidate material surfaces. A solvation correction of -0.27 eV was included into H2O2 adsorption according to the previous study. [28]

Material	ΔG (O*, eV)	ΔG (H_2O_2*, eV)
ZrSiSe	1.58	3.52
$TaSe_2$	2.17	3.80
$NbSe_2$	2.13	3.79
Fe_4S_5	1.83	3.85
BiSe	2.70	3.66
TaS_2	1.65	3.77
Nb_9IrSe_{20}	2.02	3.77
Nb_4IrSe_{10}	2.26	3.53
$Mn(InSe_2)_2$	1.84	3.75
$NbTe_2$	2.00	3.68
BiTe	1.78	3.72
NiTe	2.00	3.77
$Ge_4Te_7As_2$	1.83	3.51
$MoTe_2$	1.95	3.66
$Ge_5(Te_4As)_2$	1.73	3.31
PtTe	1.83	3.79
$LiNi(PS_3)_2$	1.72	3.60
Bi_9I_2	1.83	3.47
$CuH_2(SeO_3)_2$	2.50	3.36
$AgHO_2$	2.38	2.46
$CuTeO_3$	2.06	3.04
Bi_4I	1.92	3.61
$PtPb_4$	1.83	3.63
$CuSeO_3$	2.12	3.11
$TaTe_2$	1.77	3.36

Table S5. The space group (SG), the lattice constants (a, and b in Å, α, β, and γ in °), and the MP material-id (mp-id) for all 47 materials which exhibit the basal plane activity for oxygen electrocatalysis from the screening. The Publications related to the experimental available compounds are also given.

Formula	mp-id	Crystal System	Space Group	a	b	α	β	γ	Reference for material synthesis
$VAg(PSe_3)_2$	mp-6543	monoclinic	C2	6.35	6.36	90.00	90.00	60.05	Materials Research Bulletin 1988, 23 1199-1209
$MnSbSe_2I$	mp-570268	monoclinic	C2/m	3.90	10.53	90.00	90.00	90.00	Solid State Sciences 2006, 8, 652-699
$CuSeO_3$	mp-22688	orthorhombic	Pbca	4.59	10.27	90.00	90.00	92.51	Crystalline Materials, 1986, 175, 61-72
Bi_4I	mp-583234	monoclinic	C2/m	4.43	13.25	90.00	90.00	90.00	Eur. J. Inorg. Chem., 2008: 5196-5202.
$CuTeO_3$	mp-558696	monoclinic	P21/c	7.33	8.64	90.00	90.42	90.00	Journal of Solid State Chemistry, 1987, 291-295
Bi_9I_2	mp-28149	monoclinic	P21/m	4.44	13.28	90.00	90.00	90.00	Doklady Akademii Nauk SSSR 1990, 310, 117-120
$NiTe_2$	mp-2578	trigonal	P3m1	3.71	3.71	90.00	90.00	120.00	Bull. Soc. Chim. Belges, 1971, 80, 107-116.
$LiNi(PS_3)_2$	mp-557500	monoclinic	C2	5.82	5.84	90.00	90.00	60.14	Solid State Ionics 1984, 14, 45-49
$Ta_3Te_{14}Pd_3$	mp-505132	monoclinic	P21/m	3.74	21.80	90.00	90.00	90.00	Journal of Solid State Chemistry 1989, 78, 7-16

PtTe	mp-11693	trigonal	R-3m	3.92	3.92	90.00	90.00	60.00	Journal of the Less Common Metals 1969, 19, 121-140; Nano Res. 2021, 14, 1663–1667
$Ge_5(Te_4As)_2$	mp-28487	trigonal	P3m1	4.16	4.16	90.00	90.00	120.00	Acta Cryst. 1987, 43, 2268-2270
$MoTe_2$	mp-7459	monoclinic	P21/m	3.40	6.35	90.00	90.00	90.00	Acta Cryst. 1966, 20, 268-274
$Ge_4Te_7As_2$	mp-568730	trigonal	R3m	4.15	4.15	90.00	90.00	60.00	Journal of Solid State Chemistry 1988, 74, 277-286
NiTe	mp-10264	trigonal	R-3m	3.78	3.78	90.00	90.00	60.00	Sov. Phys. Crystallogr 1964, 8, 448-451
BiTe	mp-23224	trigonal	P3m1	4.43	4.43	90.00	90.00	120.00	Acta Cryst. 1979, 35, 147-149
$NbTe_2$	mp-11675	monoclinic	C2/m	3.43	9.79	90.00	90.00	79.90	Sci. Rep. 2018, 8, 16984
$Mn(InSe_2)_2$	mp-1078140	trigonal	R3m	4.10	4.10	90.00	90.00	60.00	Phys. Stat. Sol. A, 1991, 126, 237-244
Nb_4IrSe_{10}	mp-675326	triclinic	P1	6.01	9.12	90.00	90.00	72.31	N/A
TaS_2	mp-1984	hexagonal	P63/mmc	3.33	3.33	90.00	90.00	120.00	Acta Cryst. 1990, 46, 1598-1599
BiSe	mp-27902	trigonal	P3m1	4.22	4.22	90.00	90.00	120.00	Journal of Structural Chemistry 1967, 8, 584–589

Fe_4S_5	mp-850083	tetragonal	P4	7.88	7.88	90.00	90.00	90.00	N/A
$NbSe_2$	mp-7597	trigonal	R3m	3.45	3.45	90.00	90.00	60.00	Journal of Solid State Chemistry 1972, 4, 425-429
$TaSe_2$	mp-542495	triclinic	P1	3.46	3.46	90.00	90.00	120.00	Physica B+C 1980, 99, 51-55
ZrSiSe	mp-4628	tetragonal	P4/nmm	3.52	3.52	90.00	90.00	90.00	Recl. Trav. Chim. Pays-Bas 1964, 83, 776-783
GdBr	mp-1064427	trigonal	P3m1	3.78	3.78	90.00	90.00	120.00	N/A
$Sc_6C_2I_{11}$	mp-541102	triclinic	P1	9.05	16.16	90.00	90.00	83.11	N/A
$Li_2Cu_2F_5$	mp-762270	orthorhombic	Pnma	2.81	7.36	90.00	90.00	90.00	N/A
$Pd_3Pb_2Te_2$	mp-605028	orthorhombic	Pmmn	5.83	8.62	90.00	90.00	90.00	Canadian Mineralogist 2009, 47, 53–62.
$Zn(InS_2)_2$	mp-22253	trigonal	P3m1	3.89	3.89	90.00	90.00	120.00	J. Am. Chem. Soc. 2017, 139, 22, 7586–7594
$Ta(NiTe)_2$	mp-28667	orthorhombic	Pnma	3.51	6.44	90.00	90.00	90.00	Angew. Chem. Int. Ed. 1992, 31: 217-220
VTe_2	mp-11687	monoclinic	C2/m	3.36	9.44	90.00	90.00	79.75	Journal of Solid State Chemistry 1984, 53, 415-421

Bi_3Se_4	mp-542615	trigonal	R-3m	4.30	4.30	90.00	90.00	60.00	Dokl. AN SSSR, 1955, 100, 1079-1082; Nanotechnology 2018, 29, 085401
$TaTe_2$	mp-601823	monoclinic	C2/m	3.53	9.72	90.00	90.00	79.60	J. Phys.: Condens. Matter 1998, 10, 761
Nb_2Se_3	mp-2330	monoclinic	P21/m	3.38	9.81	90.00	90.00	90.00	Acta Cryst. 1968, 24, 1102-1106
Pr_2Br_5	mp-23169	monoclinic	P21/m	4.11	15.75	90.00	90.00	90.00	Journal of Solid State Chemistry 1991, 95, 1-13
CeZnPO	mp-13207	trigonal	R-3m	3.93	3.93	90.00	90.00	60.00	Z. Anorg. Allg. Chem., 2008, 634, 1339-1348.
EuBrO	mp-504727	tetragonal	P4/nmm	3.77	3.77	90.00	90.00	90.00	Z. Anorg. Allg. Chem. 1965, 338: 250-265
TbBr	mp-27924	trigonal	R-3m	3.79	3.79	90.00	90.00	60.00	Z. Anorg. Allg. Chem. 1980, 466, 7-22
$CrGeTe_3$	mp-541449	trigonal	R3	6.85	6.85	90.00	90.00	60.00	J. Am. Chem. Soc. 2020, 142, 9, 4438–4444
$PtPb_4$	mp-21296	tetragonal	P4/nbm	6.79	6.79	90.00	90.00	90.00	Phys. Rev. B 2021, 104, 125127
$CuH_2(SeO_3)_2$	mp-24164	monoclinic	P21/c	7.03	8.62	90.00	90.00	90.00	Zeitschrift für Kristallographie -

									Crystalline Materials. 2001, 216, 99-104
$Ag(AuS)_2$	mp-35835	monoclinic	Pc	4.29	7.16	90.00	90.00	90.00	N/A
Nb_9IrSe_{20}	mp-675290	triclinic	P-1	6.91	15.10	90.00	90.00	83.51	N/A
$AgHO_2$	mp-996958	monoclinic	Cm	5.42	5.48	90.00	90.00	80.84	N/A
La_2PI_2	mp-571647	trigonal	P-3m1	4.30	4.30	90.00	90.00	120.00	Zeitschrift für Naturforschung B, 2007, 62, 11, 2007, 1377-1382
TbGaI	mp-1025099	trigonal	P-3m1	4.18	4.18	90.00	90.00	120.00	N/A
CeI_3	mp-1025426	orthorhombic	Cmcm	4.33	10.10	90.00	90.00	90.00	N/A

Table S6. Adsorption free energies (ΔG) of the OOH*, O*, and OH* species, and the corresponding limiting potentials (U_L) for the ORR and OER on 77 built edges. The unit for adsorption energy and limiting potential are eV, and V, respectively. The major adsorption site is highlighted by red cycle.

Material	edge configuration	ΔG (OOH*)	ΔG (O*)	ΔG (OH*)	U_L (ORR)	PDS of ORR	U_L (OER)	PDS of OER	Active?
ZrSiSe	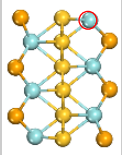	-4.23	-2.29	-2.29	-2.29	OH*↔H_2O	9.15	OOH*↔O_2	No
$TaSe_2$	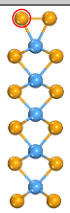	4.55	2.29	1.33	0.37	O_2↔OOH*	2.26	O*↔OOH*	No
	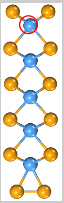	3.64	0.92	0.42	0.42	OH*↔H_2O(l)	2.72	O*↔OOH*	No
	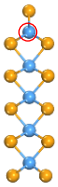	3.81	0.40	0.52	-0.11	O_2↔OOH*	3.41	O*↔OOH*	No
$NbSe_2$	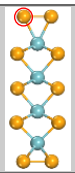	4.40	1.86	1.20	0.52	O_2↔OOH*	2.54	O↔OOH	No
	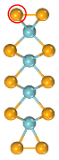	5.26	1.81	0.69	-0.34	O_2↔OOH*	3.46	O*↔OOH*	No
	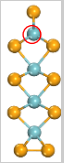	4.03	0.56	0.53	0.03	O*↔OH*	3.47	O*↔OOH*	No
Fe_4S_5	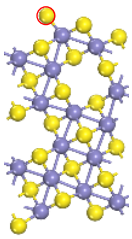	3.72	1.53	0.82	0.71	O*↔OH*	2.19	O*↔OOH*	ORR

	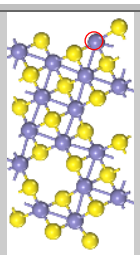	3.35	1.82	0.02	0.02	OH*↔H_2O	1.80	OH*↔O*	No
BiSe	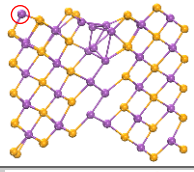	3.38	0.46	0.05	0.05	OH*↔H_2O	2.92	O*↔OOH*	No
	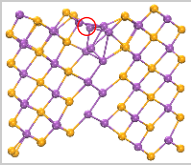	3.31	2.50	0.78	0.78	OH*↔H_2O	1.72	OH*↔O*	ORR&OER
	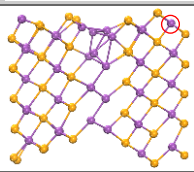	3.44	2.29	0.08	0.08	OH*↔H_2O	2.21	OH*↔O*	No
	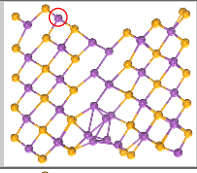	3.63	2.20	0.27	0.27	OH*↔H_2O	1.94	OH*↔O*	No
	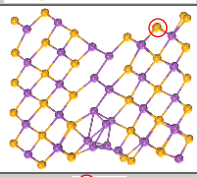	4.30	2.46	1.16	0.62	O_2↔OOH*	1.84	O*↔OOH*	ORR&OER
TaS_2	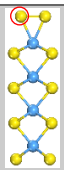	4.74	0.57	0.79	-0.22	O*↔OH*	4.16	O*↔OOH*	No
	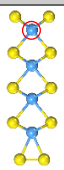	3.28	0.01	-0.90	-0.90	OH*↔H_2O	3.27	O*↔OOH*	No
	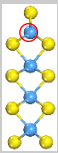	3.92	0.78	0.72	0.06	O*↔OH*	3.14	O*↔OOH*	No
Nb_9IrSe_{20}		4.02	0.68	0.88	-0.20	O*↔OH*	3.34	O*↔OOH*	No

	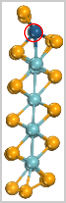	3.51	1.86	0.40	0.40	OH*↔H_2O	1.65	O*↔OOH*	OER
	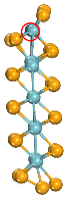	2.91	-0.63	-0.76	-0.76	OH*↔H_2O	3.55	O*↔OOH*	No
Nb_4IrSe_{10}	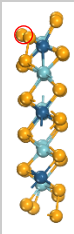	3.60	0.89	0.32	0.32	OH*↔H_2O	2.71	O*↔OOH*	No
	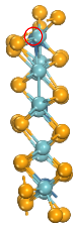	3.27	0.01	-0.25	-0.25	OH*↔H_2O	3.26	O*↔OOH*	No
	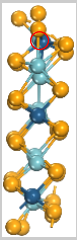	4.04	2.57	1.14	0.88	O_2↔OOH*	1.48	O*↔OOH*	ORR&OER
$Mn(InSe_2)_2$	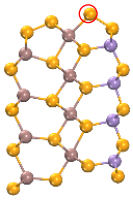	4.05	1.54	1.18	0.37	O*↔OH*	2.51	O*↔OOH*	No
	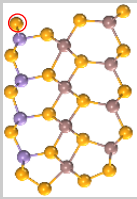	2.89	0.68	-0.45	-0.45	OH*↔H_2O	2.21	O*↔OOH*	No
	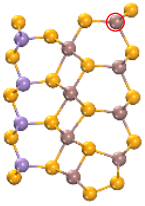	3.54	0.39	0.72	-0.33	O*↔OH*	3.15	O*↔OOH*	No

	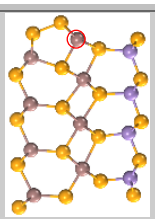	2.50	0.61	-0.73	-0.73	OH*↔H_2O	2.42	OOH*↔O_2	No
	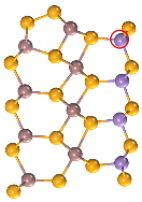	4.18	1.90	-0.41	-0.41	OH*↔H_2O	2.43	O*↔OOH*	No
$NbTe_2$	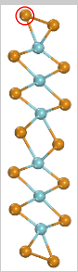	3.78	1.46	0.35	0.35	OH*↔H_2O	2.33	O*↔OOH*	No
	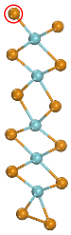	3.21	0.57	-0.01	-0.01	OH*↔H_2O	2.64	O*↔OOH*	No
	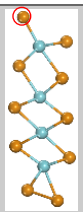	3.44	0.21	0.37	-0.16	O*↔OH*	3.23	O*↔OOH*	No
	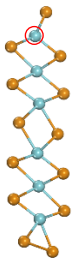	3.44	0.36	0.01	0.01	OH*↔H_2O	3.08	O*↔OOH*	No
	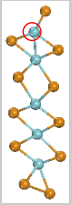	3.18	0.24	-0.14	-0.14	OH*↔H_2O	2.94	O*↔OOH*	No

	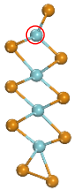	3.07	-0.15	-0.37	-0.37	OH*↔H_2O	3.22	O*↔OOH*	No
BiTe	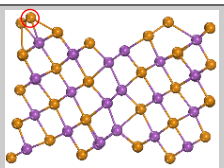	3.91	1.69	0.49	0.49	OH*↔H_2O	2.22	O*↔OOH*	No
	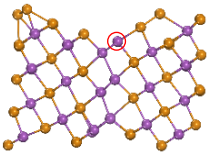	3.12	1.16	-0.13	-0.13	OH*↔H_2O	1.96	O*↔OOH*	No
	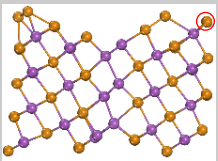	3.79	1.41	0.54	0.54	OH*↔H_2O	2.38	O*↔OOH*	No
	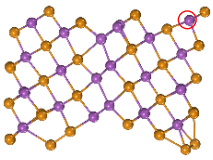	3.83	1.38	0.59	0.59	OH*↔H_2O	2.46	O*↔OOH*	No
	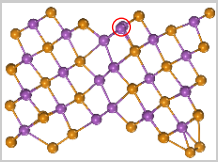	3.27	1.28	-0.01	-0.01	OH*↔H_2O	2.00	O*↔OOH*	No
NiTe	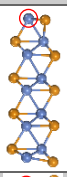	3.11	1.11	-0.62	-0.62	OH*↔H_2O	2.00	O*↔OOH*	No
	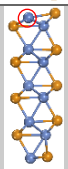	1.06	-0.15	-1.39	-1.39	OH*↔H_2O	4.16	O*+OH*↔O_2	No
$Ge_4Te_7As_2$	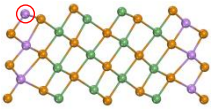	3.25	-0.06	-0.05	-0.05	OH*↔H_2O	3.31	O*↔OOH*	No
	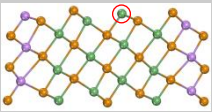	3.50	-0.34	-0.48	-0.48	OH*↔H_2O	3.84	O*↔OOH*	No
	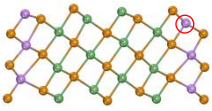	3.51	1.62	0.06	0.06	OH*↔H_2O	1.89	O*↔OOH*	No

	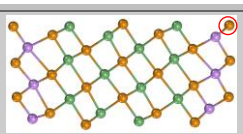	4.61	1.12	1.29	-0.16	O*↔OH*	3.48	O*↔OOH*	No
	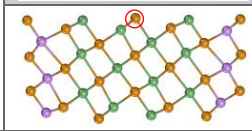	3.83	1.51	0.66	0.66	OH*↔H_2O	2.32	O*↔OOH*	ORR
$MoTe_2$	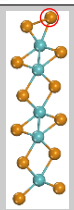	3.68	1.16	0.31	0.31	OH*↔H_2O	2.52	O*↔OOH*	No
	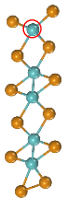	4.01	0.96	0.85	0.11	O*↔OH*	3.05	O*↔OOH*	No
	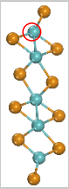	2.93	0.50	-0.32	-0.32	OH*↔H_2O	2.43	O*↔OOH*	No
		3.21	-0.42	0.52	-0.93	O*↔OH*	3.63	O*↔OOH*	No
$Ge_5(Te_4As)_2$	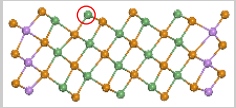	3.51	-0.14	-0.19	-0.19	OH*↔H_2O	3.65	O*↔OOH*	2.16
	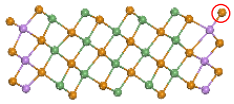	3.68	1.52	0.87	0.65	O*↔OH*	2.16	O*↔OOH*	ORR
	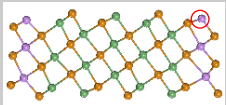	3.20	0.04	-0.17	-0.17	OH*↔H_2O	3.16	O*↔OOH*	No
PtTe	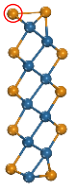	3.52	1.46	0.19	0.19	OH*↔H_2O	2.06	O*>OOH*	No

	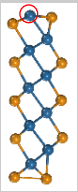	3.47	1.40	0.63	0.63	OH*↔H_2O	2.07	O*↔OOH*	ORR
$LiNi(PS_3)_2$	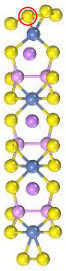	3.86	1.19	0.38	0.38	OH*↔H_2	2.66	O*↔OOH*	No
	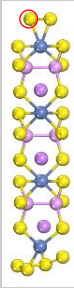	3.64	2.54	0.42	0.42	OH*↔H_2O	2.12	OH*↔O*	No
	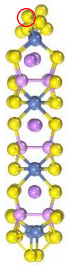	3.97	1.36	1.00	0.37	O*↔OH*	2.60	O*↔OOH*	No
	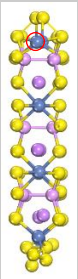	4.15	3.10	1.46	0.77	O_2↔OOH*	1.64	OH*↔O*	ORR&OER
Bi_9I_2	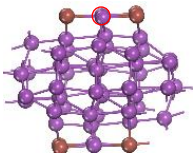	3.72	1.31	0.43	0.43	OH*↔H_2O	2.42	O*↔OOH*	No
	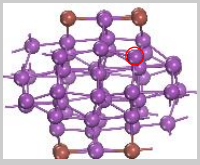	3.37	0.74	0.09	0.09	OH*↔H_2O	2.63	O*↔OOH*	No

$CuH_2(SeO_3)_2$	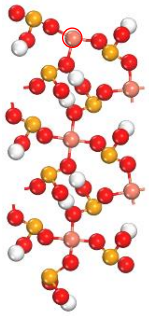	3.90	3.54	1.19	0.36	OOH*↔O*	2.64	OH*↔O*	No
$CuTeO_3$	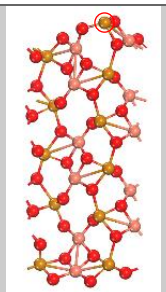	4.08	3.16	0.96	0.84	O_2↔OOH*	2.20	OH*↔O*	ORR
	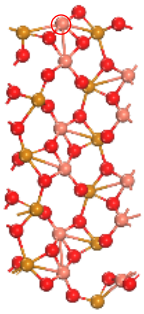	3.01	0.76	-0.39	-0.39	OH*↔H_2O	2.25	O*↔OOH*	No
	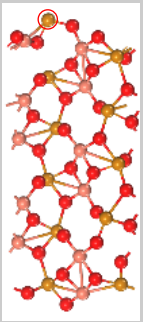	3.63	0.86	-1.09	-1.09	OH*↔H_2O	2.77	O*↔OOH*	No
Bi_4I	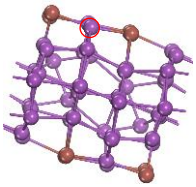	3.84	1.19	0.66	0.53	O*↔OH*	2.65	O*↔OOH*	No
	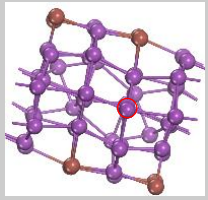	3.57	1.11	0.52	0.52	OH*↔H_2O	2.46	O*↔OOH*	No

$PtPb_4$		3.29	0.55	-0.29	-0.29	OH*↔H_2O	2.74	O*↔OOH*	No
		3.59	1.53	0.38	0.38	OH*↔H_2O	2.06	O*↔OOH*	No
		3.27	0.65	0.07	0.07	OH*↔H_2O	2.62	O*↔OOH*	No
$AgHO_2$	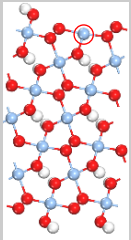	3.87	3.67	1.00	0.21	OOH*↔O*	2.67	OH*↔O*	No
$CuSeO_3$	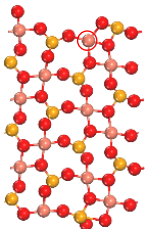	3.83	3.77	1.18	0.05	OOH*↔O*	2.59	OH*↔O*	No
	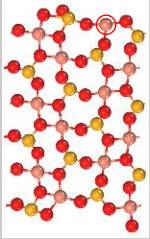	3.93	3.17	0.89	0.76	OOH*↔O*	2.28	OH*↔O*	ORR

$TaTe_2$	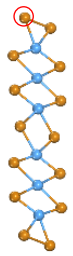	3.72	1.01	0.29	0.29	OH*↔H_2O	2.71	O*↔OOH*	No
	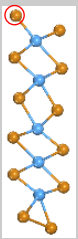	3.53	0.67	0.27	0.27	OH*↔H_2O	2.85	O*↔OOH*	No
	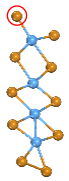	3.68	0.27	0.41	-0.13	O*↔OH*	3.41	O*↔OOH*	No
	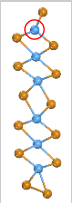	3.21	0.05	-0.22	-0.22	OH*↔H_2O	3.17	O*↔OOH*	No
	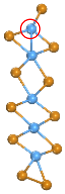	2.82	0.16	-0.39	-0.39	OH*↔H_2O	2.66	O*↔OOH*	No
	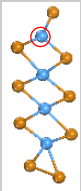	2.81	-0.29	-0.65	-0.65	OH*↔H_2O	3.10	O*↔OOH*	No

Table S7. Summary of dissolution sites, dissolution processes, standard reduction potentials (U^0, V *vs* SHE), and dissolution potentials (U_{diss}, V *vs* SHE) of 40 candidate materials screened out from activity analysis. U^0 values of different materials were obtained from ref. 24-26. For the materials whose dissolution process involves the protons, the function between the U_{diss} and pH was evaluated by Nernst equation. For example, U_{diss} on La_2PI_2 is calculated as $U_{diss}(\mathrm{pH}) = U_{diss}(\mathrm{pH} = 0) - 0.0591/10 * \log 1/[H^+]^{12} = U_{diss}(\mathrm{pH} = 0) - 0.0709\, pH$ according to the dissolution process of $I_2 + 6H_2O \rightarrow 2IO_3^- + 12H^+ + 10\, e^-$. More explanations can be in the website: https://www.doitpoms.ac.uk/tlplib/pourbaix/printall.php.

Formula	Dissolution site	Dissolution Process	U^0	U_{diss} at pH = 0 without concentration correction	U_{diss} at pH = 0 with correction	Is the dissolution pH-dependent?	U_{diss} at different pH level
$VAg(PSe_3)_2$	P	$P + 2H_2O \rightarrow H_3PO_2 + H^+ + e^-$	-0.51	-0.47	-0.72	Yes	-0.72 – 0.0591 pH
$MnSbSe_2I$	Sb	$2Sb + 3H_2O \rightarrow Sb_2O_3 + 6H^+ + 6e^-$	0.15	-0.19	-0.24	Yes	-0.24 – 0.0591 pH
$CuSeO_3$	Cu	$Cu \rightarrow Cu^{2+} + 2e^-$	0.34	0.10	-0.01	No	0.10
Bi_4I	Bi	$Bi \rightarrow Bi^{3+} + 3e^-$	0.31	0.43	0.32	No	0.43
$CuTeO_3$	Cu	$Cu \rightarrow Cu2^+ + 2e^-$	0.34	0.47	0.33	No	0.47
Bi_9I_2	Bi	$Bi \rightarrow Bi^{3+} + 3e^-$	0.31	0.61	0.50	No	0.61
$NiTe_2$	Te	$Te \rightarrow Te^{4+} + 4e^-$	0.57	0.76	0.67	No	0.76
$LiNi(PS_3)_2$	S	$S + 3H_2O \rightarrow H_2SO_3 + 4H^+ + 4e^-$	0.45	0.63	0.55	Yes	0.55 – 0.0591 pH
$Ta_3Te_{14}Pd_3$	Te	$Te \rightarrow Te^{4+} + 4e^-$	0.57	0.82	0.73	No	0.73
PtTe	Te	$Te \rightarrow Te^{4+} + 4e^-$	0.57	0.92	0.83	No	0.83
$Ge_5(Te_4As)_2$	Te	$Te \rightarrow Te^{4+} + 4e^-$	0.57	0.84	0.75	No	0.75
$MoTe_2$	Te	$Te \rightarrow Te^{4+} + 4e^-$	0.57	0.99	0.90	No	0.90
$Ge_4Te_7As_2$	Te	$Te \rightarrow Te^{4+} + 4e^-$	0.57	0.84	0.75	No	0.75
NiTe	Te	$Te \rightarrow Te^{4+} + 4e^-$	0.57	1.13	1.04	No	1.04
BiTe	Te	$Te \rightarrow Te^{4+} + 4e^-$	0.57	0.97	0.87	No	0.87
$NbTe_2$	Te	$Te \rightarrow Te^{4+} + 4e^-$	0.57	1.05	0.95	No	0.95
$Mn(InSe_2)_2$	Se	$Se + 3H_2O \rightarrow H_2SeO_3 + 4H^+ + 4e^-$	0.74	1.04	0.96	Yes	0.96 – 0.0591 pH
Nb_4IrSe_{10}	Se	$Se + 3H_2O \rightarrow H_2SeO_3 + 4H^+ + 4e^-$	0.74	1.13	1.04	Yes	1.04 – 0.0591 pH
TaS_2	S	$S + 3H_2O \rightarrow H_2SO_3 + 4H^+ + 4e^-$	0.45	1.28	1.18	Yes	1.18 – 0.0591 pH
BiSe	Se	$Se + 3H_2O \rightarrow H_2SeO_3 + 4H^+ + 4e^-$	0.74	1.26	1.17	Yes	1.17 – 0.0591 pH

Fe_4S_5	S	$S + 3H_2O \rightarrow H_2SO_3 + 4H^+ + 4e^-$	0.45	1.34	1.26	Yes	1.26 – 0.0591 pH
$NbSe_2$	Se	$Se + 3H_2O \rightarrow H_2SeO_3 + 4H^+ + 4e^-$	0.74	1.50	1.40	Yes	1.40 – 0.0591 pH
$TaSe_2$	Se	$Se + 3H_2O \rightarrow H_2SeO_3 + 4H^+ + 4e^-$	0.74	1.50	1.40	Yes	1.40 – 0.0591 pH
ZrSiSe	Se	$Se + 3H_2O \rightarrow H_2SeO_3 + 4H^+ + 4e^-$	0.74	1.65	1.56	Yes	1.56 – 0.0591 pH
GdBr	\	\	\	\	\	\	\
$Sc_6C_2I_{11}$	Sc	$Sc \rightarrow Sc^{3+} + 3e^-$	-2.09	-0.90	-1.00	No	-1.00
$Li_2Cu_2F_5$	Cu	$Cu \rightarrow Cu^{2+} + 2e^-$	0.34	-0.01	-0.02	No	-0.02
$Pd_3Pb_2Te_2$	Pb	$Pb \rightarrow Pb^{3+} + 3e^-$	-0.13	0.45	0.29	No	0.29
$Zn(InS_2)_2$	S	$S + 3H_2O \rightarrow H_2SO_3 + 4H^+ + 4e^-$	0.45	0.69	0.60	Yes	0.60
$Ta(NiTe)_2$	Te	$Te \rightarrow Te^{4+} + 4e^-$	0.57	0.85	0.76	No	0.76
VTe_2	Te	$Te \rightarrow Te^{4+} + 4e^-$	0.57	0.98	0.89	No	0.89
Bi_3Se_4	Se	$Se + 3H_2O \rightarrow H_2SeO_3 + 4H^+ + 4e^-$	0.74	1.13	1.04	Yes	1.04 – 0.0591 pH
$TaTe_2$	Te	$Te \rightarrow Te^{4+} + 4e^-$	0.57	1.05	0.96	No	0.96
Nb_2Se_3	Se	$Se + 3H_2O \rightarrow H_2SeO_3 + 4H^+ + 4e^-$	0.74	1.54	1.45	Yes	1.45 – 0.0591 pH
Pr_2Br_5	\	\	\	\	\	\	\
CeZnPO	\	\	\	\	\	\	\
EuBrO	\	\	\	\	\	\	\
TbBr	\	\	\	\	\	\	\
$CrGeTe_3$	Ge	$Ge \rightarrow Ge^{2+} + 2e^-$	0.1	0.07	-0.10	No	-0.10
$PtPb_4$	Pb	$Pb \rightarrow Pb^{3+} + 3e^-$	-0.13	0.26	0.07	No	0.07
$CuH_2(SeO_3)_2$	Cu	$Cu \rightarrow Cu^{2+} + 2e^-$	0.34	0.53	0.41	No	0.41
$Ag(AuS)_2$	S	$S + 3H_2O \rightarrow H_2SO_3 + 4H^+ + 4e^-$	0.45	0.71	0.63	Yes	0.63 – 0.0591 pH
Nb_9IrSe_{20}	Se	$Se + 3H_2O \rightarrow H_2SeO_3 + 4H^+ + 4e^-$	0.74	1.25	1.15	Yes	1.15 – 0.0591 pH
$AgHO_2$	Ag	$Ag \rightarrow Ag^+ + e^-$	0.80	0.77	0.55	No	0.55
La_2PI_2	I	$I_2 + 6H_2O \rightarrow 2IO_3^- + 12H^+ + 10\ e^-$	1.20	1.80	1.72	Yes	1.72 – 0.0709 pH
TbGaI	\	\	\	\	\	\	\
CeI_3	\	\	\	\	\	\	\

Table S8 Calculated potential difference between U_{diss} and U_L ($U_{diss} - U_L$) as a function of pH, and the minimum pH requirement (pH_{mini}) of 14 ORR catalysts and 16 OER catalysts that excluded from the electrochemical stability analysis at pH = 0. For materials that the value of $U_{diss} - U_L$ remains constant at full pH level, the pH_{mini} is marked as "none". Unstable materials at full pH range were highlighted by red color.

Category	Formula	$U_{diss} - U_L$ as function of pH	pH_{mini}
ORR catalysts	$LiNi(PS_3)_2$	-0.06 + 0.0591 pH	2
	$VAg(PSe_3)_2$	-1.32	none
	$Ta_3Te_{14}Pd_3$	-0.02	none
	$MnSbSe_2I$	-0.86	none
	$CrGeTe_3$	-0.93 + 0.0591 pH	>14
	$CuSeO_3$	-0.81 + 0.0591 pH	14
	$AgHO_2$	-0.61 + 0.0591 pH	11
	$PtPb_4$	-0.57 + 0.0591 pH	10
	Bi_4I	-0.50 + 0.0591 pH	9
	$CuTeO_3$	-0.42 + 0.0591 pH	8
	$CuH_2(SeO_3)_2$	-0.31 + 0.0591 pH	6
	$Ag(AuS)_2$	-0.13	none
	Bi_9I_2	-0.12 + 0.0591 pH	3
	$NiTe_2$	-0.09	none
OER catalysts	$Sc_6C_2I_{11}$	-2.91 + 0.0591 pH	>14
	$Li_2Cu_2F_5$	-1.75 + 0.0591 pH	>14
	$CrGeTe_3$	-1.75 + 0.0591 pH	>14
	$PtPb_4$	-1.75 + 0.0591 pH	>14
	$Pd_3Pb_2Te_2$	-1.28 + 0.0591 pH	>14
	$CuH_2(SeO_3)_2$	-1.36 + 0.0591 pH	>14
	$Zn(InS_2)_2$	-1.26	none
	$Ag(AuS)_2$	-1.20	none
	$Ta(NiTe)_2$	-1.15 + 0.0591 pH	>14
	VTe_2	-1.03 + 0.0591 pH	>14
	Bi_3Se_4	-0.87	none
	$TaTe_2$	-0.83 + 0.0591 pH	14
	Nb_9IrSe_{20}	-0.76	none
	$AgHO_2$	-0.77 + 0.0591 pH	13
	Nb_2Se_3	-0.43	none
	La_2PI_2	-0.19 – 0.1182 pH	none

Table S9 Summary of theoretical and experimental progresses on the design of 2D materials for the oxygen electrocatalysis.

	Material	Overpotential	Active site	Theory or Exp?	Stability of the original structure	Reference
ORR catalysts	Pd_3Pb	330 mV in 0.1 M KOH	Pt sites	Theory & Exp.	Activity remains 77% after 5000 cycles	Small Methods 2018, 1700331
	MX_2 (M= V, Nb, Mo, Ta, and W; X= S, Se and Te)	>=950 mV in aprotic media	Edge sites of VSe_2	Theory & Exp.	N/A	Adv. Mater. 2019, 31, 1804453
	CoS_2	580 mV	Co metal site within the Co oxide surface	Theory & Exp.	Unstable	ACS Appl. Energy Mater. 2019, 2, 8605−8614
	SnS, and SnS_2	>1000 mV on SnS2 in 50 mM phosphate buffered saline	N/A	Exp.	Unstable	J. Phys. Chem. C 2016, 120, 24098−24111
	InS, InSe and InTe	>1000 mV in 1.0 M KOH solution	N/A	Exp.	Unstable	ChemCatChem 2019, 11, 2634 – 2642
	$FeNiS_2$	450 mV in 0.1 M phosphate buffer solution	N/A	Exp.	Stable	Nano Energy 27 (2016) 526–534
	Ni_3S_2/MoS_2 heterostructure	280 mV in 0.1 M KOH electrolyte	Mo edges/Mo–Ni–S sites in the heterointerfaces	Exp.	2.7 h test with activity loss of 12.0%	J. Mater. Chem. A, 2019, 7, 8785–8789
	Nb/Ta doped MoS_2 and WS_2	>=450 mV on undoped MoS2 in 0.1 M KOH solution	N/A	Exp.	N/A	ACS Catal. 2016, 6, 5724−5734
	P doped MoS_2	270 mV	N/A	Exp.	Over 2.7 h with activity loss of 18.8%	Chem. Commun., 2015, 51, 7903--7906
	MX_2 (M = Nb, Ta, Mo, W; X = S, Se, Te)	540 mV	S/Te sites in the basal plane of $NbS_2/TaSe_2$	Theory	N/A	Nano Research volume 12, pages 925–930 (2019)
	$_1T'$-$TaTe_2$	510 mV	Te sites in the basal plane	Theory	1, 2	Green Energy & Environment, https://doi.org/10.1016/j.gee.2020.11.003
	PtTe	370 mV	Te sites in the basal plane	Theory	1, 2	J. Am. Chem. Soc. 2018, 140, 12732−12735

	NiTe	450 mV	Te sites in the basal plane	Theory	1, 2, 4	J. Phys. Chem. C 2021, 125, 19164−19170
	M_2S_2 (M= Sc, Ti, V, Cr, Mn, Co, Ni, Zr, Nb, Mo, Ru, Rh, Pd, Hf, Ta, W, and Ir)	>=380 mV	S sites in the basal plane of Ti_2S_2	Theory	N/A	Energy Fuels 2020, 34, 5006−5015
	206 MS_2 contain $_2$H, $_1$T, and $_1$T′ phase	>=240 mV	Te sites in the basal plane of VTe_2	Theory	1, 2, 3	J. Phys. Chem. Lett. 2022, 13, 58−65
	Pt_5Se_4	700 mV	Pt sites in the basal plane	Theory	1, 2, 4	ACS Appl. Mater. Interfaces 2020, 12, 12, 13896–13903
	RuN_2	240 mV	Ru sites the basal plane	Theory	1, 2, 3	ACS Appl. Mater. Interfaces 2020, 12, 49, 54517–54523
	IrN_2	470 mV	Ir sites in the basal plane	Theory	1,2,3	Journal of Colloid and Interface Science (2021), doi: https://doi.org/10.1016/j.jcis.2021.05.028
	$MN_4C_{12}H_4$ (M=Cr, Mn, Fe, Co, Ni, Cu, Ru, Rh, Ir, Pt, Pd, and Ag)	>=330 mV	Fe sites in the basal plane of $FeN_4C_{12}H_4$	Theory	1,3	Journal of Catalysis 370 (2019) 378–384
	$M_2C_{12}N_{12}H_{12}$ (M= V, Cr, Mn, Fe, Co, Ni, Cu, Ru, Rh, Pd)	>=520 mV	Fe sites in the basal plane of $Fe_2C_{12}N_{12}H_{12}$	Theory	N/A	Journal of Catalysis 352 (2017) 579–585
	MC_2 (M= Ti, V, Nb, Ta, and Mo)	>=370mV	C sites in the basal plane of TaC_2	Theory	1, 2	Adv. Funct. Mater. 2020, 30, 2000570
	GeS, GeSe, and SnSe	>=520 mV	Ge sites in the basal plane of GeS	Theory	1, 3	J. Mater. Chem. A, 2017, 5, 1734–1741
	Nb_2SbTe_2	330 mV	Te sites in the basal plane	Theory	1, 2	Inorg. Chem. 2022, 61, 4, 2284–2291
	Ni_2SbTe_2, NiSb, $NiTe_2$, $NiSe_2$, Co_2SbTe, and Ni_2SbSe_2	>=710 mV	(014) surface of Ni_2SbTe_2	Theory	1, 2	J. Phys. Chem. C 2020, 124, 3671−3680
	MA_2Z_4 (M = Ti, Zr, Hf, V, Nb, Ta, Cr, Mo, W; A = Si or Ge; Z = N,	>=490 mV	As sites in the basal plane of $CrGe_2As_4$	Theory	1, 2	J. Phys. Chem. C 2021, 125, 22581−22590

	P, or As)					
	N-/P-doped TMD (MoS_2, $MoSe_2$, WS_2, and WSe_2)	>=310 mV	N sites in the N-doped WS_2 monolayer	Theory	1	ChemElectroChem 2018, 5, 4029 –4035
	Pt doped $MoSe_2$	480 mV	Se sites in the basal plane	Theory	N/A	J. Mater. Chem. C, 2021, 9, 11331–11342
OER catalysts	$Fe_2S_6C_6$	372 mV at 20°C in 1.0 M N_2-saturated KOH electrolyte	Fe, and S sites in the basal plane	Theory & Exp.	50 h with activity loss of 6 mV.	ACS Energy Lett. 2022, 7, 343−348
	$PtSe_2$	663 mV	Defective sites in the basal plane	Theory & Exp.	Over 10 h in 1 M KOH	Adv. Energy Mater. 2022, 12, 2102359
	MoS_2, and TaS_2 with $_1T$ and $_2H$ phases	420 mV in 0.5 M H2SO4	Edge sites of the 1T-MoS_2	Theory & Exp.	Stable	Adv. Mater. Interfaces 2016, 3, 1500669
	MX_2 (M= V, Nb, Mo, Ta, and W; X= S, Se and Te)	>=800mV in aprotic media	Edge sites of VSe_2	Theory & Exp.	N/A	Adv. Mater. 2019, 31, 1804453
	$NiPS_3/Ni_2P$ heterostructure	260 mV in 1.0 M KOH	In-situ formed nickel hydroxides and/or oxyhydroxides	Theory & Exp.	Unstable	ACS Nano 2019, 13, 7, 7975–7984
	Ni_3S_2 nanosheet arrays on nickel foam	260 mV in basic media	In situ grown $(\bar{2}10)$ high-index facet	Theory & Exp.	Retains the activity for over 200 h	J. Am. Chem. Soc. 2015, 137, 44, 14023–14026
	$CoSe_2$	294.2 mV in 1 M NaOH	Co vacancies in in-situ formed metal hydroxides	Theory & Exp.	Unstable	Nat Commun 11, 1664 (2020).
	$PtTe_2$	368 mV	Newly formed Pt sites	Exp.	Unstable	Nanotechnology, 2020, 31 375601
	Co doped MoS_2	220 mV	Newly formed high valence state Co species	Exp.	Unstable	Adv. Mater. 2018, 30(29), 1801450
	Fe doped CoS_2	302 mV	N/A	Exp.	Maintains the catalytic activity for at least 20 h	Chem. Commun., 2019,55, 2469-2472
	$FeNiS_2$	310 mV in 0.1 M KOH solution	Newly formed NiOOH species	Exp.	Unstable	Nano Energy 27 (2016) 526–534
	$FePS_3$	288 mV in 0.1 M KOH	Newly formed	Exp.	Unstable	Small Methods 2019, 1900632

		solution	FeOOH species			
	WS_2/CNT heterostructure	430 mV in 0.1 M KOH solution	W-bonded C atoms at the WS_2–CNT interface	Exp.	Stable	Adv. Energy Mater. 2017, 7, 1602217
	GeS, and GeSe	>=970mV	N/A	Exp.	Unstable	Phys. Chem. Chem. Phys., 2016, 18, 1699--1711
	SnS, and SnS_2	>1000mV in 50 mM phosphate buffered saline	N/A	Exp.	Unstable	J. Phys. Chem. C 2016, 120, 24098−24111
	InS, InSe and InTe	>1000mV in 1.0 M KOH solution	N/A	Exp.	Unstable	ChemCatChem 2019, 11, 2634 – 2642
	Pt_5Se_4	350 mV	Pt sites in the basal plane	Theory	1, 2, 4	ACS Appl. Mater. Interfaces 2020, 12, 12, 13896–13903
	MN_2 (M= V, Co, W, Re, Rh, Pd, Ir)	>=270 mV	Ir sites in the basal plane of IrN_2	Theory	1,2,3	Journal of Colloid and Interface Science (2021), doi: https://doi.org/10.1016/j.jcis.2021.05.028
	[206] MS_2 contain $_2$H, $_1$T, and $_1$T′ phase	>=300 mV	Te sites in the basal plane of $TaTe_2$	Theory	1, 2, 3	J. Phys. Chem. Lett. 2022, 13, 58−65
	$MN_4C_{12}H_4$ (M=Cr, Mn, Fe, Co, Ni, Cu, Ru, Rh, Ir, Pt, Pd, and Ag)	>=460 mV	Ni sites in the basal plane of $NiN_4C_{12}H_4$	Theory	1,3	Journal of Catalysis 370 (2019) 378–384
	$MC_6N_6H_6$ (M= V, Cr, Mn, Fe, Co, Ni, Cu, Ru, Rh, Pd)	>=320 mV	Rh sites in the basal plane of $RhN_6C_6H_6$	Theory	N/A	Journal of Catalysis 352 (2017) 579–585
	MC_2 (M= Ti, V, Nb, Ta, and Mo)	>=450mV	C sites in the basal plane of MoC_2	Theory	1, 2	Adv. Funct. Mater. 2020, 30, 2000570
	Metal atom doped Ga_2FeS_4	>=480 mV	Au atom doped Ga_2FeS_4	Theory	1	J. Mater. Chem. A, 2021, 9, 18594–18603

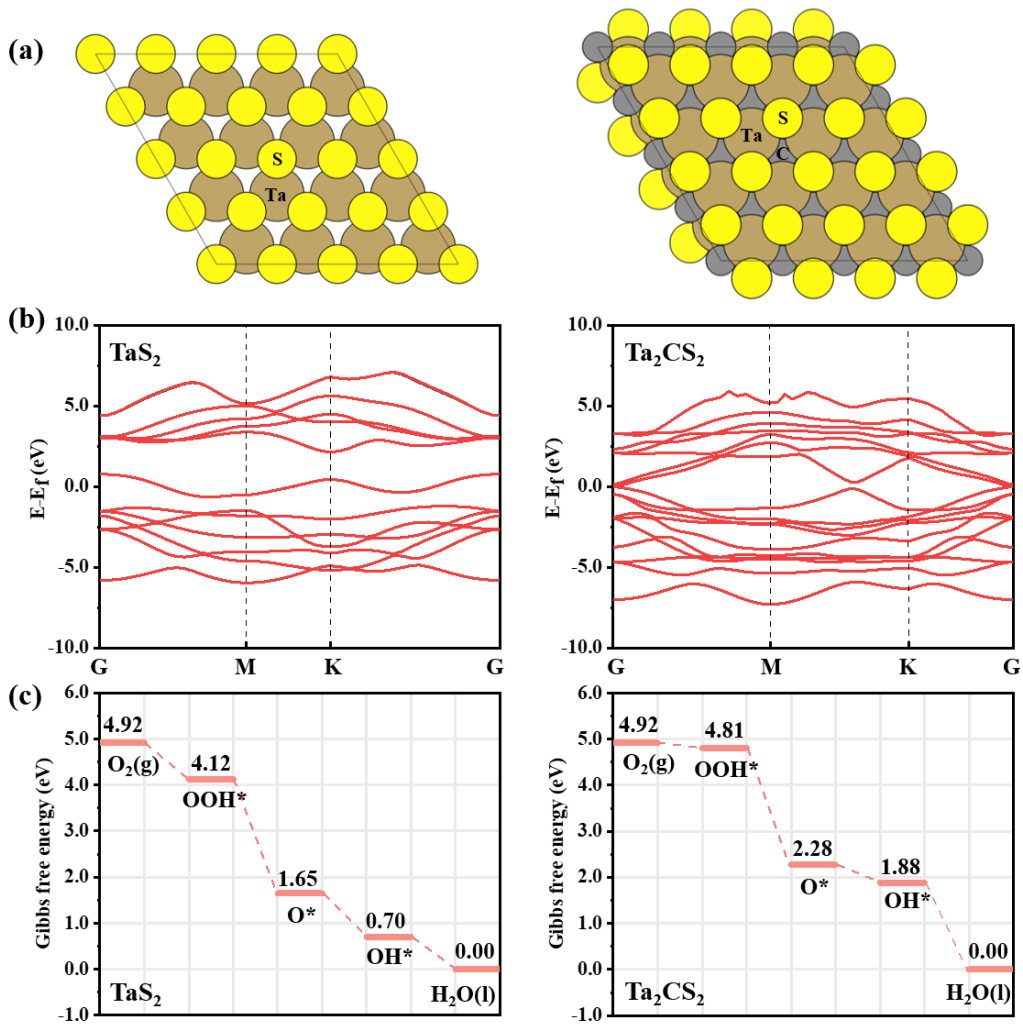

Fig. S1. Top view of structure (a), band structure (b), and reaction pathway along the oxygen reduction reaction for the TaS_2 and Ta_2CS_2.

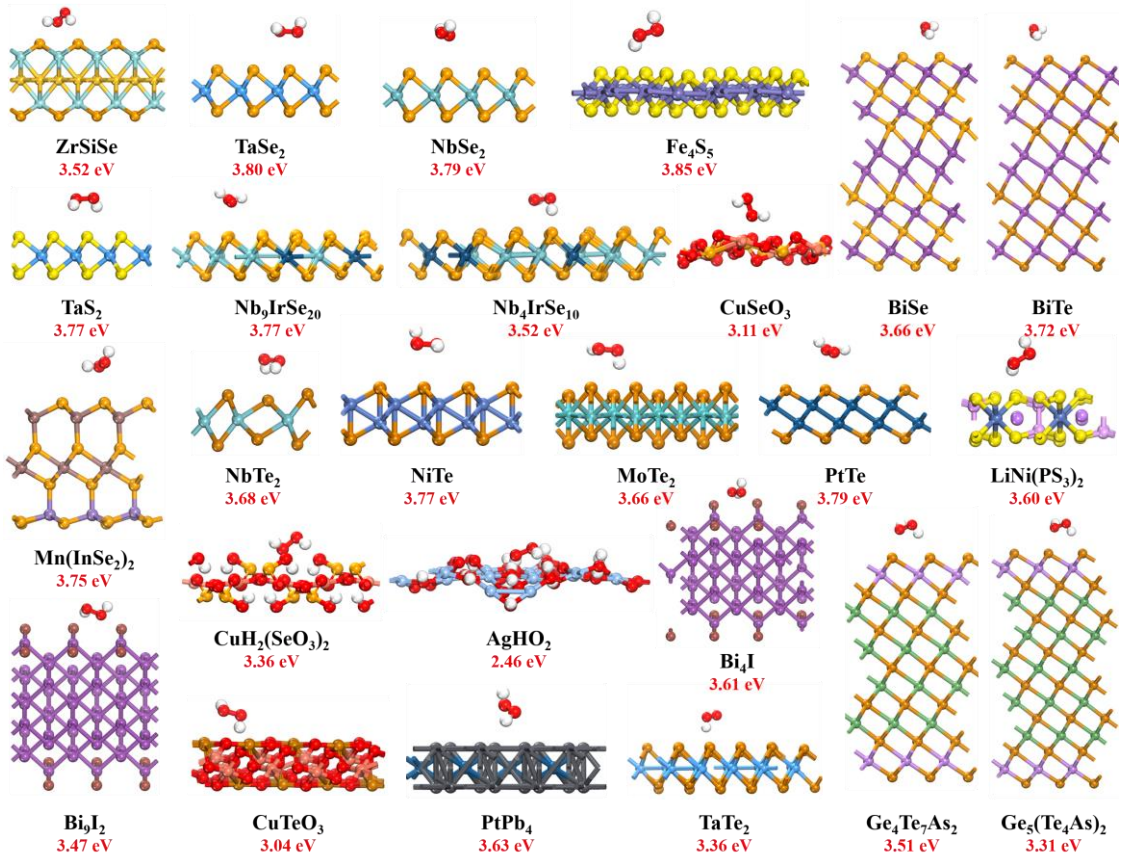

Fig. S2. Side view of adsorption configuration and the corresponding adsorption free energy of H_2O_2 (use the H_2O and H_2 as the energy references) at the active site of 25 2D materials that is predicted for the four-electron oxygen electrocatalysis.

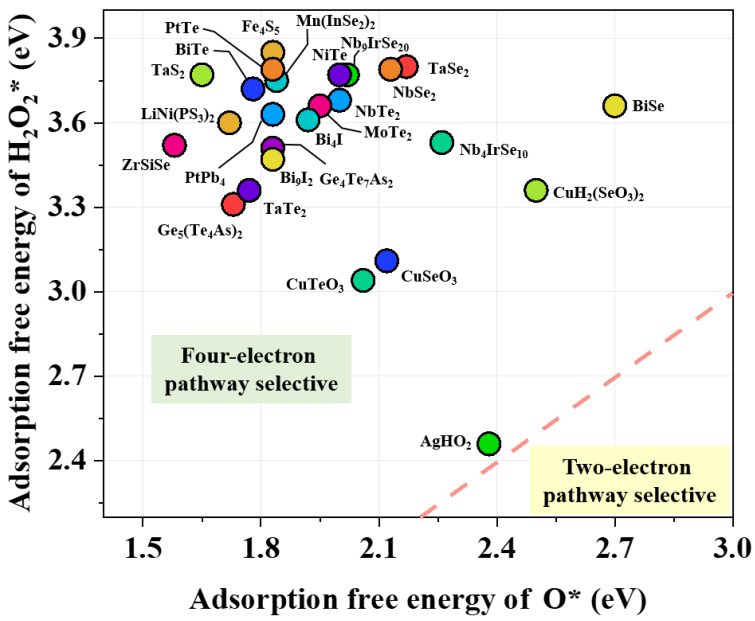

Fig. S3. Adsorption analysis for the O* and H_2O_2* on 25 four-electron pathway preferable materials that were identified using the free energy of O* as the descriptor.

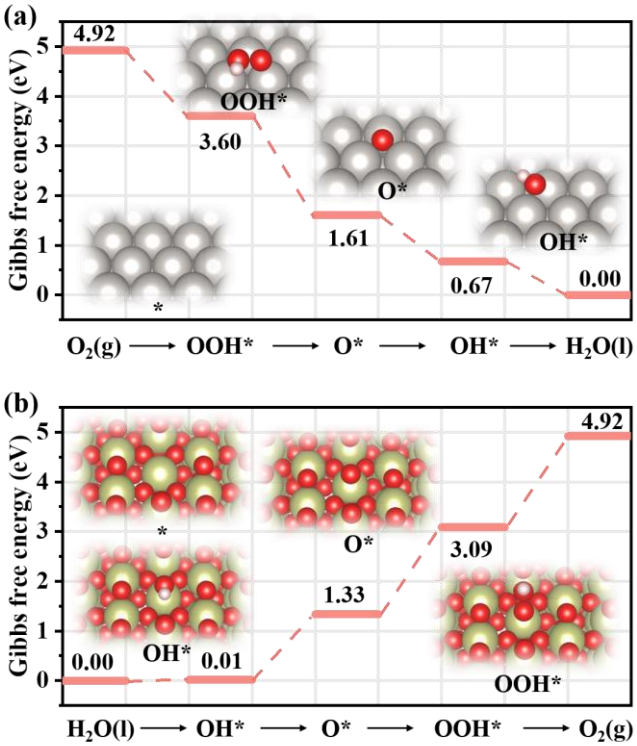

Fig. S4. Computed free energy profile of ORR on the Pt(111) (a), and of OER on the IrO_2(110) (b). The solvation contribution of -0.3, 0.0, -0.3 eV were included in the free energy computations for the OOH*, O*, OH*, respectively, to ensure all the computations are under the same computation level, and to be comparable as the activity benchmark. Note that the corrected adsorption free energies are of well agreement with the previous work. [28] For example, the computed free energy value of 3.088 eV for OOH* adsorption on the IrO_2 (110) is very close to the reported value of 3.1 eV. No clear solvation correction was found for the O* adsorption, which also agrees well with our correction strategy. The slight difference might be raised by the dipole effect on the polar surfaces of IrO_2 (110) due to the inclusion of explicit water molecules in their study. [29]

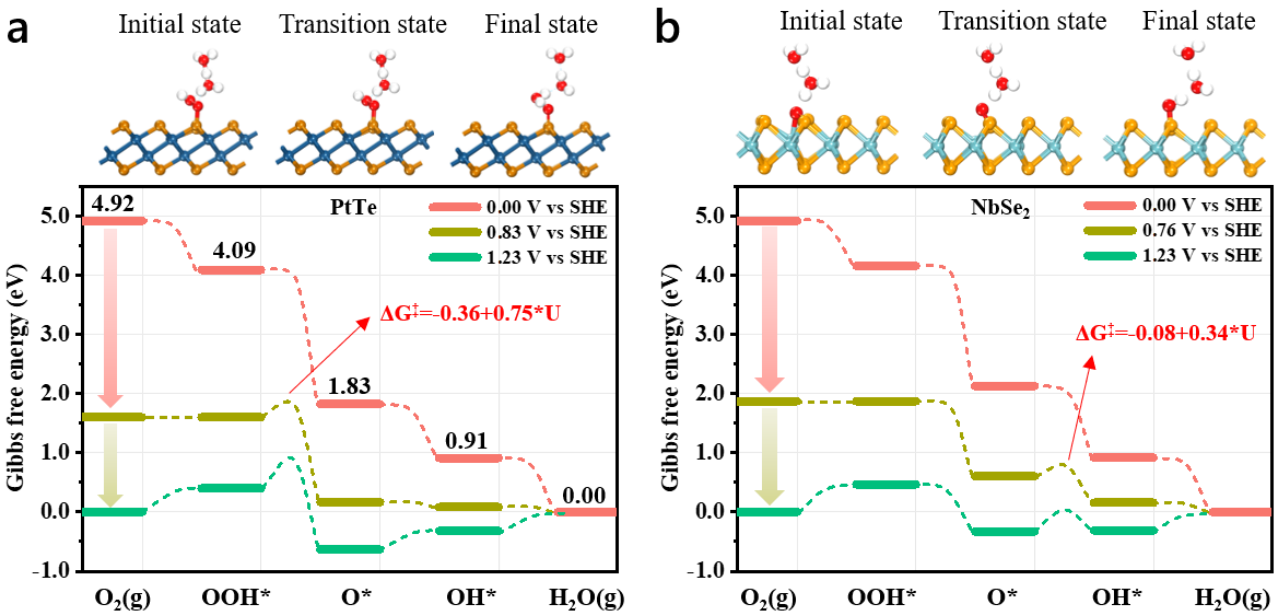

Fig. S5. Kinetic simulation of ORR on the PtTe and $NbSe_2$ surfaces at three different potential (zero potential, theoretical limiting potential, and equilibrium potential). The key reaction intermediates along the rate limiting step obtained from the climbing image nudged elastic band (CI-NEB) method are also shown.

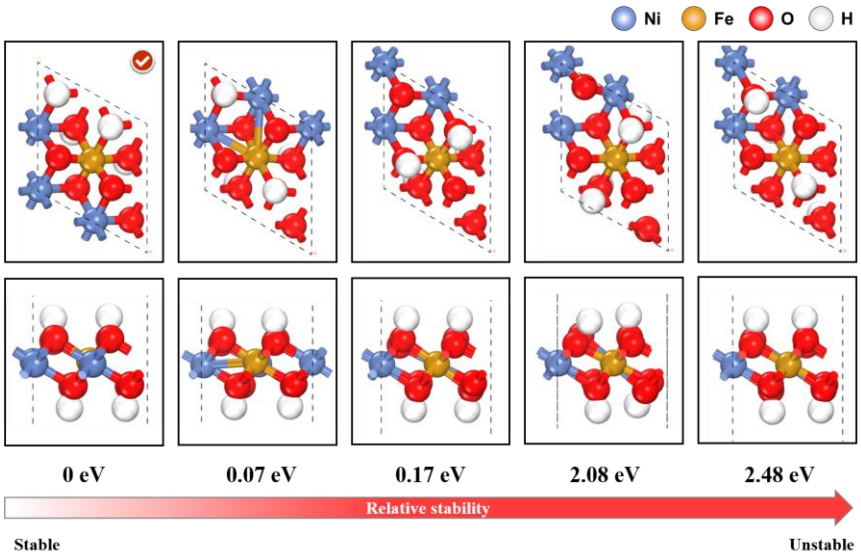

Fig. S6. Relative stability analysis on the possible configuration of $Ni_{0.75}Fe_{0.25}OOH$.

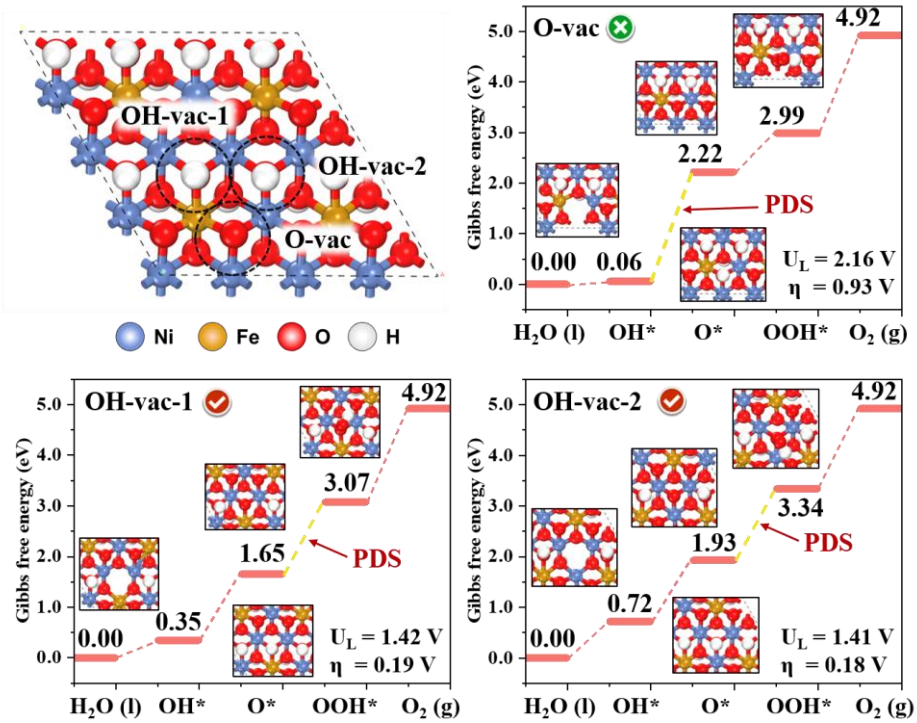

Fig. S7. Free energy diagrams for the OER on three different sites of $Ni_{0.75}Fe_{0.25}OOH$, including OH and O vacancies. The potential limiting step (PDS) was highlighted by yellow line. Note that the self-interaction error in GGA method could strongly affect the adsorption on the transitional oxides, as conventional DFT is not canceled out in redox reactions where the electrons are transferred between significantly different environments. To address this issue, DFT+U computations was carried out, where the U values for the Ni and Fe were set as 6.2 and 5.3 eV, respectively, following the strategy in the Materials Project database.

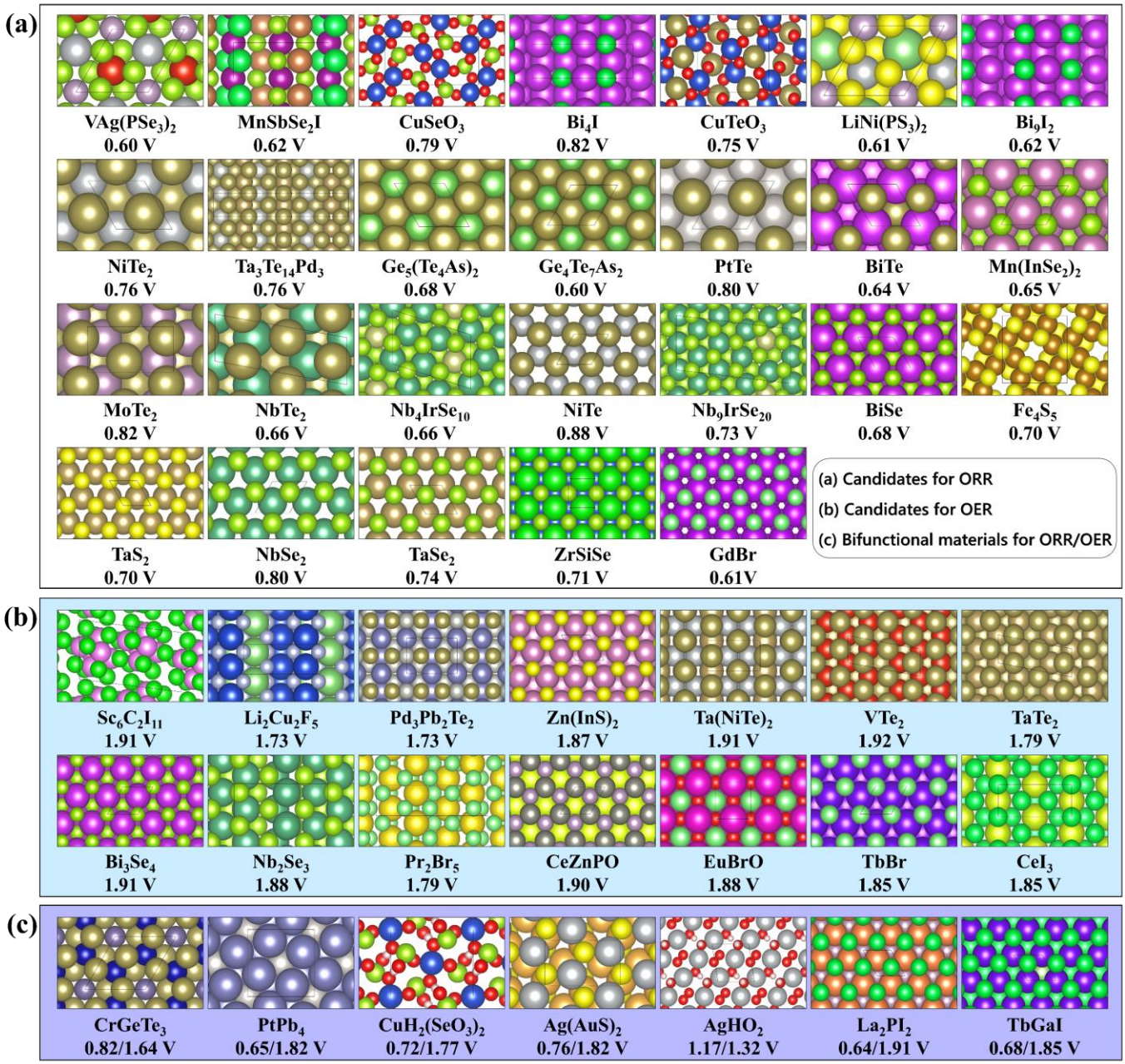

Fig. S8. (a) 25 basal plane active materials for the oxygen reduction reaction. (b) 13 candidates for the oxygen evolution reaction. (c) nine compounds with bifunctional capability for both oxygen reduction and oxygen evolution reactions.

	$VAg(PSe_3)_2$	OOH*	O*	OH*
Top view	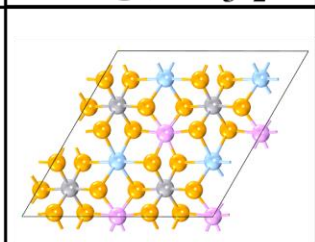	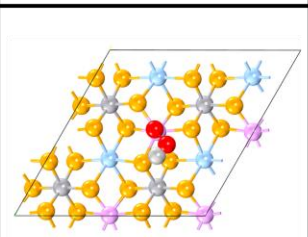	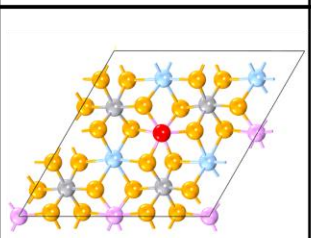	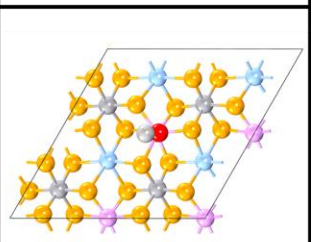
Side view	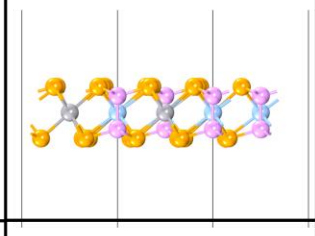	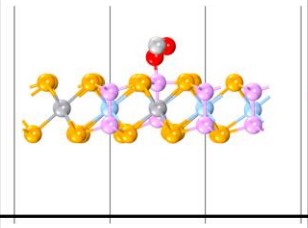	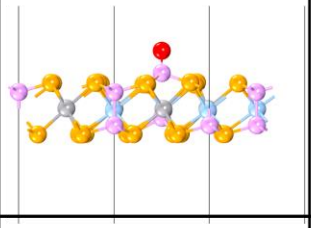	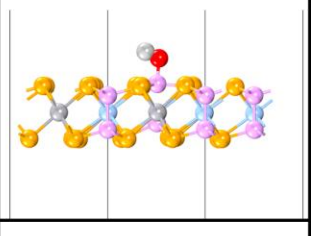
ΔZPE	\	0.45	0.08	0.37
ΔH	\	0.08	0.03	0.05
ΔTS	\	0.16	0.06	0.08
ΔG	\	3.92	1.34	0.60
PDS	$OH^* \rightarrow H_2O$		**U_L(ORR)**	0.60

Fig. S9. Optimized structures and computed thermodynamic data (include zero-point energy (ΔZPE), enthalpy (ΔH), entropy (ΔTS), and Gibbs free energy (ΔG)) of oxygen-containing species on the **$VAg(PSe_3)_2$** surface. The corresponding U_L value for **ORR** is also shown.

	$MnSbSe_2I$	OOH*	O*	OH*
Top view	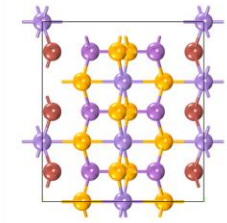	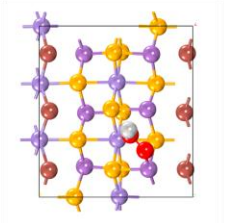	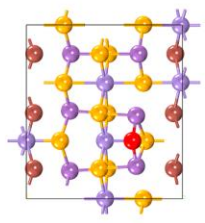	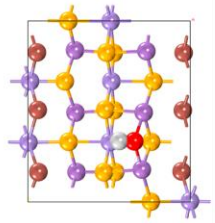
Side view	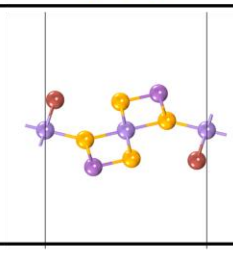		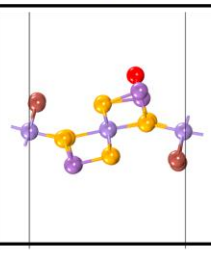	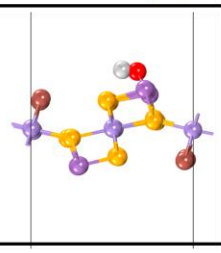
ΔZPE	\	0.43	0.07	0.35
ΔH	\	0.09	0.03	0.05
ΔTS	\	0.18	0.05	0.08
ΔG	\	4.06	1.25	0.63
PDS	O* → OH*		**U_L(ORR)**	0.62

Fig. S10. Optimized structures and computed thermodynamic data (include ΔZPE, ΔH, ΔTS, and ΔG) of oxygen-containing species on the **$MnSbSe_2I$** surface. The corresponding U_L value for **ORR** is also shown.

	$CuSeO_3$	OOH*	O*	OH*
Top view	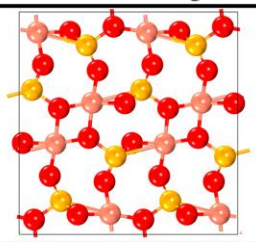	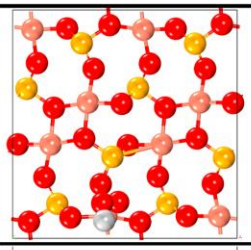	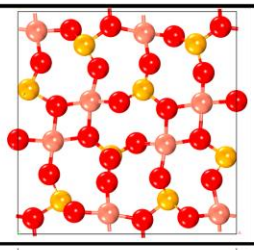	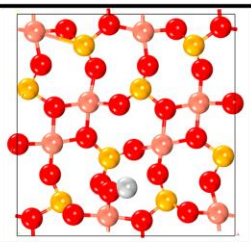
Side view	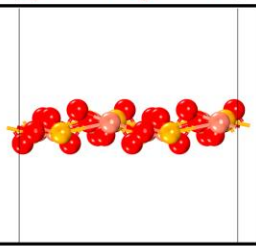	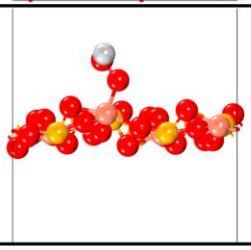	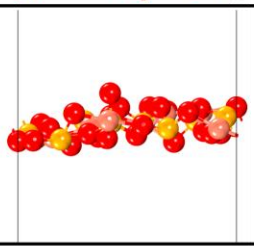	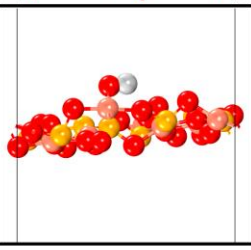
ΔZPE	\	0.42	0.08	0.36
ΔH	\	0.11	0.03	0.05
ΔTS	\	0.24	0.05	0.09
ΔG	\	4.13	2.12	1.13
PDS	$O_2 \rightarrow$ OOH*		**U_L(ORR)**	0.79

Fig. S11. Optimized structures and computed thermodynamic data (include ΔZPE, ΔH, ΔTS, and ΔG) of oxygen-containing species on the **$CuSeO_3$** surface. The corresponding U_L value for **ORR** is also shown.

	Bi_4I	OOH*	O*	OH*
Top view	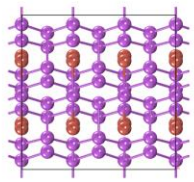	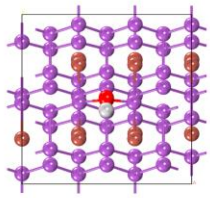	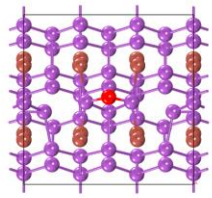	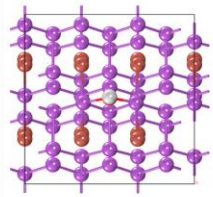
Side view	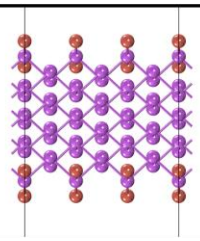	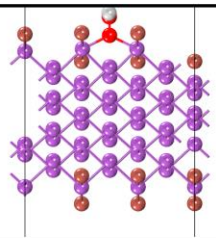	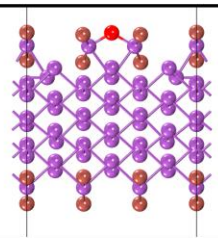	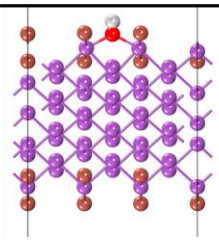
ΔZPE	\	0.42	0.06	0.32
ΔH	\	0.10	0.03	0.06
ΔTS	\	0.21	0.06	0.12
ΔG	\	3.95	1.92	0.82
PDS	$OH^* \rightarrow H_2O$		U_L(ORR)	0.82

Fig. S12. Optimized structures and computed thermodynamic data (include ΔZPE, ΔH, ΔTS, and ΔG) of oxygen-containing species on the **Bi_4I** surface. The corresponding U_L value for **ORR** is also shown.

	$CuTeO_3$	OOH*	O*	OH*
Top view	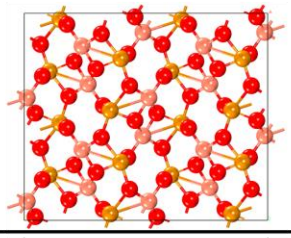	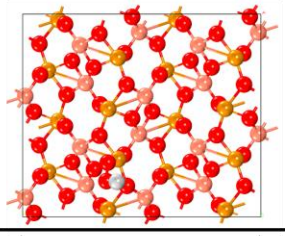	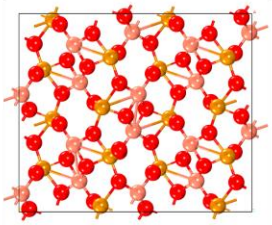	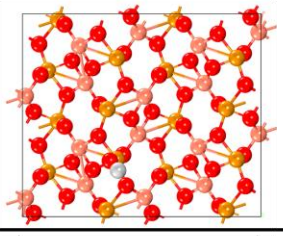
Side view	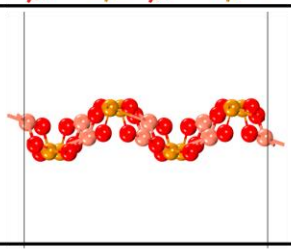	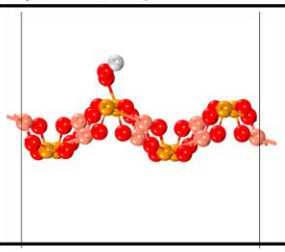	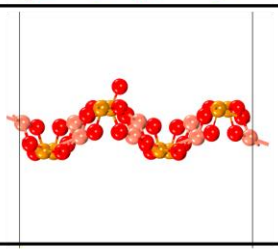	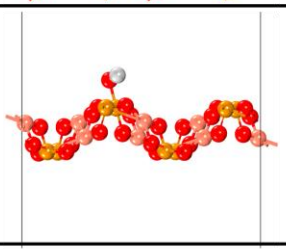
ΔZPE	\	0.42	0.07	0.34
ΔH	\	0.10	0.04	0.06
ΔTS	\	0.21	0.07	0.11
ΔG	\	4.17	2.06	0.94
PDS	O* → OH*		**U_L(ORR)**	0.75

Fig. S13. Optimized structures and computed thermodynamic data (include ΔZPE, ΔH, ΔTS, and ΔG) of oxygen-containing species on the **$CuTeO_3$** surface. The corresponding U_L value for **ORR** is also shown.

	Bi_9I_2	OOH*	O*	OH*
Top view	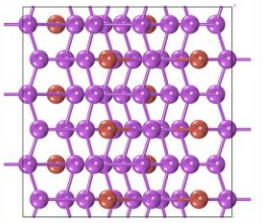	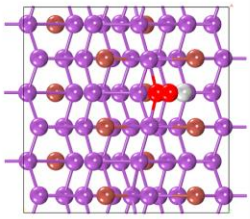	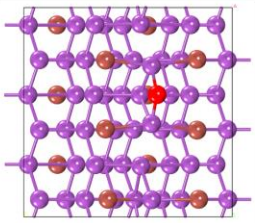	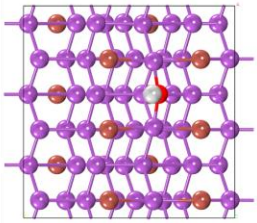
Side view	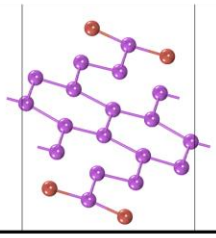	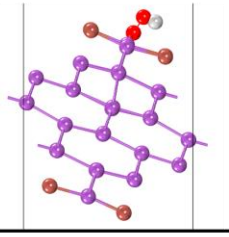	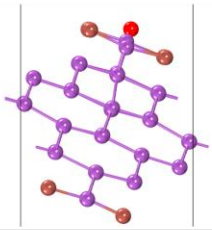	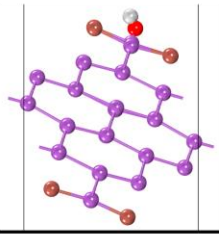
ΔZPE	\	0.42	0.06	0.32
ΔH	\	0.08	0.03	0.07
ΔTS	\	0.14	0.06	0.13
ΔG	\	3.79	1.83	0.62
PDS	$OH^* \rightarrow H_2O$		U_L(ORR)	0.62

Fig. S14. Optimized structures and computed thermodynamic data (include ΔZPE, ΔH, ΔTS, and ΔG) of oxygen-containing species on the **Bi_9I_2** surface. The corresponding U_L value for **ORR** is also shown.

	$NiTe_2$	OOH*	O*	OH*
Top view	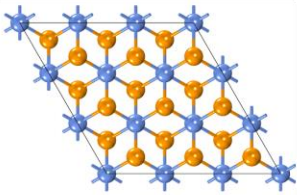	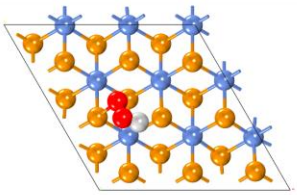	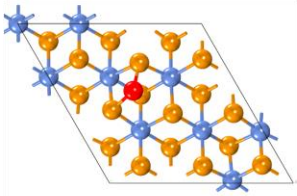	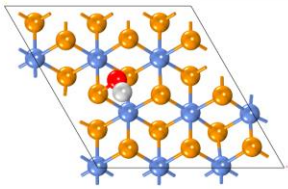
Side view	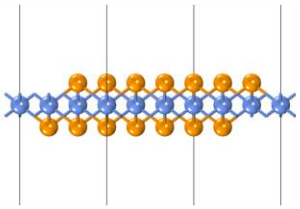	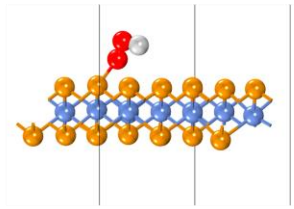	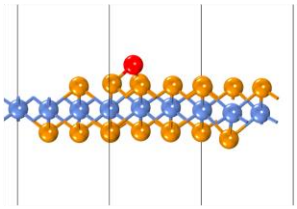	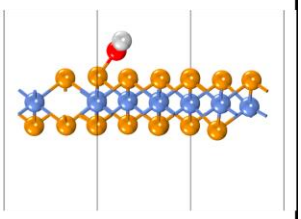
ΔZPE	\	0.42	0.06	0.33
ΔH	\	0.10	0.03	0.06
ΔTS	\	0.21	0.06	0.12
ΔG	\	4.01	1.60	0.76
PDS	$OH^* \rightarrow H_2O$		U_L(ORR)	0.76

Fig. S15. Optimized structures and computed thermodynamic data (include ΔZPE, ΔH, ΔTS, and ΔG) of oxygen-containing species on the **$NiTe_2$** surface. The corresponding U_L value for **ORR** is also shown.

	$LiNi(PS_3)_2$	OOH*	O*	OH*
Top view	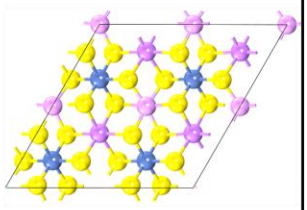	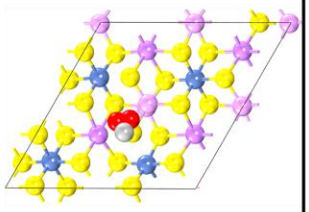	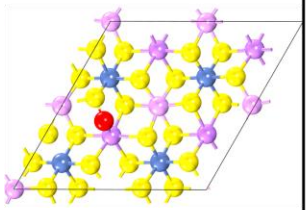	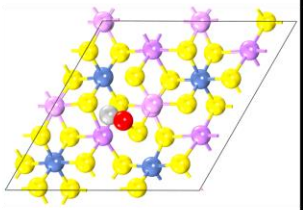
Side view	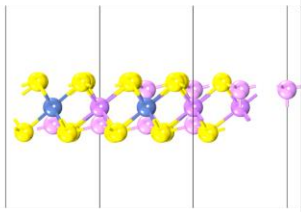	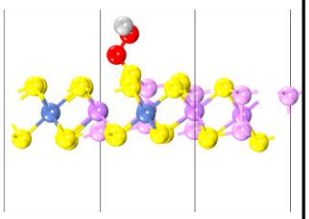	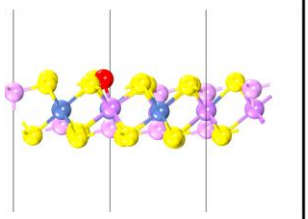	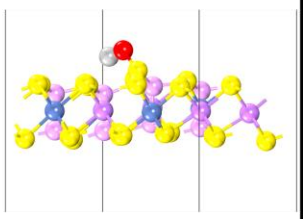
ΔZPE	\	0.43	0.08	0.37
ΔH	\	0.09	0.03	0.04
ΔTS	\	0.18	0.05	0.08
ΔG	\	4.31	1.72	0.99
PDS	$O_2 \rightarrow$ OOH*		U_L(ORR)	0.61

Fig. S16. Optimized structures and computed thermodynamic data (include ΔZPE, ΔH, ΔTS, and ΔG) of oxygen-containing species on the **$LiNi(PS_3)_2$** surface. The corresponding U_L value for **ORR** is also shown.

	$Ta_3Te_{14}Pd_3$	OOH*	O*	OH*
Top view	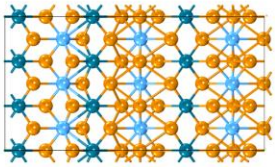	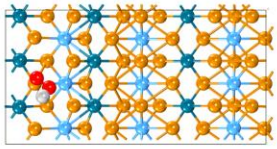	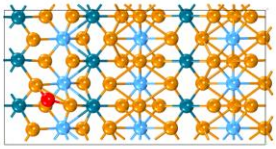	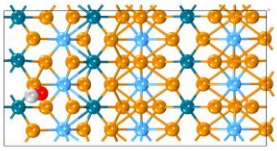
Side view	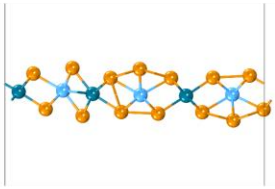	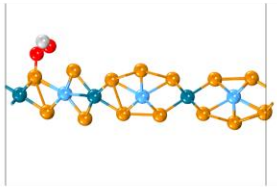	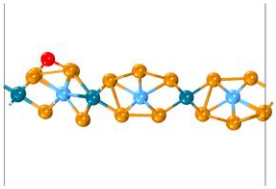	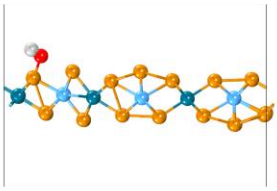
ΔZPE	\	0.43	0.06	0.33
ΔH	\	0.10	0.04	0.07
ΔTS	\	0.21	0.06	0.14
ΔG	\	4.16	1.81	0.85
PDS	$O_2 \rightarrow$ OOH*		**U_L(ORR)**	0.76

Fig. S17. Optimized structures and computed thermodynamic data (include ΔZPE, ΔH, ΔTS, and ΔG) of oxygen-containing species on the **$Ta_3Te_{14}Pd_3$** surface. The corresponding U_L value for **ORR** is also shown.

	TePt	OOH*	O*	OH*
Top view	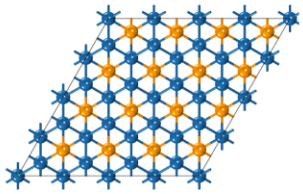	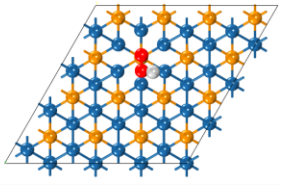	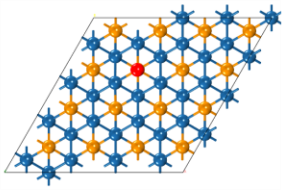	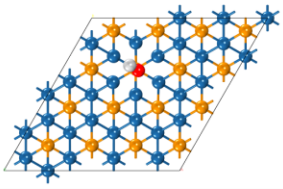
Side view	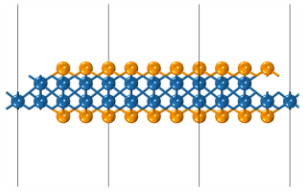	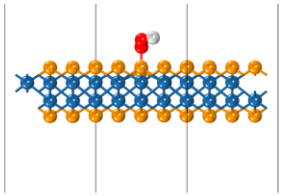	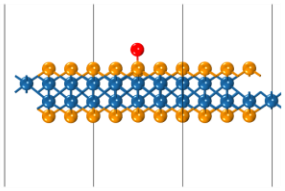	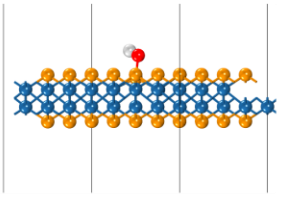
ΔZPE	\	0.42	0.06	0.33
ΔH	\	0.10	0.04	0.04
ΔTS	\	0.22	0.09	0.08
ΔG	\	4.02	1.83	0.80
PDS	$OH^* \rightarrow H_2O$		**U_L(ORR)**	0.80

Fig. S18. Optimized structures and computed thermodynamic data (include ΔZPE, ΔH, ΔTS, and ΔG) of oxygen-containing species on the **PtTe** surface. The corresponding U_L value for **ORR** is also shown.

	$Ge_5(Te_4As)_2$	OOH*	O*	OH*
Top view	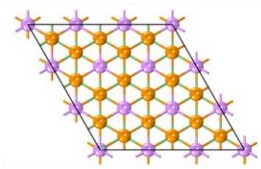	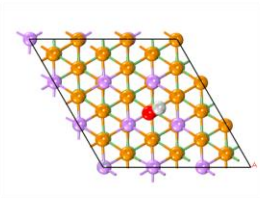	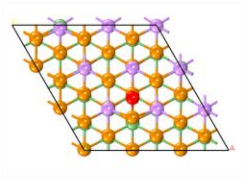	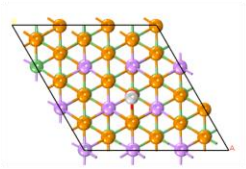
Side view	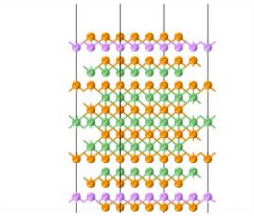	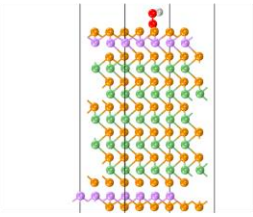	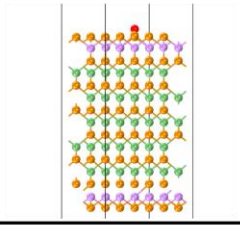	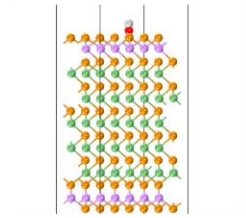
ΔZPE	\	0.41	0.05	0.32
ΔH	\	0.09	0.04	0.06
ΔTS	\	0.17	0.09	0.12
ΔG	\	4.24	1.73	1.04
PDS	$O_2 \rightarrow$ OOH*		**U_L(ORR)**	0.68

Fig. S19. Optimized structures and computed thermodynamic data (include ΔZPE, ΔH, ΔTS, and ΔG) of oxygen-containing species on the **$Ge_5(Te_4As)_2$** surface. The corresponding U_L value for **ORR** is also shown.

	$MoTe_2$	OOH*	O*	OH*
Top view	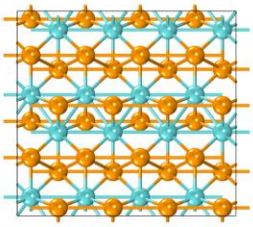	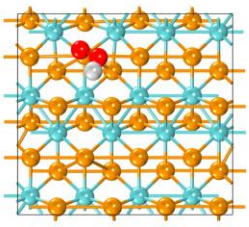	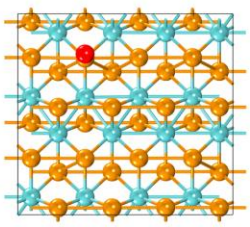	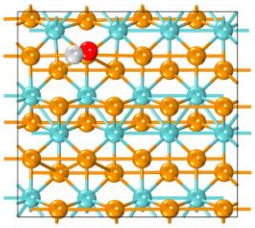
Side view	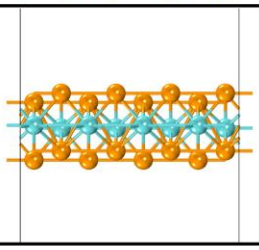	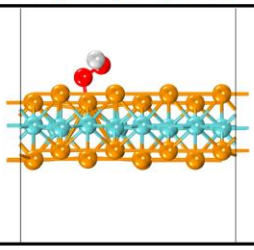	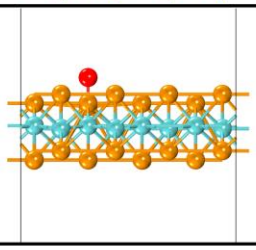	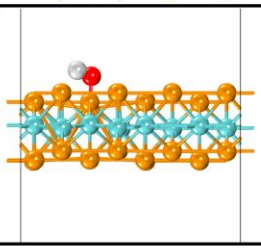
ΔZPE	\	0.43	0.06	0.34
ΔH	\	0.10	0.04	0.06
ΔTS	\	0.19	0.08	0.11
ΔG	\	4.08	1.95	0.82
PDS	$O_2 \rightarrow$ OOH*		**U_L(ORR)**	0.82

Fig. S20. Optimized structures and computed thermodynamic data (include ΔZPE, ΔH, ΔTS, and ΔG) of oxygen-containing species on the **$MoTe_2$** surface. The corresponding U_L value for **ORR** is also shown.

	$Ge_4Te_7As_2$	OOH*	O*	OH*
Top view	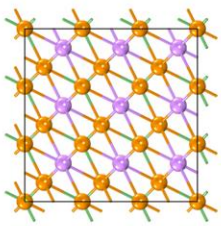	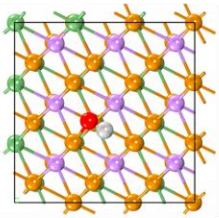	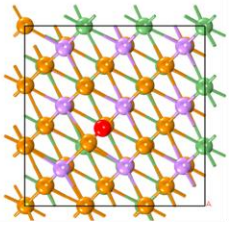	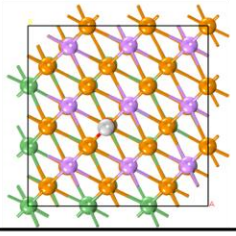
Side view	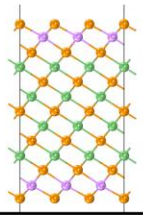	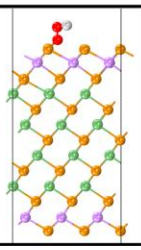	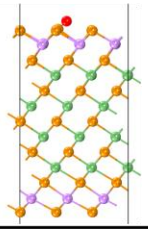	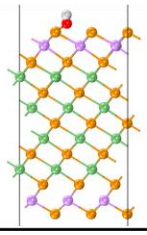
ΔZPE	\	0.41	0.05	0.32
ΔH	\	0.11	0.04	0.06
ΔTS	\	0.24	0.09	0.12
ΔG	\	4.32	1.83	1.17
PDS	$O_2 \rightarrow$ OOH*		**U_L(ORR)**	0.60

Fig. S21. Optimized structures and computed thermodynamic data (include ΔZPE, ΔH, ΔTS, and ΔG) of oxygen-containing species on the **$Ge_4Te_7As_2$** surface. The corresponding U_L value for **ORR** is also shown.

	NiTe	OOH*	O*	OH*
Top view	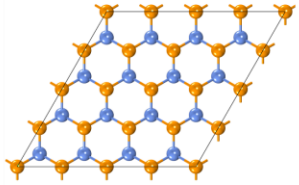	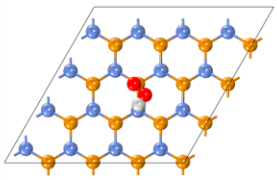	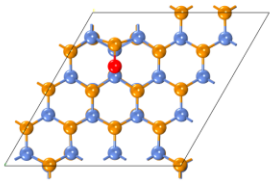	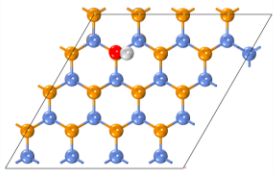
Side view	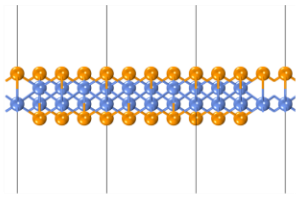	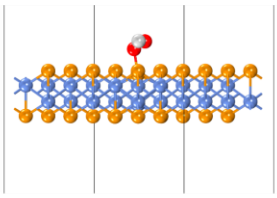	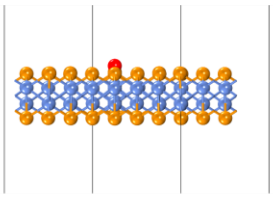	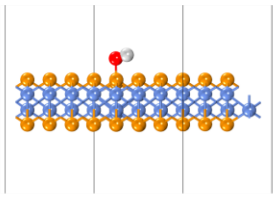
ΔZPE	\	0.42	0.06	0.33
ΔH	\	0.10	0.03	0.07
ΔTS	\	0.22	0.06	0.15
ΔG	\	4.09	2.00	0..88
PDS	$O_2 \rightarrow$ OOH*		**U_L(ORR)**	0.83

Fig. S22. Optimized structures and computed thermodynamic data (include ΔZPE, ΔH, ΔTS, and ΔG) of oxygen-containing species on the **NiTe** surface. The corresponding U_L value for **ORR** is also shown.

	BiTe	OOH*	O*	OH*
Top view	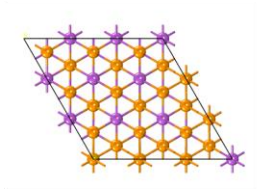	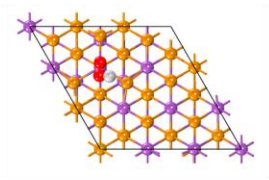	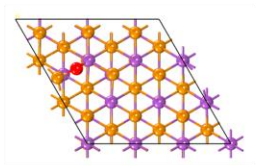	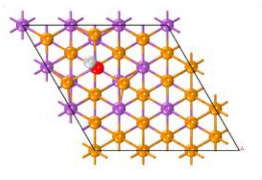
Side view	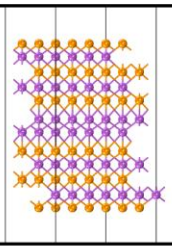	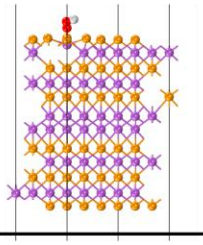	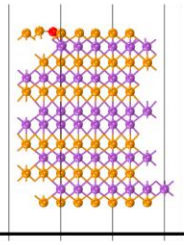	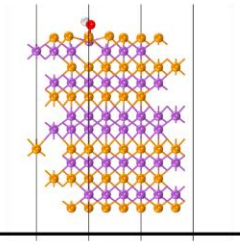
ΔZPE	\	0.42	0.06	0.34
ΔH	\	0.10	0.04	0.06
ΔTS	\	0.20	0.08	0.11
ΔG	\	4.28	1.78	1.09
PDS	$O_2 \rightarrow$ OOH*		U_L(ORR)	0.64

Fig. S23. Optimized structures and computed thermodynamic data (include ΔZPE, ΔH, ΔTS, and ΔG) of oxygen-containing species on the **BiTe** surface. The corresponding U_L value for **ORR** is also shown.

	$NbTe_2$	OOH*	O*	OH*
Top view	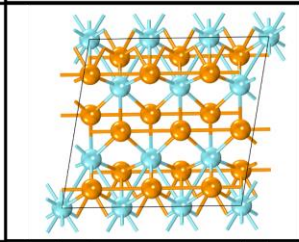	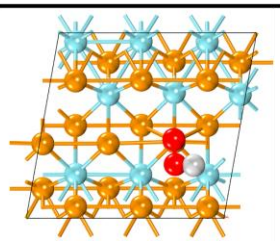	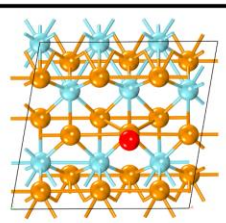	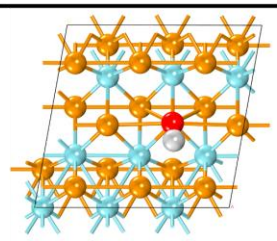
Side view	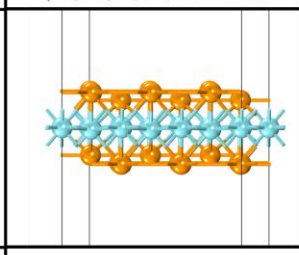	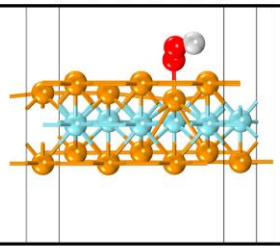	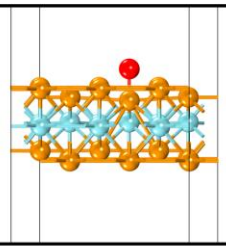	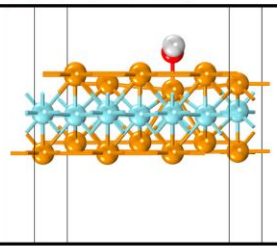
ΔZPE	\	0.43	0.06	0.33
ΔH	\	0.07	0.04	0.07
ΔTS	\	0.14	0.08	0.14
ΔG	\	3.95	2.00	0.66
PDS	$OH^* \rightarrow H_2O$		U_L(ORR)	0.66

Fig. S24. Optimized structures and computed thermodynamic data (include ΔZPE, ΔH, ΔTS, and ΔG) of oxygen-containing species on the **$NbTe_2$** surface. The corresponding U_L value for **ORR** is also shown.

	$Mn(InSe_2)_2$	OOH*	O*	OH*
Top view	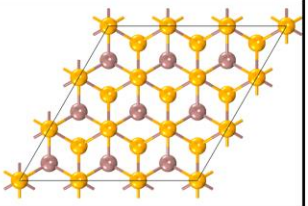	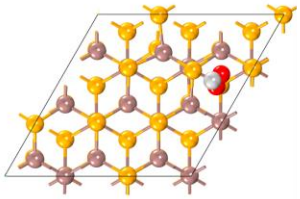	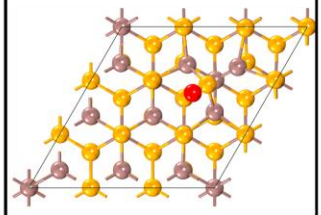	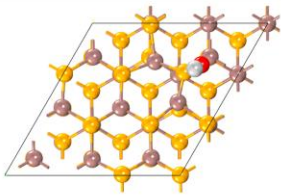
Side view	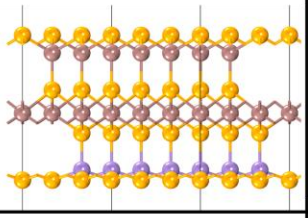	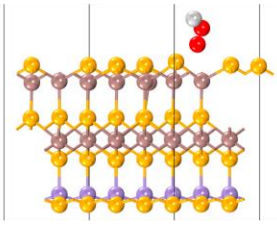	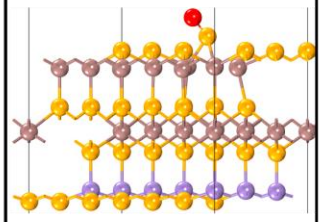	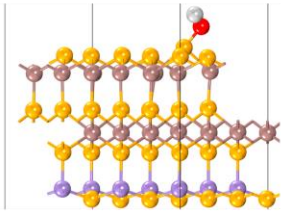
ΔZPE	\	0.42	0.06	0.33
ΔH	\	0.08	0.04	0.07
ΔTS	\	0.17	0.09	0.14
ΔG	\	4.27	1.84	1.12
PDS	$O_2 \rightarrow$ OOH*		**U_L(ORR)**	0.65

Fig. S25. Optimized structures and computed thermodynamic data (include ΔZPE, ΔH, ΔTS, and ΔG) of oxygen-containing species on the **$Mn(InSe_2)_2$** surface. The corresponding U_L value for **ORR** is also shown.

	Nb_4IrSe_{10}	OOH*	O*	OH*
Top view	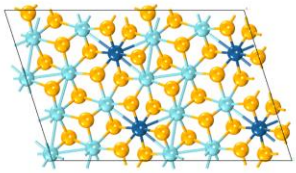	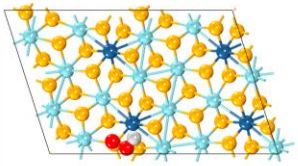	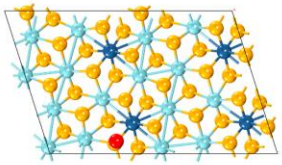	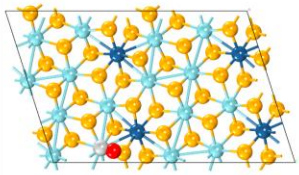
Side view	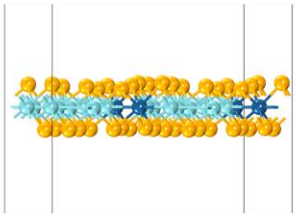	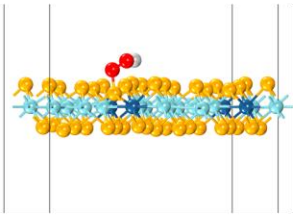	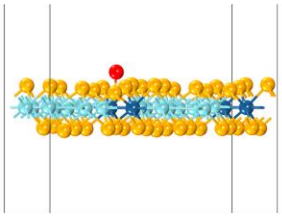	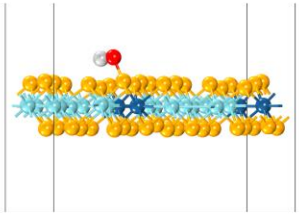
ΔZPE	\	0.44	0.06	0.33
ΔH	\	0.09	0.04	0.06
ΔTS	\	0.18	0.07	0.13
ΔG	\	4.26	2.26	1.43
PDS	$O_2 \rightarrow$ OOH*		**U_L(ORR)**	0.66

Fig. S26. Optimized structures and computed thermodynamic data (include ΔZPE, ΔH, ΔTS, and ΔG) of oxygen-containing species on the **Nb_4IrSe_{10}** surface. The corresponding U_L value for **ORR** is also shown.

	TaS_2	OOH*	O*	OH*
Top view	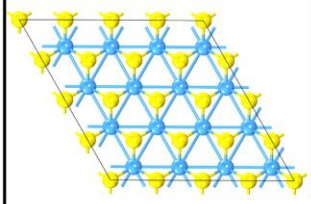	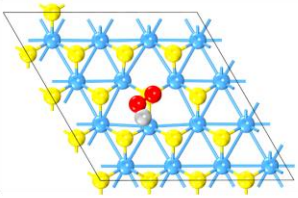	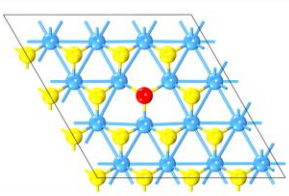	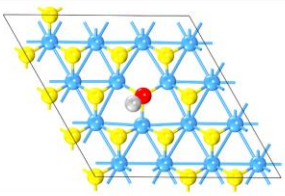
Side view	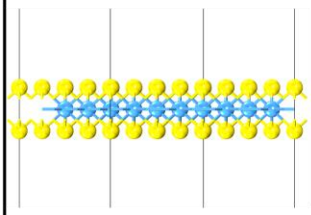	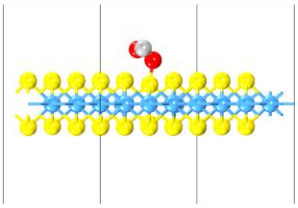	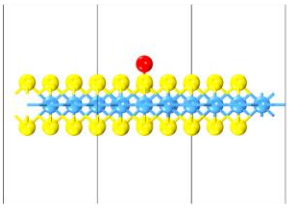	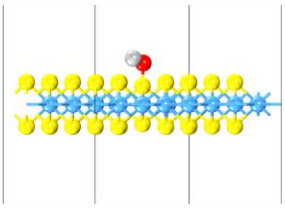
ΔZPE	\	0.44	0.08	0.35
ΔH	\	0.09	0.03	0.06
ΔTS	\	0.18	0.06	0.13
ΔG	\	4.12	1.65	0.70
PDS	$OH^* \rightarrow H_2O$		**U_L(ORR)**	0.70

Fig. S27. Optimized structures and computed thermodynamic data (include ΔZPE, ΔH, ΔTS, and ΔG) of oxygen-containing species on the **TaS_2** surface. The corresponding U_L value for **ORR** is also shown.

	BiSe	OOH*	O*	OH*
Top view	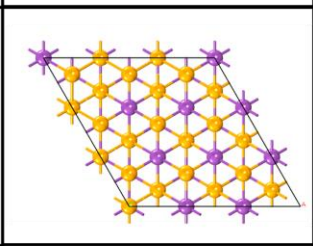	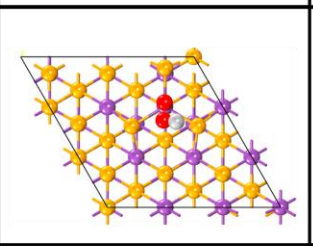	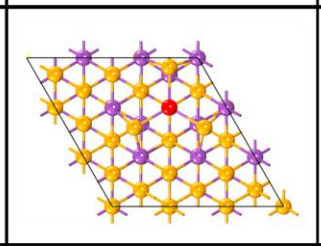	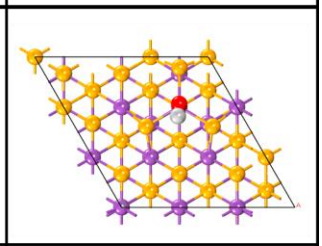
Side view	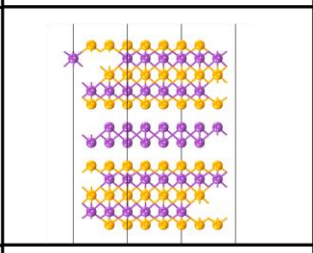	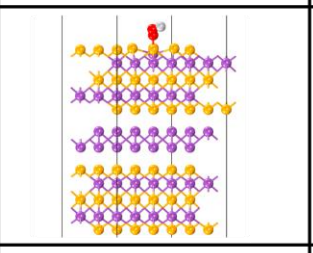	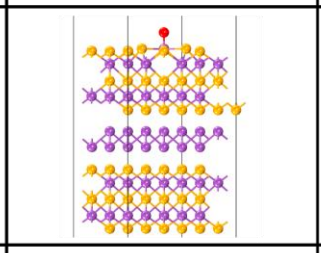	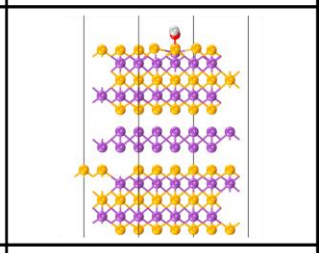
ΔZPE	\	0.43	0.05	0.34
ΔH	\	0.10	0.04	0.06
ΔTS	\	0.20	0.10	0.11
ΔG	\	3.96	2.70	0.68
PDS	$OH^* \rightarrow H_2O$		U_L(ORR)	0.68

Fig. S28. Optimized structures and computed thermodynamic data (include ΔZPE, ΔH, ΔTS, and ΔG) of oxygen-containing species on the **BiSe** surface. The corresponding U_L value for **ORR** is also shown.

	Fe_4S_5	OOH*	O*	OH*
Top view	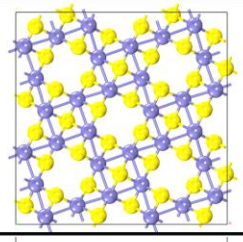	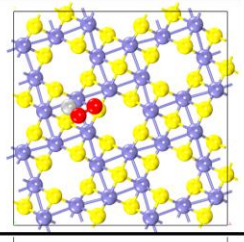	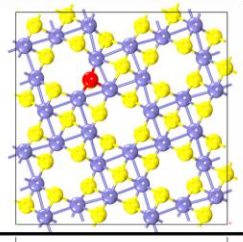	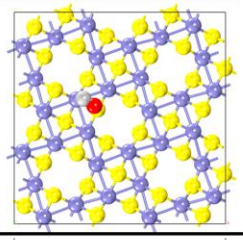
Side view	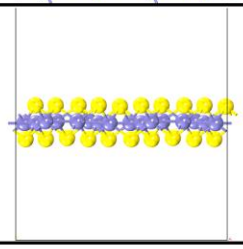	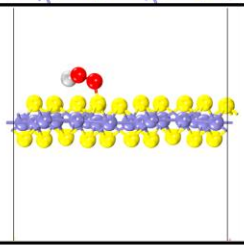	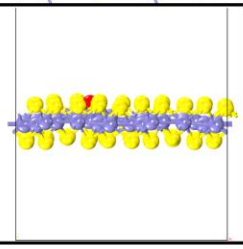	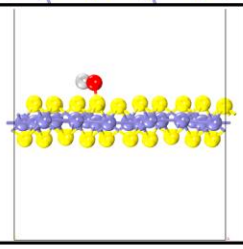
ΔZPE	\	0.43	0.08	0.34
ΔH	\	0.10	0.02	0.06
ΔTS	\	0.20	0.03	0.12
ΔG	\	3.93	1.83	0.70
PDS	$OH^* \rightarrow H_2O$		U_L(ORR)	0.70

Fig. S29. Optimized structures and computed thermodynamic data (include ΔZPE, ΔH, ΔTS, and ΔG) of oxygen-containing species on the **Fe_4S_5** surface. The corresponding U_L value for **ORR** is also shown.

	$NbSe_2$	OOH*	O*	OH*
Top view	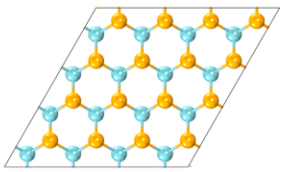	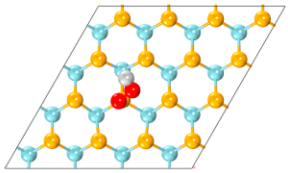	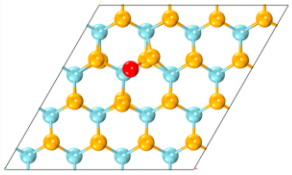	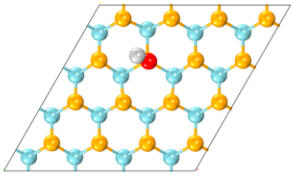
Side view	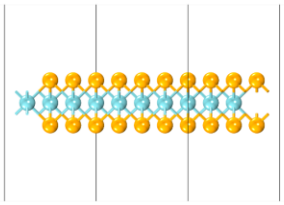	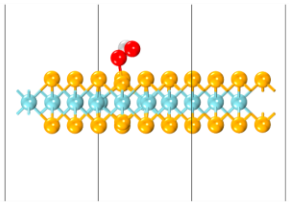	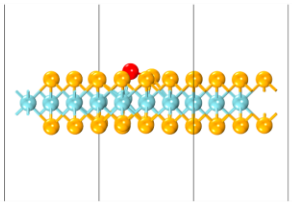	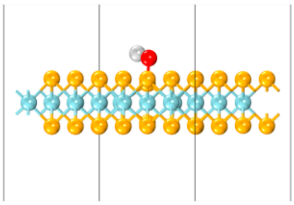
ΔZPE	\	0.44	0.07	0.34
ΔH	\	0.09	0.03	0.06
ΔTS	\	0.20	0.05	0.13
ΔG	\	4.12	2.13	0.83
PDS	$O_2 \rightarrow$ OOH*		U_L(ORR)	0.80

Fig. S30. Optimized structures and computed thermodynamic data (include ΔZPE, ΔH, ΔTS, and ΔG) of oxygen-containing species on the **$NbSe_2$** surface. The corresponding U_L value for **ORR** is also shown.

	$TaSe_2$	OOH*	O*	OH*
Top view	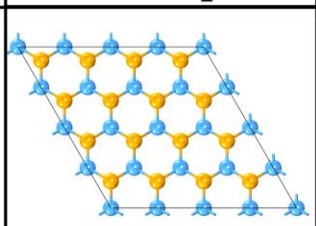	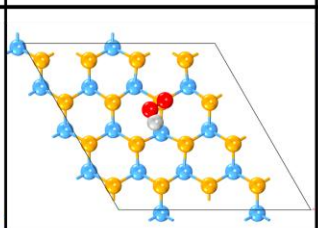	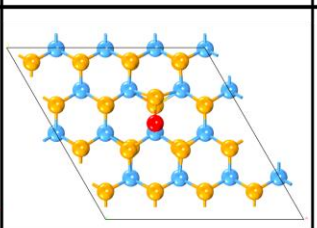	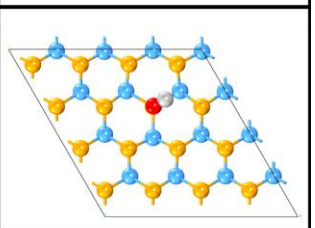
Side view	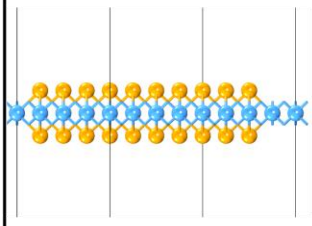	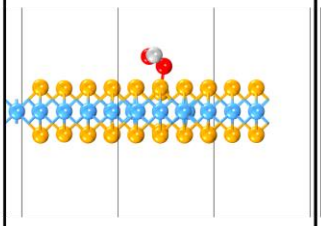	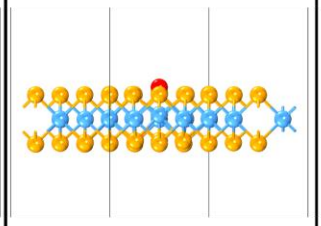	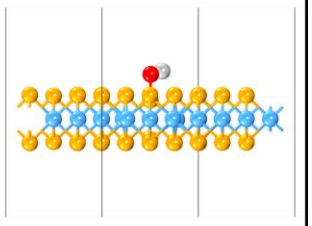
ΔZPE	\	0.44	0.07	0.34
ΔH	\	0.09	0.03	0.04
ΔTS	\	0.20	0.05	0.08
ΔG	\	4.18	2.17	0.90
PDS	$O_2 \rightarrow$ OOH*		U_L(ORR)	0.74

Fig. S31. Optimized structures and computed thermodynamic data (include ΔZPE, ΔH, ΔTS, and ΔG) of oxygen-containing species on the **$TaSe_2$** surface. The corresponding U_L value for **ORR** is also shown.

	ZrSiSe	OOH*	O*	OH*
Top view	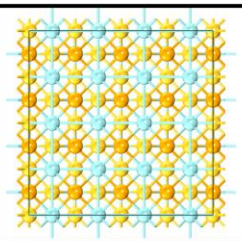	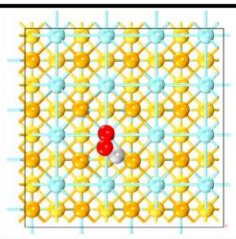	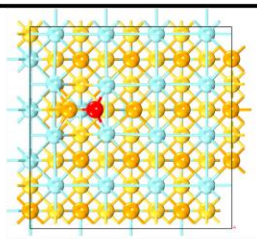	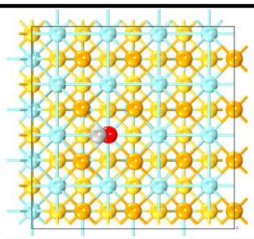
Side view	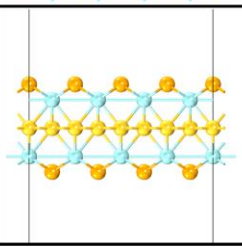	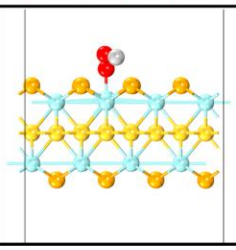	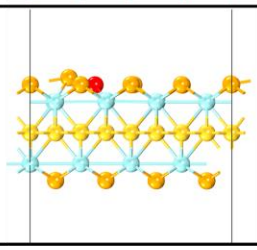	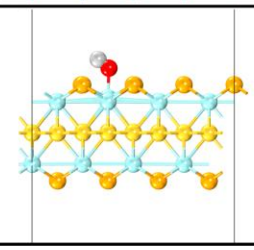
ΔZPE	\	0.42	0.07	0.32
ΔH	\	0.09	0.03	0.04
ΔTS	\	0.18	0.04	0.07
ΔG	\	4.12	1.58	0.71
PDS	$OH^* \rightarrow H_2O$		U_L(ORR)	0.71

Fig. S32. Optimized structures and computed thermodynamic data (include ΔZPE, ΔH, ΔTS, and ΔG) of oxygen-containing species on the **ZrSiSe** surface. The corresponding U_L value for **ORR** is also shown.

	GdBr	OOH*	O*	OH*
Top view	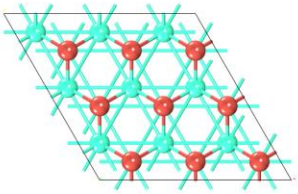	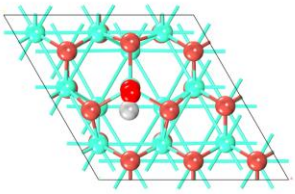	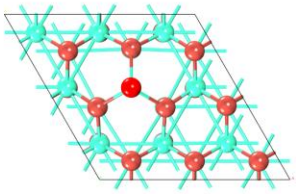	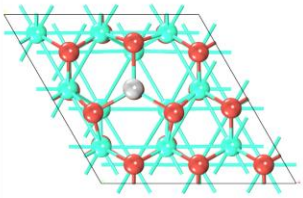
Side view	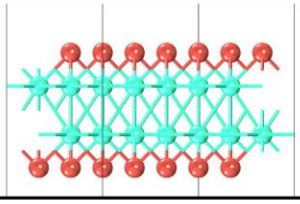	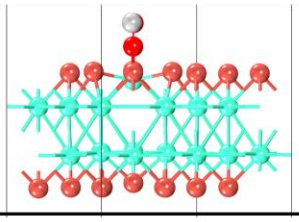	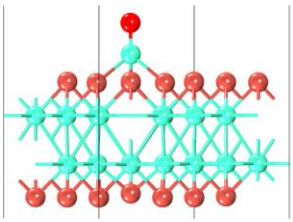	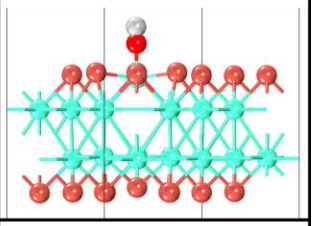
ΔZPE	\	0.43	0.06	0.33
ΔH	\	0.08	0.05	0.06
ΔTS	\	0.17	0.12	0.11
ΔG	\	4.19	1.91	0.61
PDS	OH* → H_2O		U_L(ORR)	0.61

Fig. S33. Optimized structures and computed thermodynamic data (include ΔZPE, ΔH, ΔTS, and ΔG) of oxygen-containing species on the **GdBr** surface. The corresponding U_L value for **ORR** is also shown.

	$CrGeTe_3$	OOH*	O*	OH*
Top view	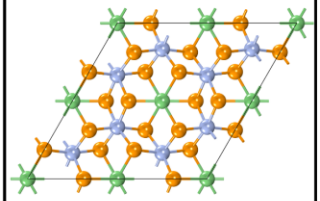	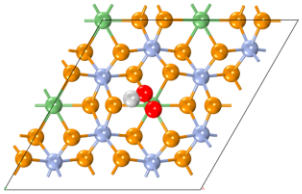	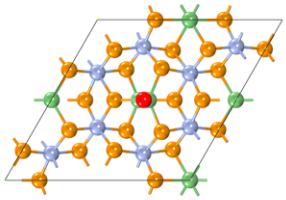	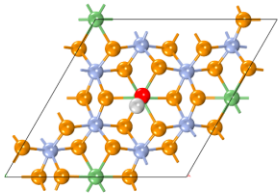
Side view	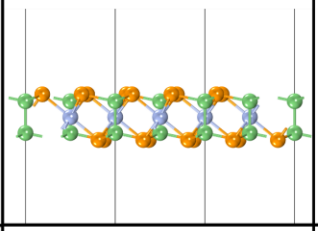	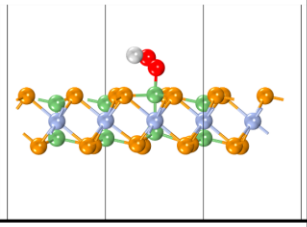	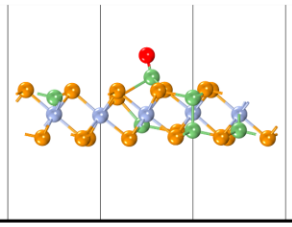	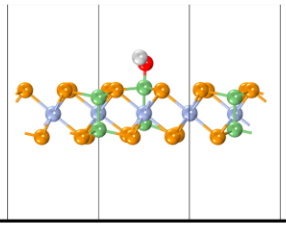
ΔZPE	\	0.43	0.06	0.34
ΔH	\	0.09	0.04	0.06
ΔTS	\	0.19	0.08	0.11
ΔG	\	4.10	2.45	0.86
PDS	$O_2 \rightarrow$ OOH*		**U_L(ORR)**	0.82

Fig. S34. Optimized structures and computed thermodynamic data (include ΔZPE, ΔH, ΔTS, and ΔG) of oxygen-containing species on the **$CrGeTe_3$** surface. The corresponding U_L value for **ORR** is also shown.

	$PtPb_4$	OOH*	O*	OH*
Top view	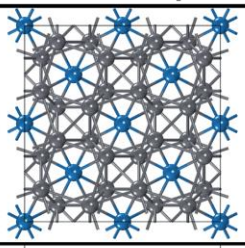	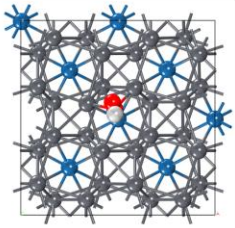	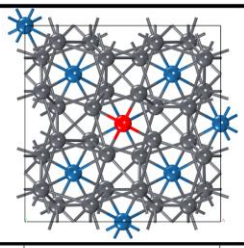	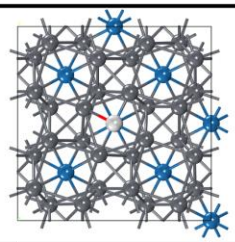
Side view	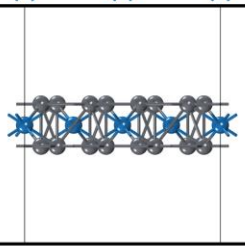	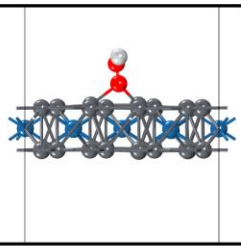	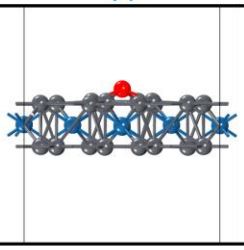	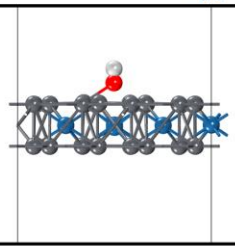
ΔZPE	\	0.41	0.02	0.30
ΔH	\	0.11	0.06	0.03
ΔTS	\	0.22	0.14	0.04
ΔG	\	3.65	1.83	0.65
PDS	$OH^* \rightarrow H_2O$		U_L(ORR)	0.65

Fig. S35. Optimized structures and computed thermodynamic data (include ΔZPE, ΔH, ΔTS, and ΔG) of oxygen-containing species on the **$PtPb_4$** surface. The corresponding U_L value for **ORR** is also shown.

	$CuH_2(SeO_3)_2$	OOH*	O*	OH*
Top view	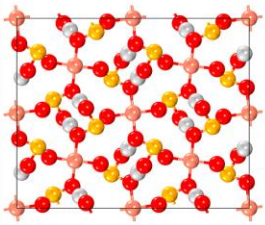	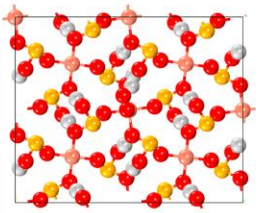	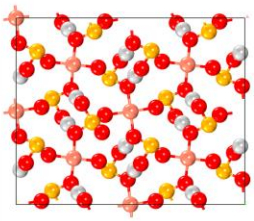	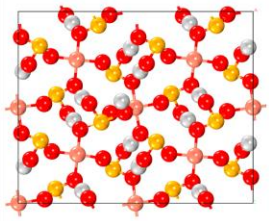
Side view	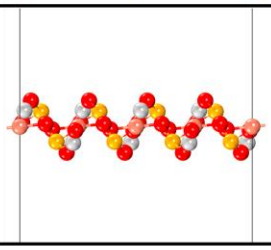	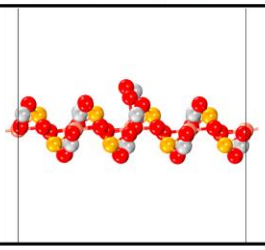	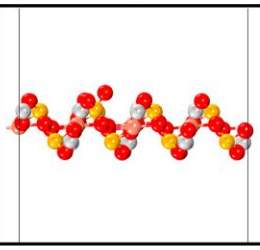	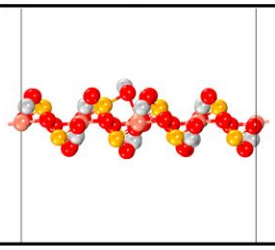
ΔZPE	\	0.42	0.08	0.35
ΔH	\	0.10	0.03	0.05
ΔTS	\	0.21	0.05	0.08
ΔG	\	4.20	2.50	1.77
PDS	$O_2 \rightarrow$ OOH*		**U_L(ORR)**	0.72

Fig. S36. Optimized structures and computed thermodynamic data (include ΔZPE, ΔH, ΔTS, and ΔG) of oxygen-containing species on the **$CuH_2(SeO_3)_2$** surface. The corresponding U_L value for **ORR** is also shown.

	$Ag(AuS)_2$	OOH*	O*	OH*
Top view	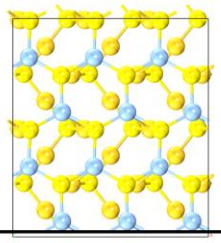	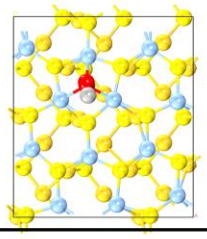	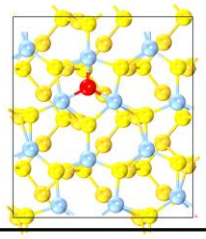	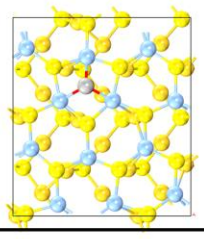
Side view	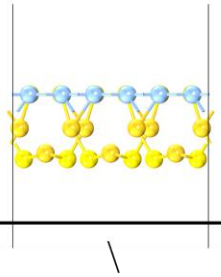	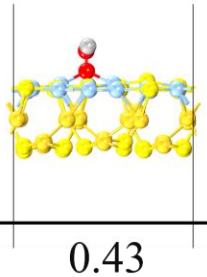	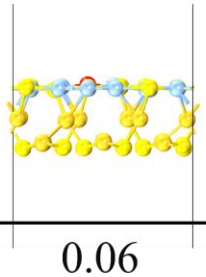	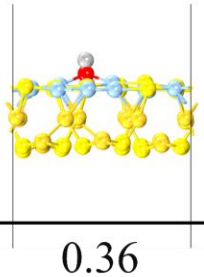
ΔZPE	\	0.43	0.06	0.36
ΔH	\	0.10	0.03	0.05
ΔTS	\	0.19	0.05	0.08
ΔG	\	4.16	2.34	1.01
PDS	$O_2 \rightarrow$ OOH*		U_L(ORR)	0.76

Fig. S37. Optimized structures and computed thermodynamic data (include ΔZPE, ΔH, ΔTS, and ΔG) of oxygen-containing species on the **$Ag(AuS)_2$** surface. The corresponding U_L value for **ORR** is also shown.

	Nb_9IrSe_{20}	OOH*	O*	OH*
Top view	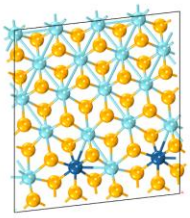	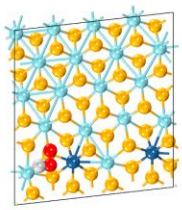	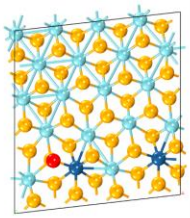	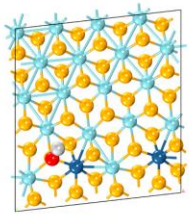
Side view	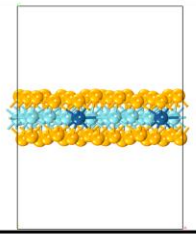	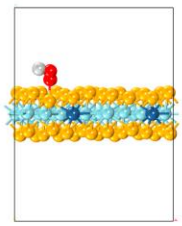	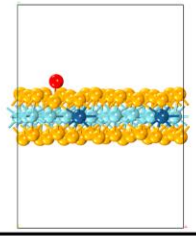	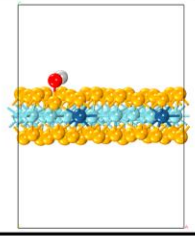
ΔZPE	\	0.44	0.06	0.35
ΔH	\	0.09	0.04	0.06
ΔTS	\	0.20	0.07	0.06
ΔG	\	4.19	2.27	0.93
PDS	$O_2 \rightarrow$ OOH*		**U_L(ORR)**	0.73

Fig. S38. Optimized structures and computed thermodynamic data (include ΔZPE, ΔH, ΔTS, and ΔG) of oxygen-containing species on the **Nb_9IrSe_{20}** surface. The corresponding U_L value for **ORR** is also shown.

	$AgHO_2$	OOH*	O*	OH*
Top view	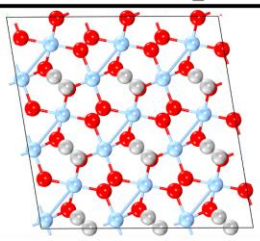	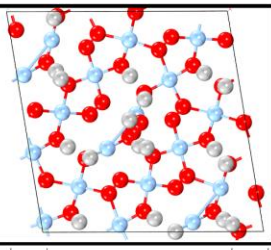	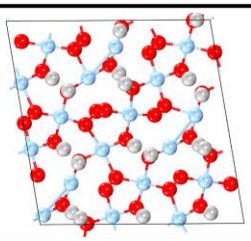	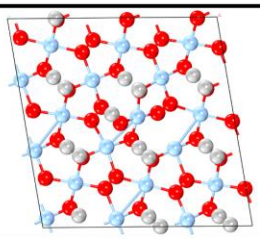
Side view	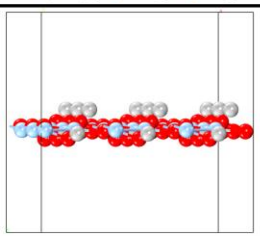	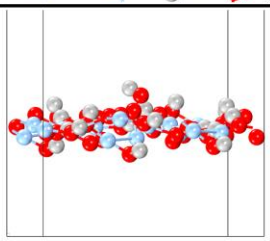	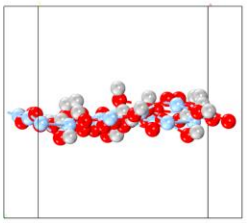	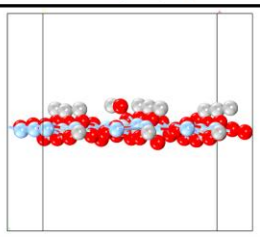
ΔZPE	\	0.42	0.08	0.34
ΔH	\	0.10	0.03	0.06
ΔTS	\	0.21	0.04	0.11
ΔG	\	3.70	2.38	1.21
PDS	O* → OH*		**U_L(ORR)**	1.17

Fig. S39. Optimized structures and computed thermodynamic data (include ΔZPE, ΔH, ΔTS, and ΔG) of oxygen-containing species on the **$AgHO_2$** surface. The corresponding U_L value for **ORR** is also shown.

	La_2PI_2	OOH*	O*	OH*
Top view	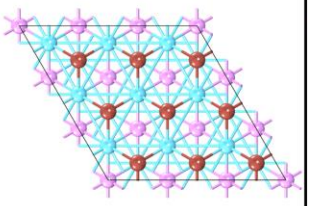	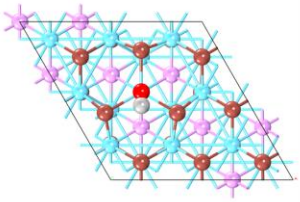	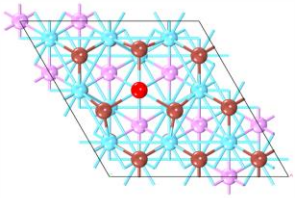	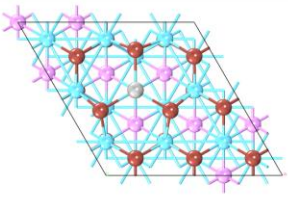
Side view	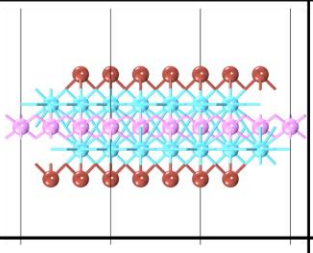	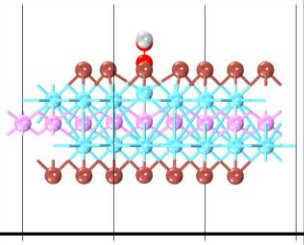	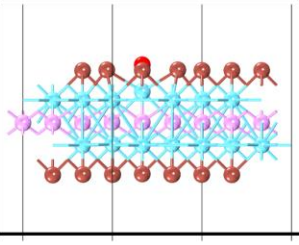	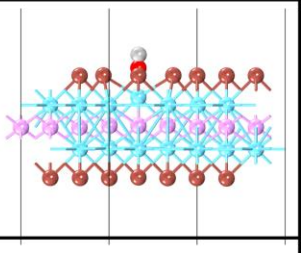
ΔZPE	\	0.43	0.06	0.33
ΔH	\	0.08	0.04	0.06
ΔTS	\	0.16	0.07	0.10
ΔG	\	4.28	2.37	0.87
PDS	$O_2 \rightarrow$ OOH*		**U_L(ORR)**	0.64

Fig. S40. Optimized structures and computed thermodynamic data (include ΔZPE, ΔH, ΔTS, and ΔG) of oxygen-containing species on the **La_2PI_2** surface. The corresponding U_L value for **ORR** is also shown.

	TbGaI	OOH*	O*	OH*
Top view	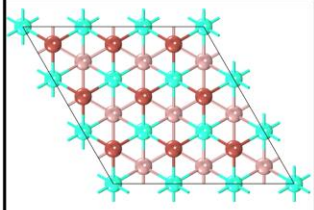	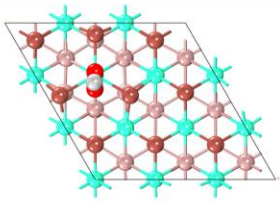	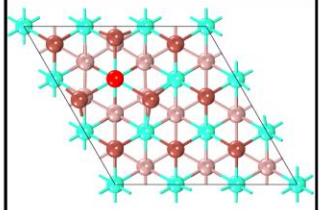	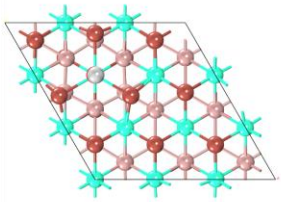
Side view	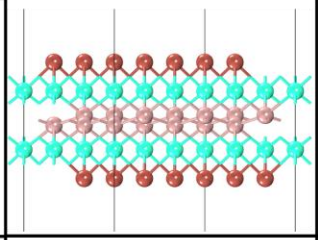	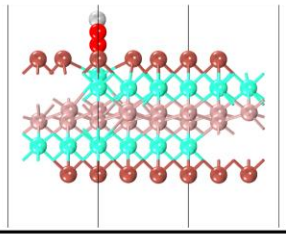	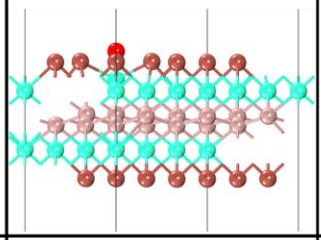	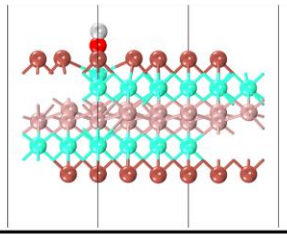
ΔZPE	\	0.43	0.06	0.31
ΔH	\	0.09	0.04	0.07
ΔTS	\	0.17	0.08	0.14
ΔG	\	4.24	2.71	0.85
PDS	$O_2 \rightarrow$ OOH*		U_L(ORR)	0.68

Fig. S41. Optimized structures and computed thermodynamic data (include ΔZPE, ΔH, ΔTS, and ΔG) of oxygen-containing species on the **TbGaI** surface. The corresponding U_L value for **ORR** is also shown.

	CeI_3	OOH*	O*	OH*
Top view	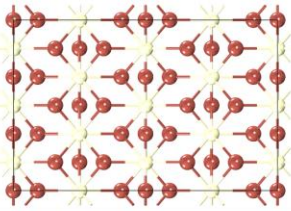	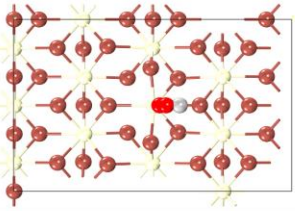	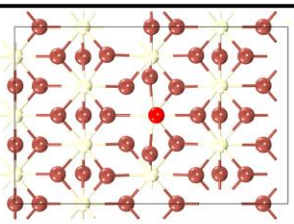	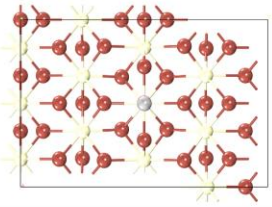
Side view	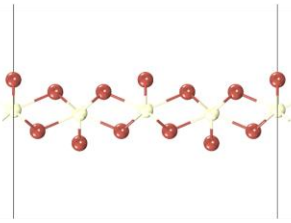	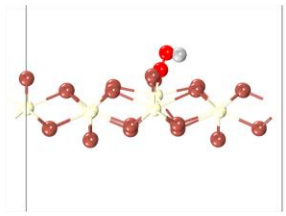	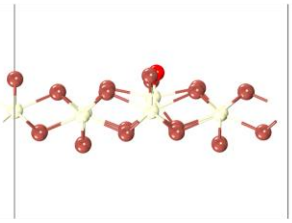	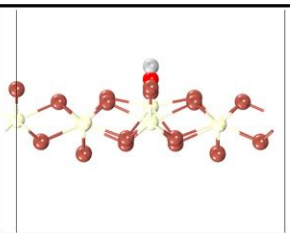
ΔZPE	\	0.44	0.04	0.33
ΔH	\	0.09	0.03	0.06
ΔTS	\	0.18	0.03	0.11
ΔG	\	3.29	1.44	0.79
PDS	O*→ OH*		U_L(ORR)	0.65

Fig. S42. Optimized structures and computed thermodynamic data (include ΔZPE, ΔH, ΔTS, and ΔG) of oxygen-containing species on the **CeI_3** surface. The corresponding U_L value for **ORR** is also shown.

	$Sc_6C_2I_{11}$	OH*	O*	OOH*
Top view	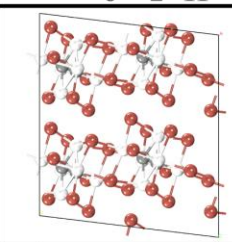	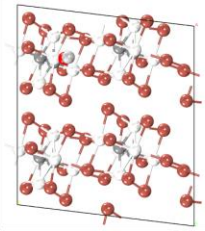	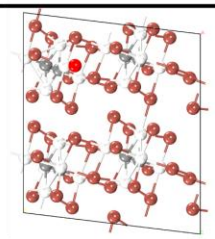	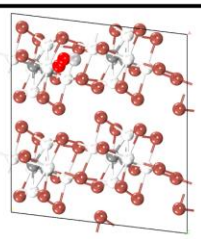
Side view	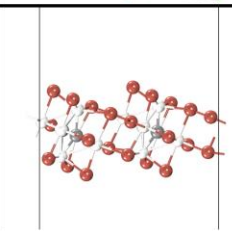	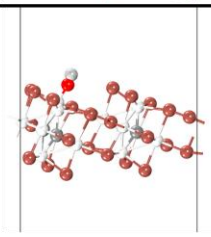	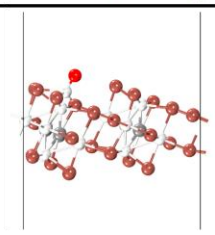	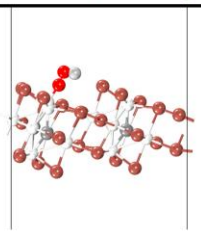
ΔZPE	\	0.33	0.06	0.44
ΔH	\	0.06	0.04	0.10
ΔTS	\	0.12	0.10	0.21
ΔG	\	-0.44	1.18	3.01
PDS	$OOH^* \rightarrow O_2$		**U_L(OER)**	1.91

Fig. S43. Optimized structures and computed thermodynamic data (include ΔZPE, ΔH, ΔTS, and ΔG) of oxygen-containing species on the **$Sc_6C_2I_{11}$** surface. The corresponding U_L value for **OER** is also shown.

	$Li_2Cu_2F_5$	OH*	O*	OOH*
Top view	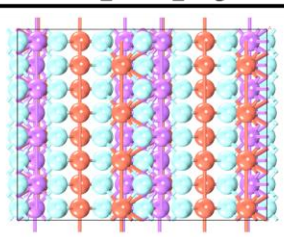	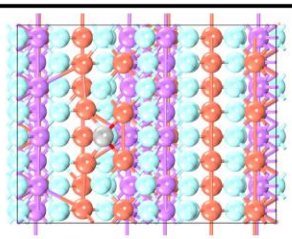	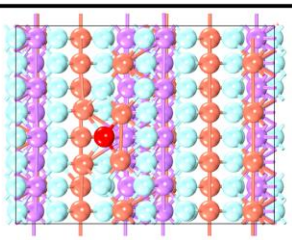	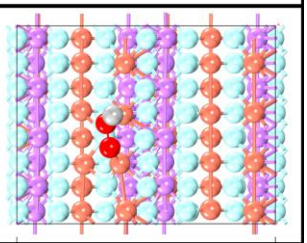
Side view	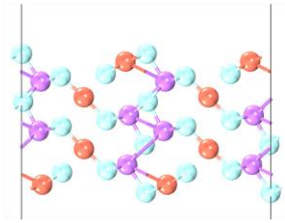	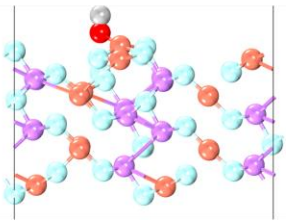	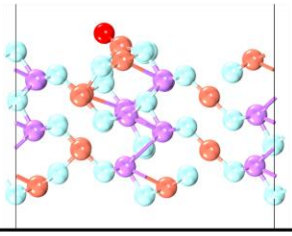	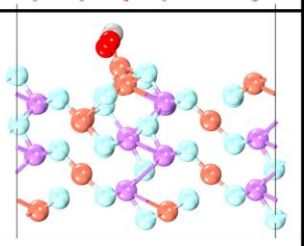
ΔZPE	\	0.37	0.07	0.44
ΔH	\	0.04	0.03	0.09
ΔTS	\	0.07	0.05	0.18
ΔG	\	0.53	2.38	4.11
PDS	O*→ OOH*		**U_L(OER)**	1.73

Fig. S44. Optimized structures and computed thermodynamic data (include ΔZPE, ΔH, ΔTS, and ΔG) of oxygen-containing species on the **$Li_2Cu_2F_5$** surface. The corresponding U_L value for **OER** is also shown.

	$Te_2Pd_3Pb_2$	OH*	O*	OOH*
Top view	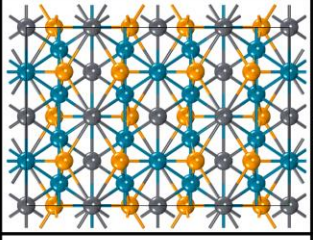	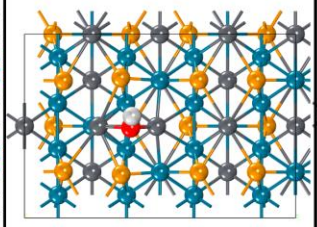	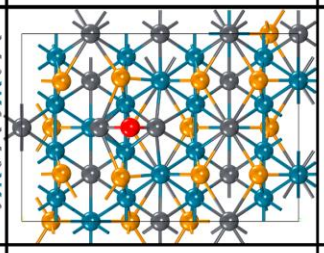	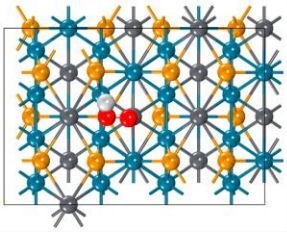
Side view	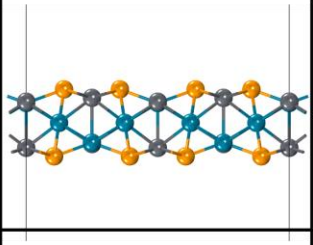	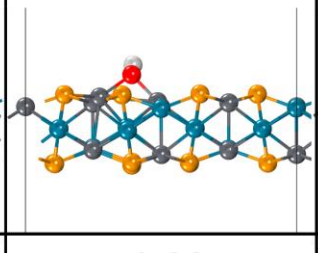	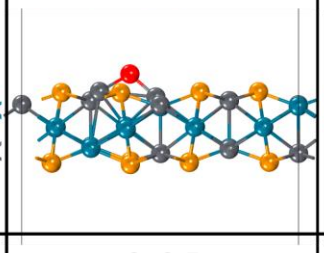	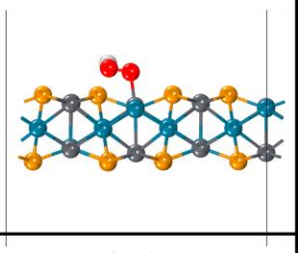
ΔZPE	\	0.33	0.05	0.41
ΔH	\	0.06	0.04	0.11
ΔTS	\	0.10	0.07	0.24
ΔG	\	0.50	1.97	3.70
PDS	O*→ OOH*		U_L(OER)	1.73

Fig. S45. Optimized structures and computed thermodynamic data (include ΔZPE, ΔH, ΔTS, and ΔG) of oxygen-containing species on the **$Pd_3Pb_2Te_2$** surface. The corresponding U_L value for **OER** is also shown.

	$Zn(InS_2)_2$	OH*	O*	OOH*
Top view	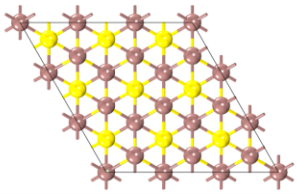	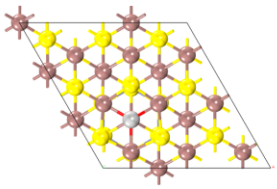	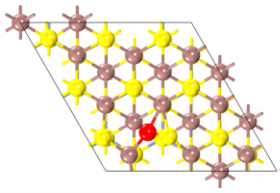	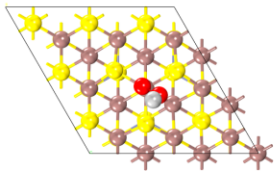
Side view	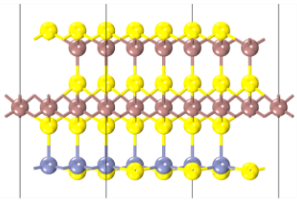	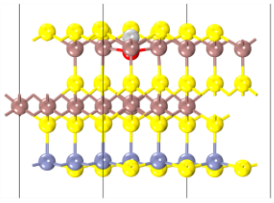	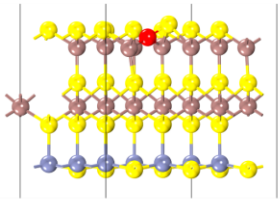	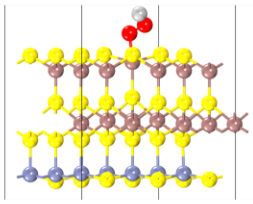
ΔZPE	\	0.41	0.07	0.42
ΔH	\	0.03	0.03	0.10
ΔTS	\	0.05	0.05	0.21
ΔG	\	1.10	2.54	4.41
PDS	O*→ OOH*		**U_L(OER)**	1.87

Fig. S46. Optimized structures and computed thermodynamic data (include ΔZPE, ΔH, ΔTS, and ΔG) of oxygen-containing species on the **$Zn(InS_2)_2$** surface. The corresponding U_L value for **OER** is also shown.

	$Ta(NiTe)_2$	OH*	O*	OOH*
Top view	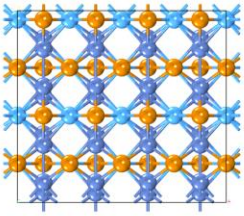	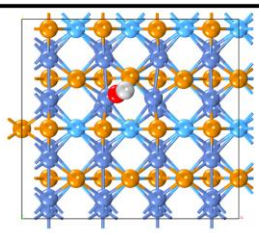	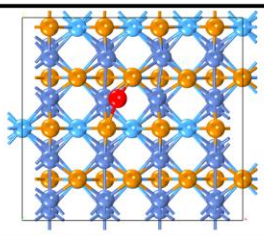	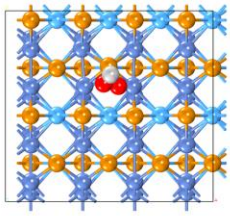
Side view	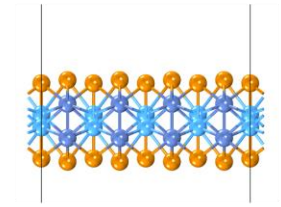	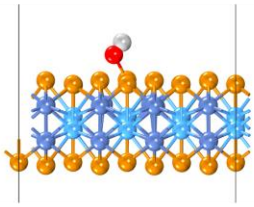	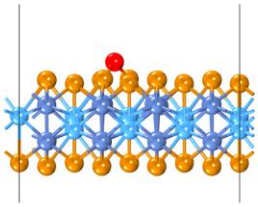	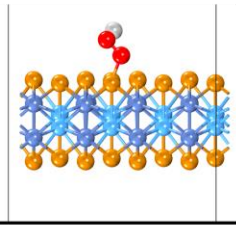
ΔZPE	\	0.32	0.05	0.41
ΔH	\	0.07	0.04	0.08
ΔTS	\	0.14	0.07	0.17
ΔG	\	1.46	2.71	4.62
PDS	O*→ OOH*		U_L(OER)	1.91

Fig. S47. Optimized structures and computed thermodynamic data (include ΔZPE, ΔH, ΔTS, and ΔG) of oxygen-containing species on the **$Ta(NiTe)_2$** surface. The corresponding U_L value for **OER** is also shown.

	VTe_2	OH*	O*	OOH*
Top view	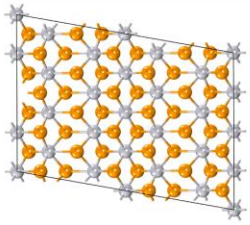	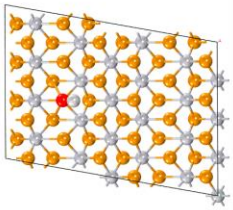	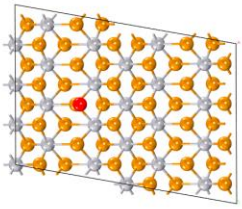	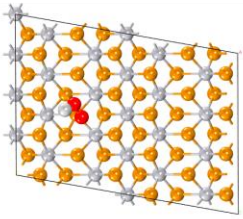
Side view	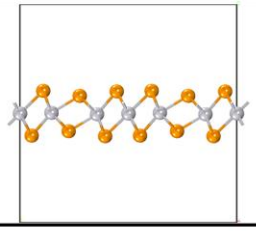	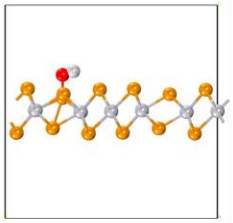	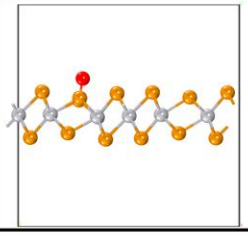	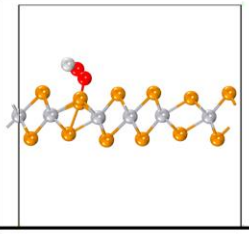
ΔZPE	\	0.33	0.06	0.43
ΔH	\	0.07	0.04	0.10
ΔTS	\	0.13	0.08	0.21
ΔG	\	0.57	1.93	3.85
PDS	O*→ OOH*		U_L(OER)	1.92

Fig. S48. Optimized structures and computed thermodynamic data (include ΔZPE, ΔH, ΔTS, and ΔG) of oxygen-containing species on the **TaS_2** surface. The corresponding U_L value for **OER** is also shown.

	Bi_3Se_4	OH*	O*	OOH*
Top view	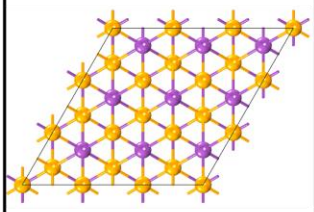	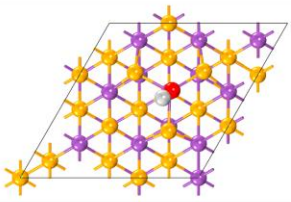	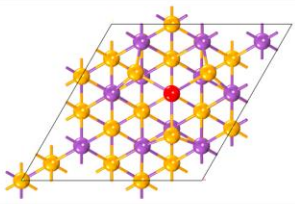	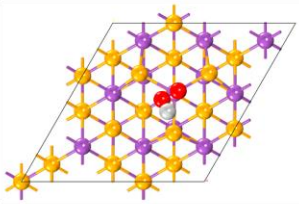
Side view	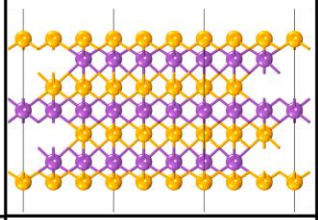	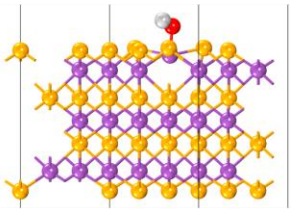	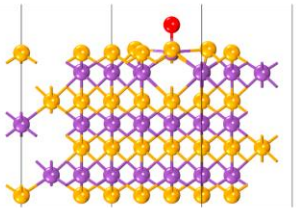	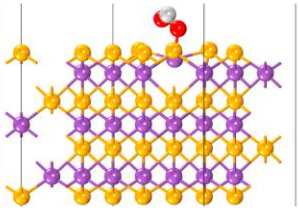
ΔZPE	\	0.34	0.06	0.43
ΔH	\	0.06	0.04	0.10
ΔTS	\	0.12	0.09	0.20
ΔG	\	0.32	1.70	3.61
PDS	O*→ OOH*		**U_L(OER)**	1.91

Fig. S49. Optimized structures and computed thermodynamic data (include ΔZPE, ΔH, ΔTS, and ΔG) of oxygen-containing species on the **Bi_3Se_4** surface. The corresponding U_L value for **OER** is also shown.

	$TaTe_2$	OH*	O*	OOH*
Top view	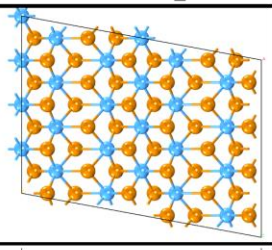	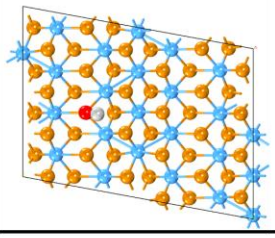	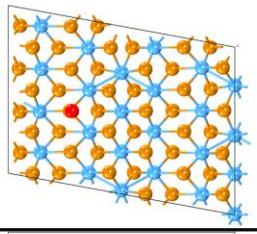	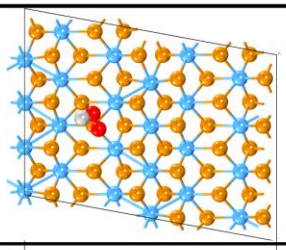
Side view	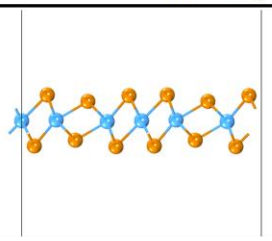	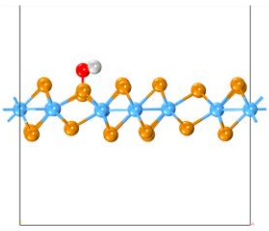	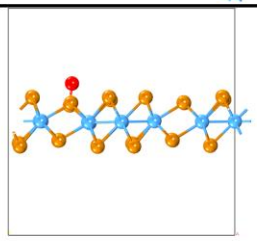	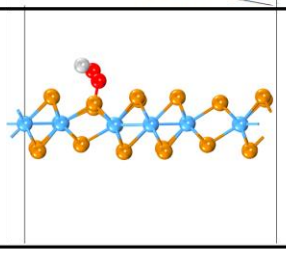
ΔZPE	\	0.34	0.06	0.43
ΔH	\	0.06	0.04	0.10
ΔTS	\	0.13	0.09	0.22
ΔG	\	0.29	1.77	3.55
PDS	O*→ OOH*		**U_L(OER)**	1.79

Fig. S50. Optimized structures and computed thermodynamic data (include ΔZPE, ΔH, ΔTS, and ΔG) of oxygen-containing species on the **$TaTe_2$** surface. The corresponding U_L value for **OER** is also shown.

	Nb_2Se_3	OH*	O*	OOH*
Top view	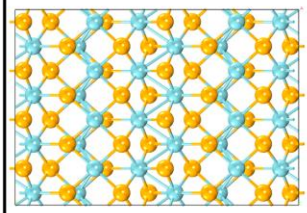	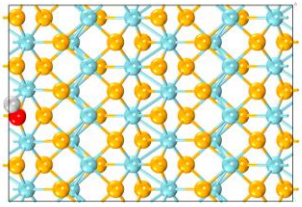	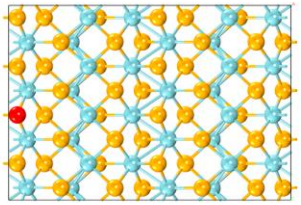	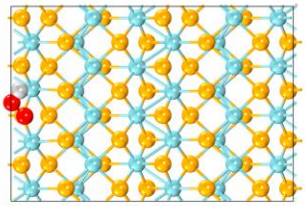
Side view	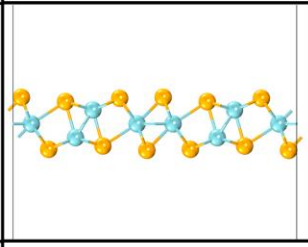	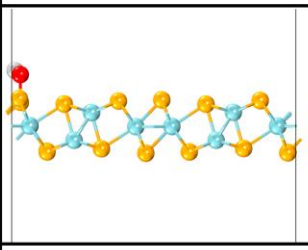	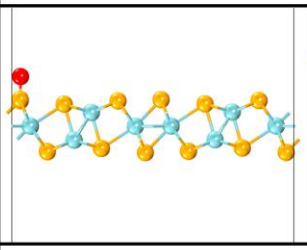	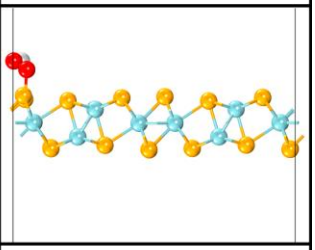
ΔZPE	\	0.33	0.06	0.42
ΔH	\	0.07	0.04	0.10
ΔTS	\	0.13	0.07	0.23
ΔG	\	1.45	2.71	4.59
PDS	O*→ OOH*		**U_L(OER)**	1.88

Fig. S51. Optimized structures and computed thermodynamic data (include ΔZPE, ΔH, ΔTS, and ΔG) of oxygen-containing species on the **Nb_2Se_3** surface. The corresponding U_L value for **OER** is also shown.

	Pr_2Br_5	OH*	O*	OOH*
Top view	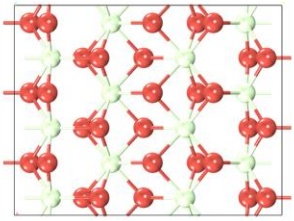	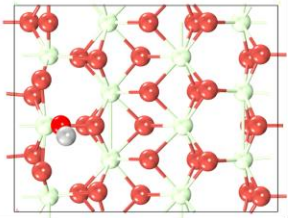	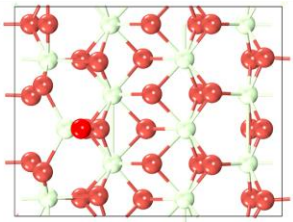	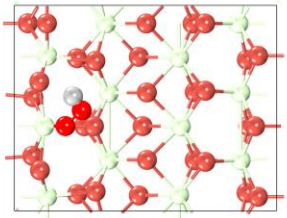
Side view	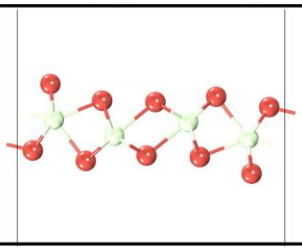	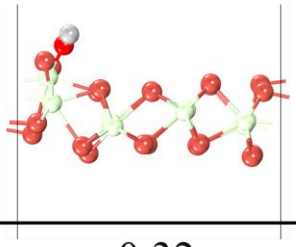	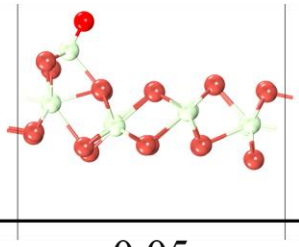	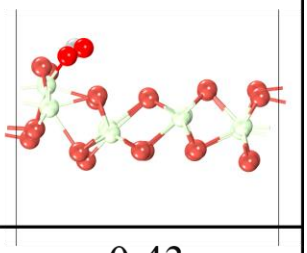
ΔZPE	\	0.32	0.05	0.43
ΔH	\	0.07	0.02	0.10
ΔTS	\	0.13	0.04	0.19
ΔG	\	0.22	1.87	3.66
PDS	O*→ OOH*		**U_L(OER)**	1.79

Fig. S52. Optimized structures and computed thermodynamic data (include ΔZPE, ΔH, ΔTS, and ΔG) of oxygen-containing species on the **Pr_2Br_5** surface. The corresponding U_L value for **OER** is also shown.

	CeZnPO	OH*	O*	OOH*
Top view	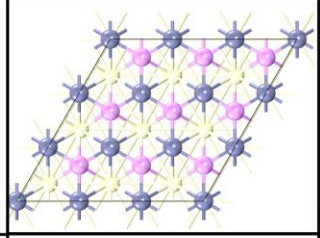	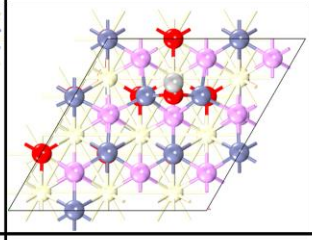	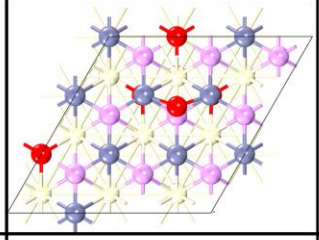	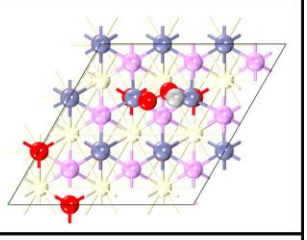
Side view	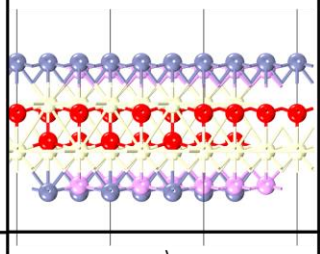	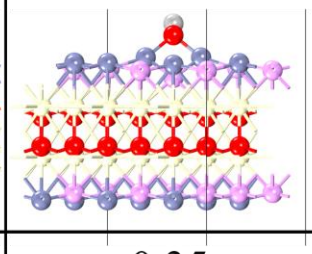	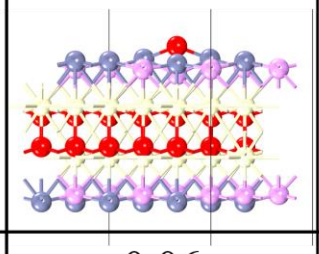	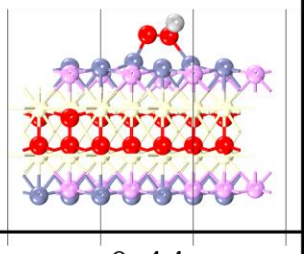
ΔZPE	\	0.35	0.06	0.44
ΔH	\	0.05	0.04	0.09
ΔTS	\	0.09	0.07	0.18
ΔG	\	0.04	1.22	3.12
PDS	O*→ OOH*		U_L(OER)	1.90

Fig. S53. Optimized structures and computed thermodynamic data (include ΔZPE, ΔH, ΔTS, and ΔG) of oxygen-containing species on the **CeZnPO** surface. The corresponding U_L value for **OER** is also shown.

	EuBrO	OH*	O*	OOH*
Top view	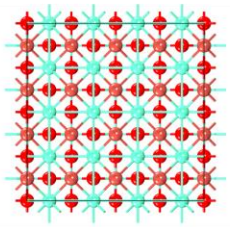	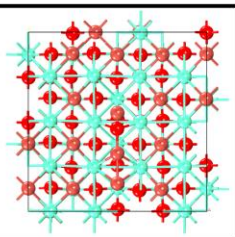	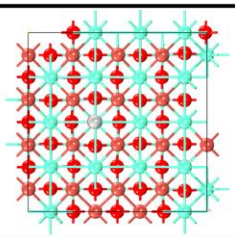	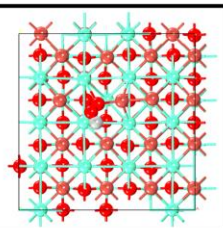
Side view	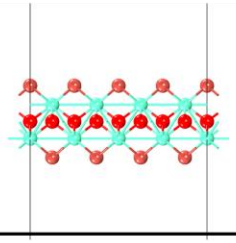	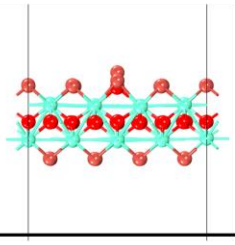	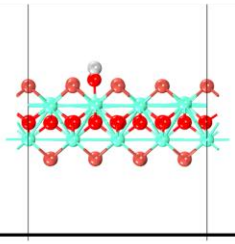	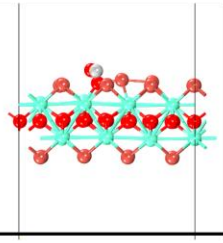
ΔZPE	\	0.32	0.07	0.44
ΔH	\	0.06	0.03	0.08
ΔTS	\	0.12	0.05	0.15
ΔG	\	1.88	1.92	3.74
PDS	$H_2O^* \rightarrow OH^*$		U_L(OER)	1.88

Fig. S54. Optimized structures and computed thermodynamic data (include ΔZPE, ΔH, ΔTS, and ΔG) of oxygen-containing species on the **EuBrO** surface. The corresponding U_L value for **OER** is also shown.

	TbBr	OH*	O*	OOH*
Top view	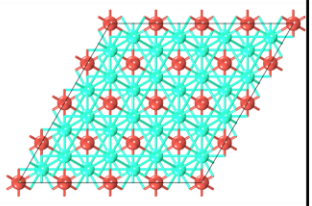	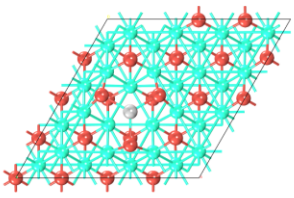	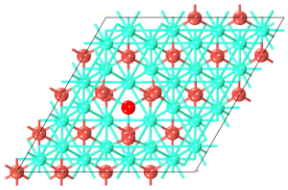	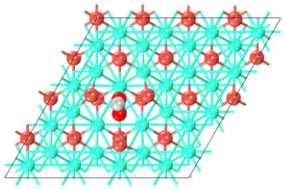
Side view	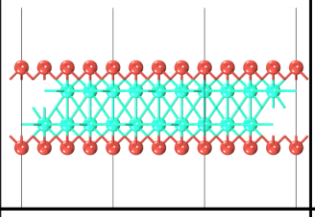	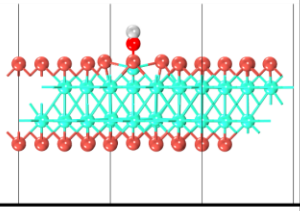	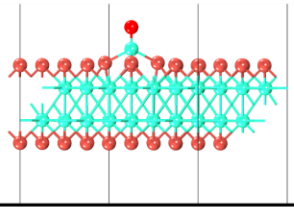	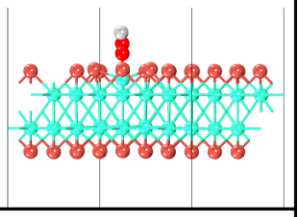
ΔZPE	\	0.33	0.06	0.43
ΔH	\	0.07	0.04	0.10
ΔTS	\	0.12	0.10	0.20
ΔG	\	0.56	2.18	4.03
PDS	O*→ OOH*		U_L(OER)	1.85

Fig. S55. Optimized structures and computed thermodynamic data (include ΔZPE, ΔH, ΔTS, and ΔG) of oxygen-containing species on the **TbBr** surface. The corresponding U_L value for **OER** is also shown.

	$CrGeTe_3$	OH*	O*	OOH*
Top view	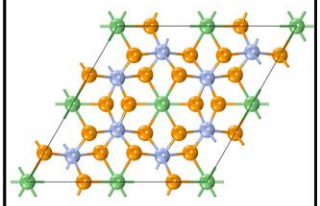	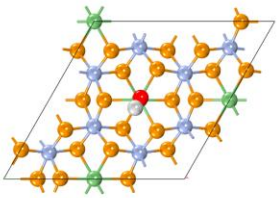	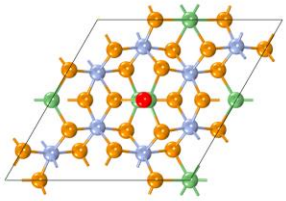	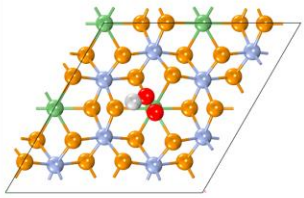
Side view	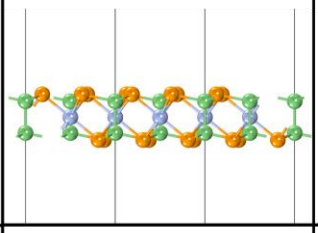	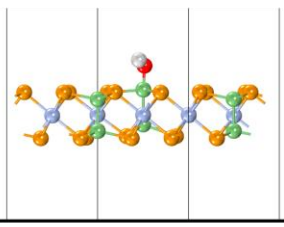	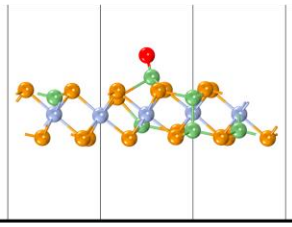	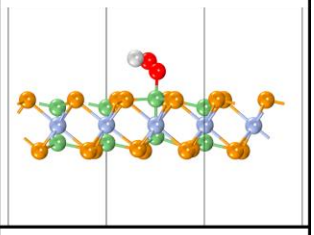
ΔZPE	\	0.34	0.06	0.43
ΔH	\	0.06	0.04	0.09
ΔTS	\	0.11	0.08	0.19
ΔG	\	0.86	2.45	4.10
PDS	O* → OOH*		**U_L(OER)**	1.64

Fig. S56. Optimized structures and computed thermodynamic data (include ΔZPE, ΔH, ΔTS, and ΔG) of oxygen-containing species on the **$CrGeTe_3$** surface. The corresponding U_L value for **OER** is also shown.

	$PtPb_4$	OH*	O*	OOH*
Top view	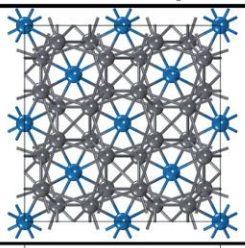	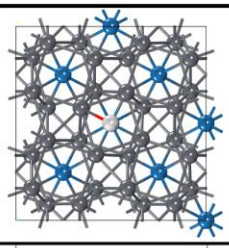	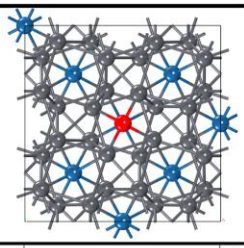	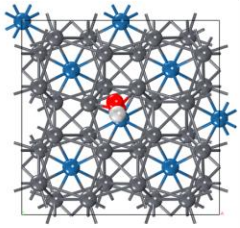
Side view	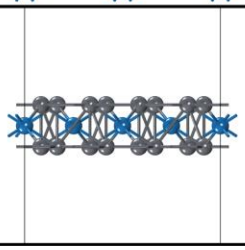	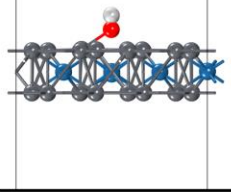	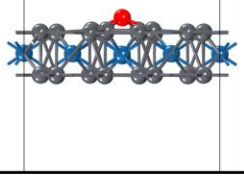	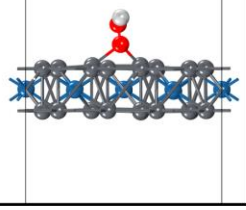
ΔZPE	\	0.30	0.02	0.41
ΔH	\	0.03	0.06	0.11
ΔTS	\	0.04	0.14	0.22
ΔG	\	0.65	1.83	3.65
PDS	O* → OOH*		**U_L(OER)**	1.82

Fig. S57. Optimized structures and computed thermodynamic data (include ΔZPE, ΔH, ΔTS, and ΔG) of oxygen-containing species on the **$PtPb_4$** surface. The corresponding U_L value for **OER** is also shown.

	$CuH_2(SeO_3)_2$	OH*	O*	OOH*
Top view	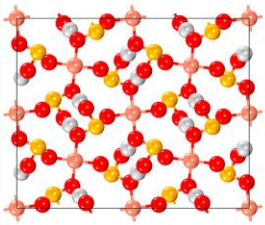	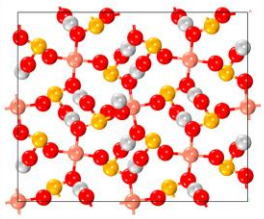	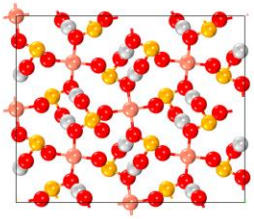	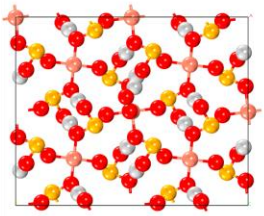
Side view	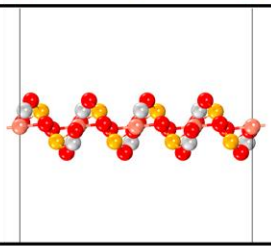	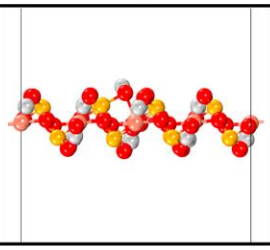	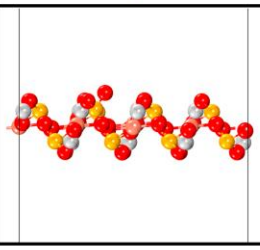	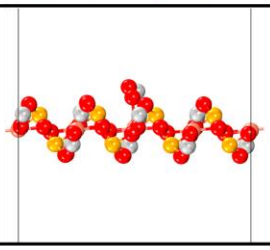
ΔZPE	\	0.35	0.08	0.42
ΔH	\	0.05	0.03	0.10
ΔTS	\	0.08	0.05	0.21
ΔG	\	1.77	2.50	4.20
PDS	$H_2O \rightarrow OH^*$		**U_L(OER)**	1.77

Fig. S58. Optimized structures and computed thermodynamic data (include ΔZPE, ΔH, ΔTS, and ΔG) of oxygen-containing species on the **$CuH_2(SeO_3)_2$** surface. The corresponding U_L value for **OER** is also shown.

	$Ag(AuS)_2$	OH*	O*	OOH*
Top view	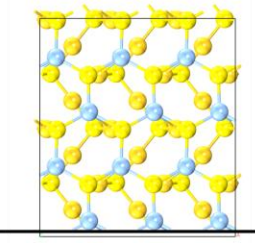	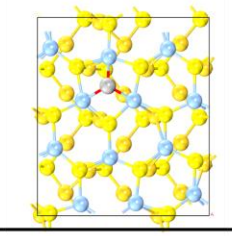	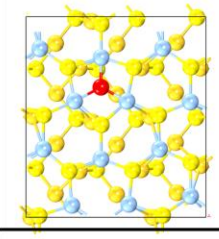	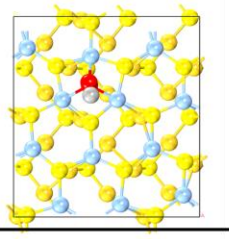
Side view	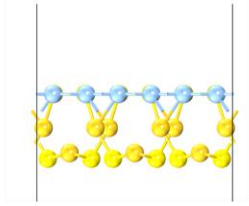	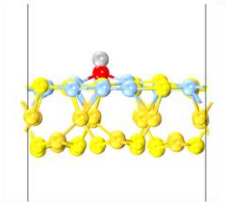	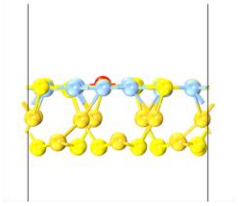	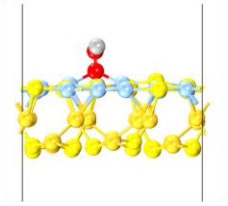
ΔZPE	\	0.36	0.06	0.43
ΔH	\	0.05	0.03	0.10
ΔTS	\	0.08	0.05	0.19
ΔG	\	1.01	2.34	4.16
PDS	O*→ OOH*		**U_L(OER)**	1.82

Fig. S59. Optimized structures and computed thermodynamic data (include ΔZPE, ΔH, ΔTS, and ΔG) of oxygen-containing species on the **$Ag(AuS)_2$** surface. The corresponding U_L value for **OER** is also shown.

	Nb_9IrSe_{20}	OH*	O*	OOH*
Top view	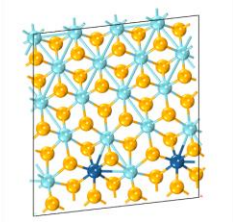	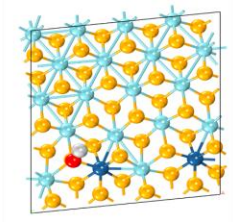	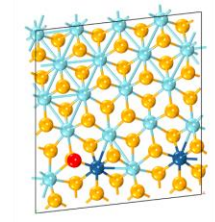	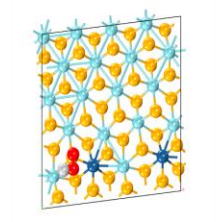
Side view	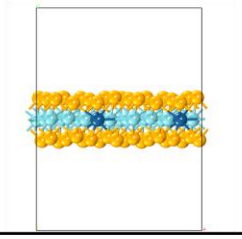	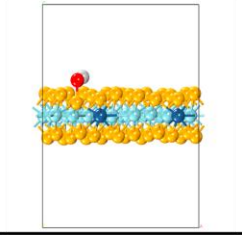	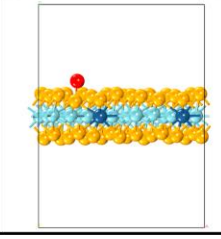	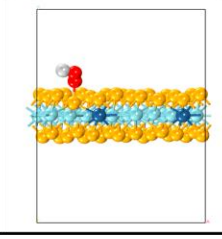
ΔZPE	\	0.35	0.06	0.44
ΔH	\	0.06	0.04	0.09
ΔTS	\	0.06	0.07	0.20
ΔG	\	0.93	2.27	4.19
PDS	OOH* →O*		**U_L(OER)**	1.91

Fig. S60. Optimized structures and computed thermodynamic data (include ΔZPE, ΔH, ΔTS, and ΔG) of oxygen-containing species on the **Nb_9IrSe_{20}** surface. The corresponding U_L value for **OER** is also shown.

	$AgHO_2$	OH*	O*	OOH*
Top view	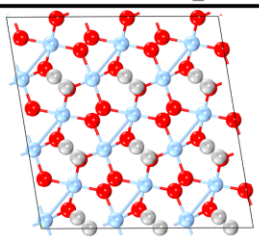	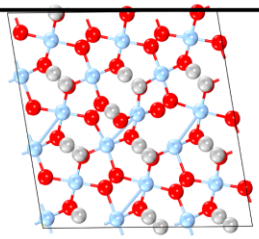	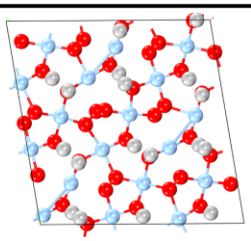	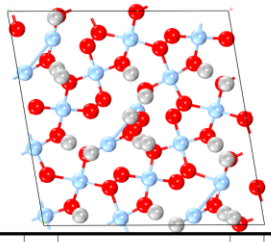
Side view	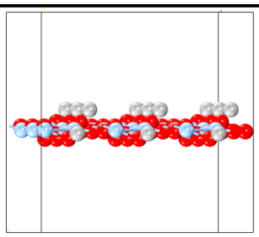	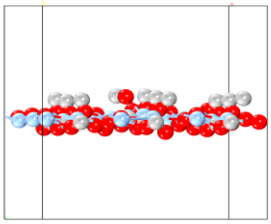	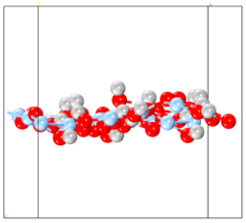	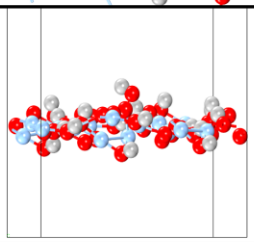
ΔZPE	\	0.34	0.08	0.42
ΔH	\	0.06	0.03	0.10
ΔTS	\	0.11	0.04	0.21
ΔG	\	1.21	2.38	3.70
PDS	O* → OOH*		**U_L(OER)**	1.32

Fig. S61. Optimized structures and computed thermodynamic data (include ΔZPE, ΔH, ΔTS, and ΔG) of oxygen-containing species on the **$AgHO_2$** surface. The corresponding U_L value for **OER** is also shown.

	La_2PI_2	OH*	O*	OOH*
Top view	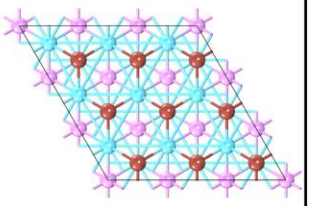	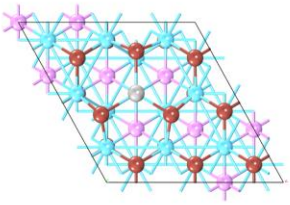	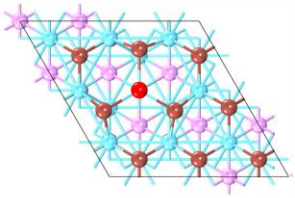	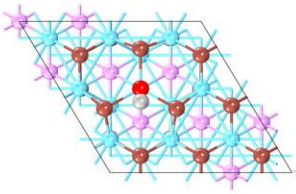
Side view	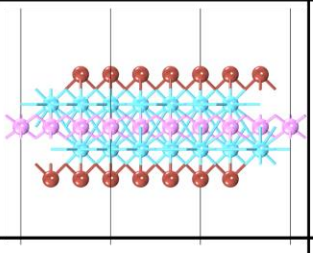	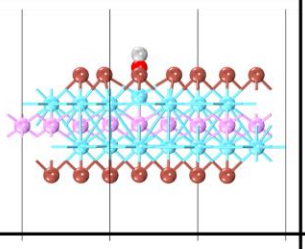	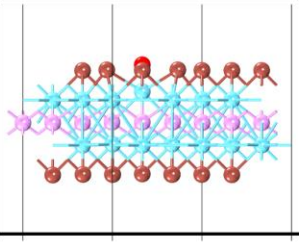	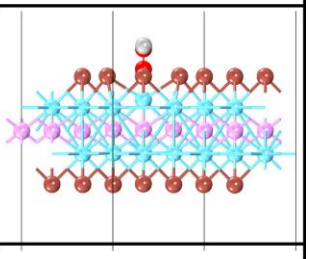
ΔZPE	\	0.33	0.06	0.43
ΔH	\	0.06	0.04	0.08
ΔTS	\	0.10	0.07	0.16
ΔG	\	0.87	2.37	4.28
PDS	O* → OOH*		**U_L(OER)**	1.91

Fig. S62. Optimized structures and computed thermodynamic data (include ΔZPE, ΔH, ΔTS, and ΔG) of oxygen-containing species on the **La_2PI_2** surface. The corresponding U_L value for **OER** is also shown.

	TbGaI	OH*	O*	OOH*
Top view	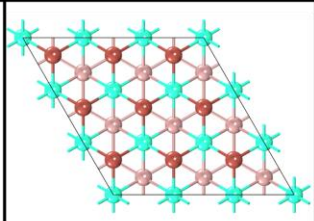	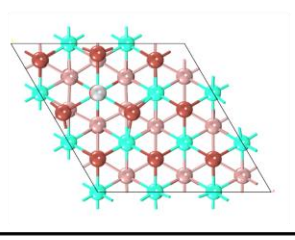	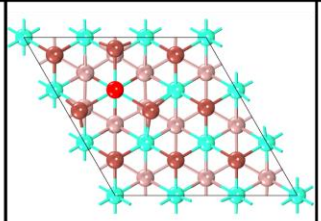	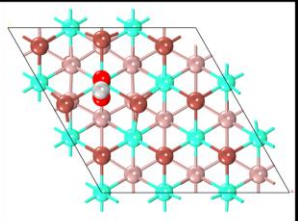
Side view	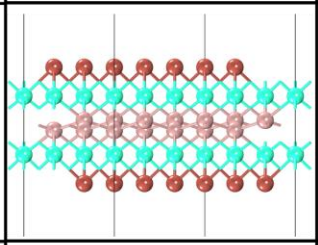	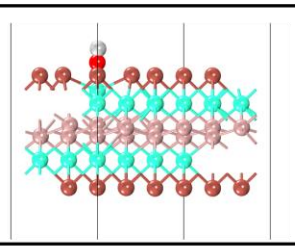	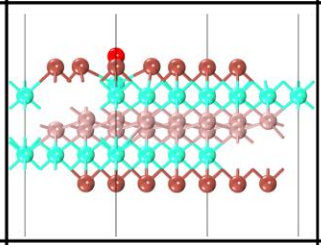	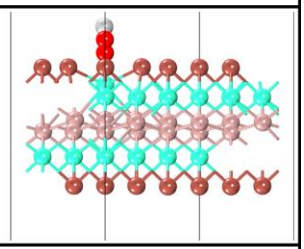
ΔZPE	\	0.31	0.06	0.43
ΔH	\	0.07	0.04	0.09
ΔTS	\	0.14	0.08	0.17
ΔG	\	0.85	2.71	4.24
PDS	OH* → O*		U_L(OER)	1.85

Fig. S63. Optimized structures and computed thermodynamic data (include ΔZPE, ΔH, ΔTS, and ΔG) of oxygen-containing species on the **TbGaI** surface. The corresponding U_L value for **OER** is also shown.

	CeI_3	OH*	O*	OOH*
Top view	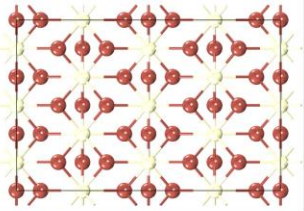	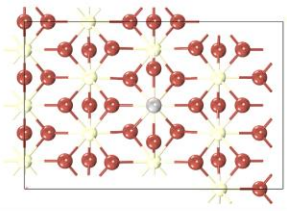	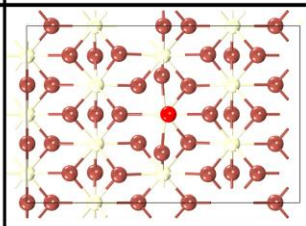	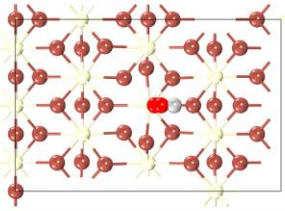
Side view	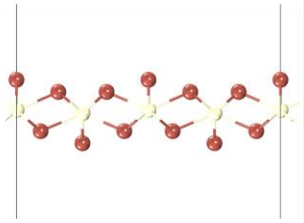	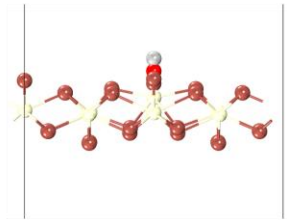	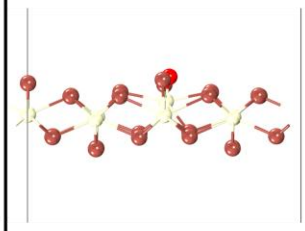	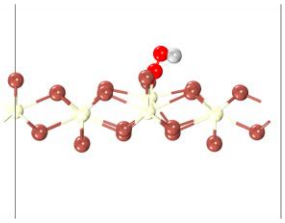
ΔZPE	\	0.33	0.04	0.44
ΔH	\	0.06	0.03	0.09
ΔTS	\	0.11	0.03	0.18
ΔG	\	0.79	1.44	3.29
PDS	O*→ OOH*		**U_L(OER)**	1.85

Fig. S64. Optimized structures and computed thermodynamic data (include ΔZPE, ΔH, ΔTS, and ΔG) of oxygen-containing species on the **CeI_3** surface. The corresponding U_L value for **OER** is also shown.

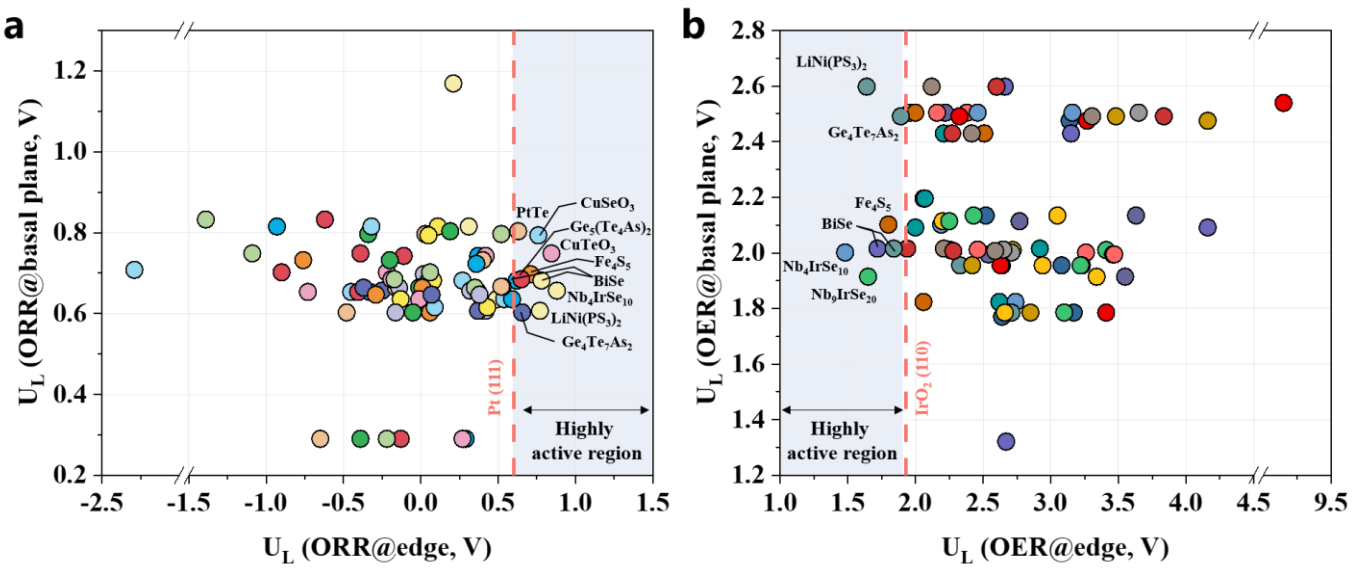

Fig. S65. Theoretical limiting potential (U_L) of ORR (a) and OER(b) on 77 edge surfaces in comparison with the potential on the basal planes.

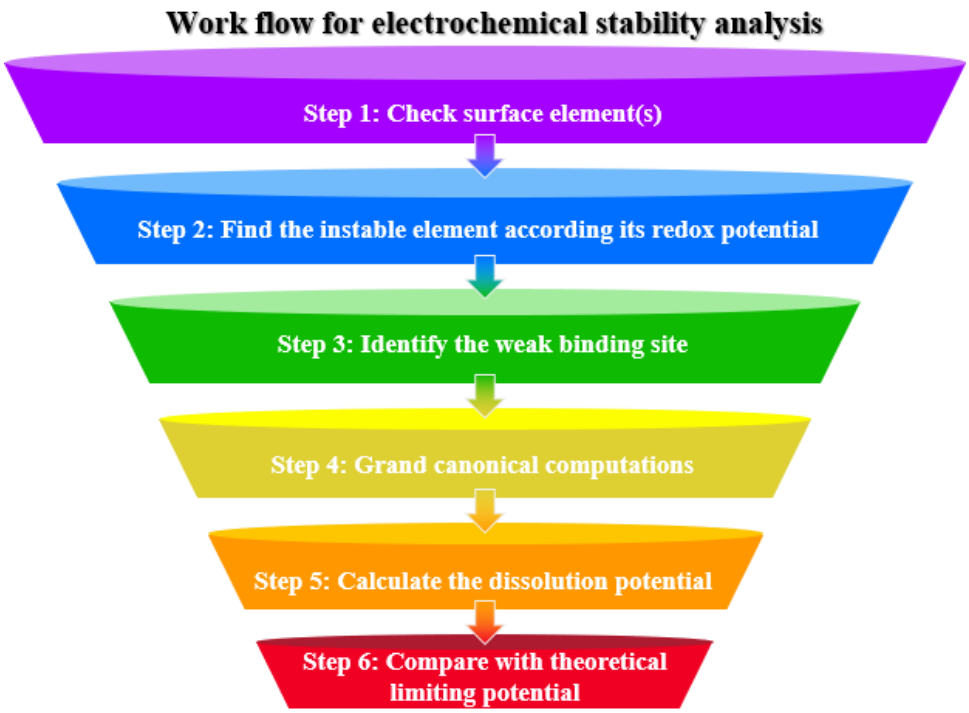

Fig. S66. Work flow for electrochemical stability analysis.

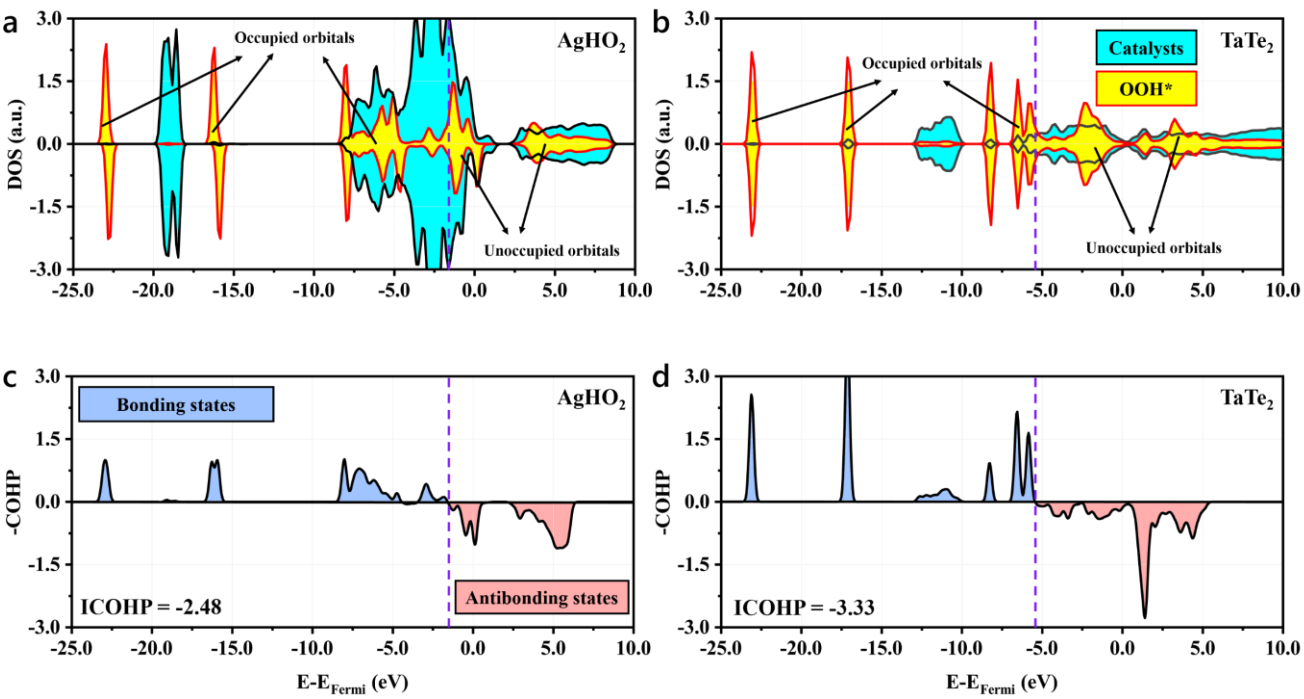

Fig. S67. Density of states (DOS) and the crystal orbital Hamilton populations (COHP) of the OOH* adsorbed on the active sites of $AgHO_2$ (a and c), and $TaTe_2$ (b and d). The results indicate that both of the two catalysts can strongly interact with the OOH* via band hybridization. Upon adsorption, OOH* can form the fully occupied orbitals below the Fermi level and partial occupied molecular orbitals around the Fermi level. By comparison with the $AgHO_2$, $TaTe_2$ can downshift the molecular orbitals of OOH* toward a lower energy level, which results in a stronger binding. The bonding states or the occupied orbitals between the OOH* and $TaTe_2$ are all distributed below the -5.97 eV, much lower than that in the $AgHO_2$ (-2.19 eV). Specifically, through integrating the COHP up to the Fermi level, the different band hybridization can be further unveiled. In principle, a more negative value of integrated-COHP (ICOHP) generally implies a stronger binding. The calculated ICOHP value on the $TaTe_2$ (-3.33 eV) is more negative than that of -2.48 eV on the $AgHO_2$, which is consistent with the trend of adsorption free energy calculations (3.55 eV for the $TaTe_2$ vs 3.70 eV for the $AgHO_2$). Notably, the ideal situation for the oxygen electrocatalysis is that the Gibbs free energy changes in each elementary step are the same at zero potential so that potential barriers of each step can be zero when the electrode potential reaches the equilibrium potential. Thus, the optimal ΔG(OOH*) value is estimated at 3.69 eV (4.92 – 1.23 = 3.69). Since the $AgHO_2$ has a nearly ideal ΔG(OOH*) of 3.69 eV, the $AgHO_2$ is predicted to have a better performance for the OER than the $TaTe_2$.

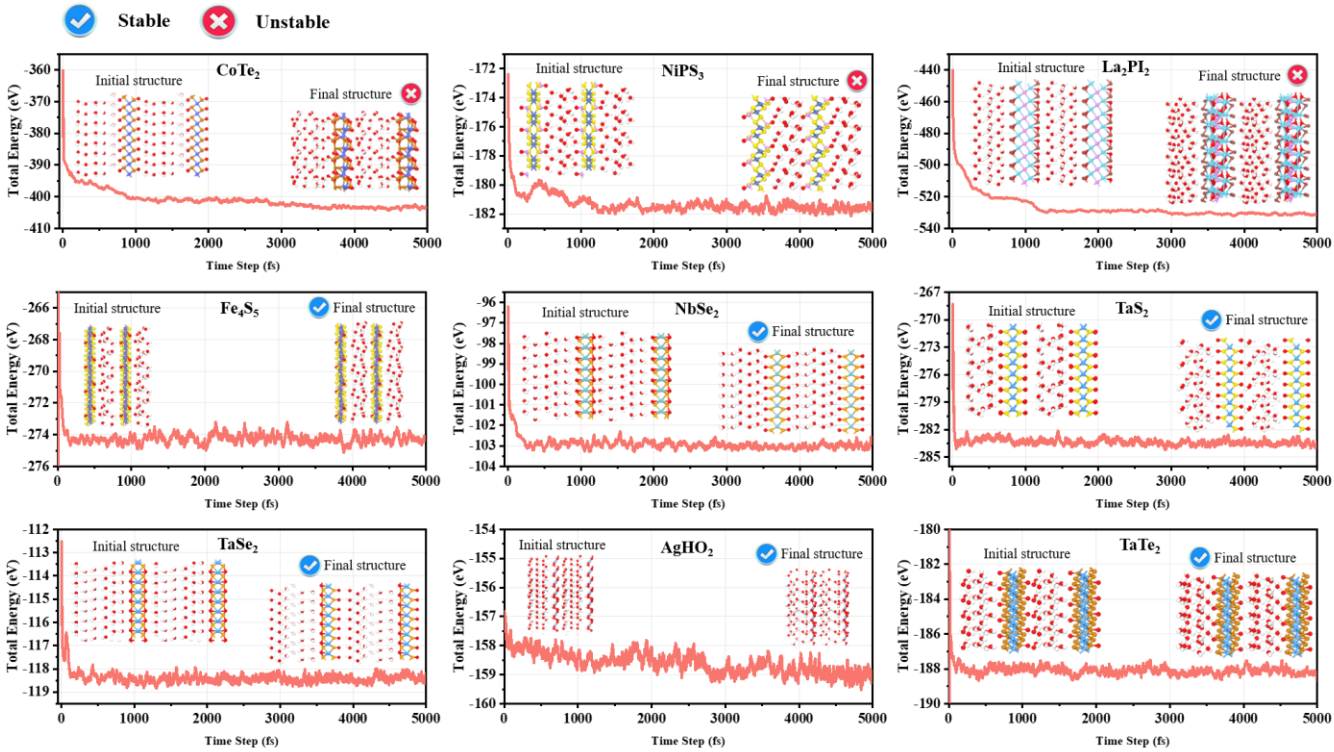

Fig. S68. Energy profiles along 5 ps AIMD simulation for the two benchmark materials of $CoTe_2$ and $NiPS_3$, and nine typical compounds which screened from dissolution potential analysis. A canonical ensemble was simulated using the algorithm of Nosé. The temperature was set at 300K.

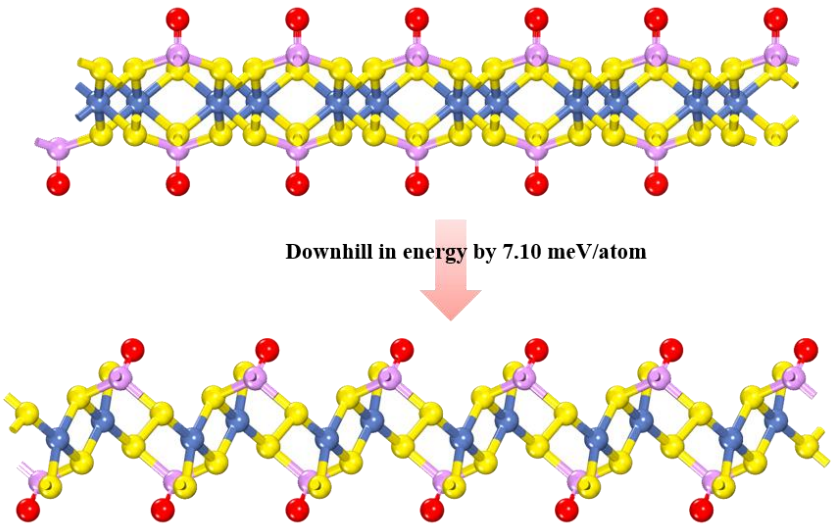

Fig. S69. Oxygen adsorption induced structure change for the $NiPS_3$ during the MD simulation.

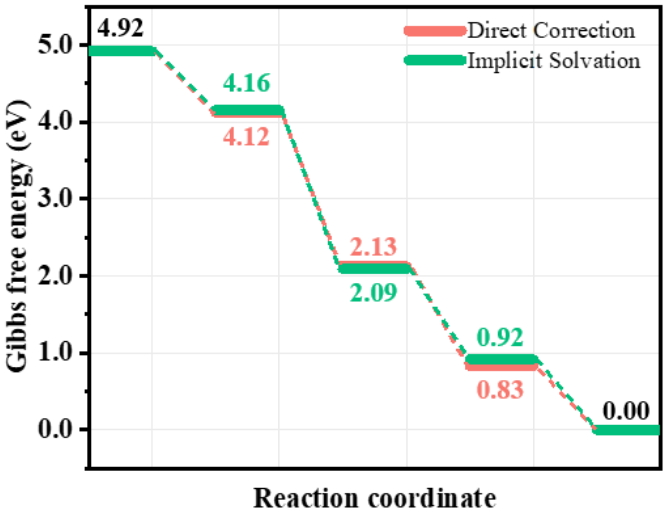

Fig. S70. Comparison of energy profiles of ORR on the $NbSe_2$ obtained from the direct correction and implicit solvation model.

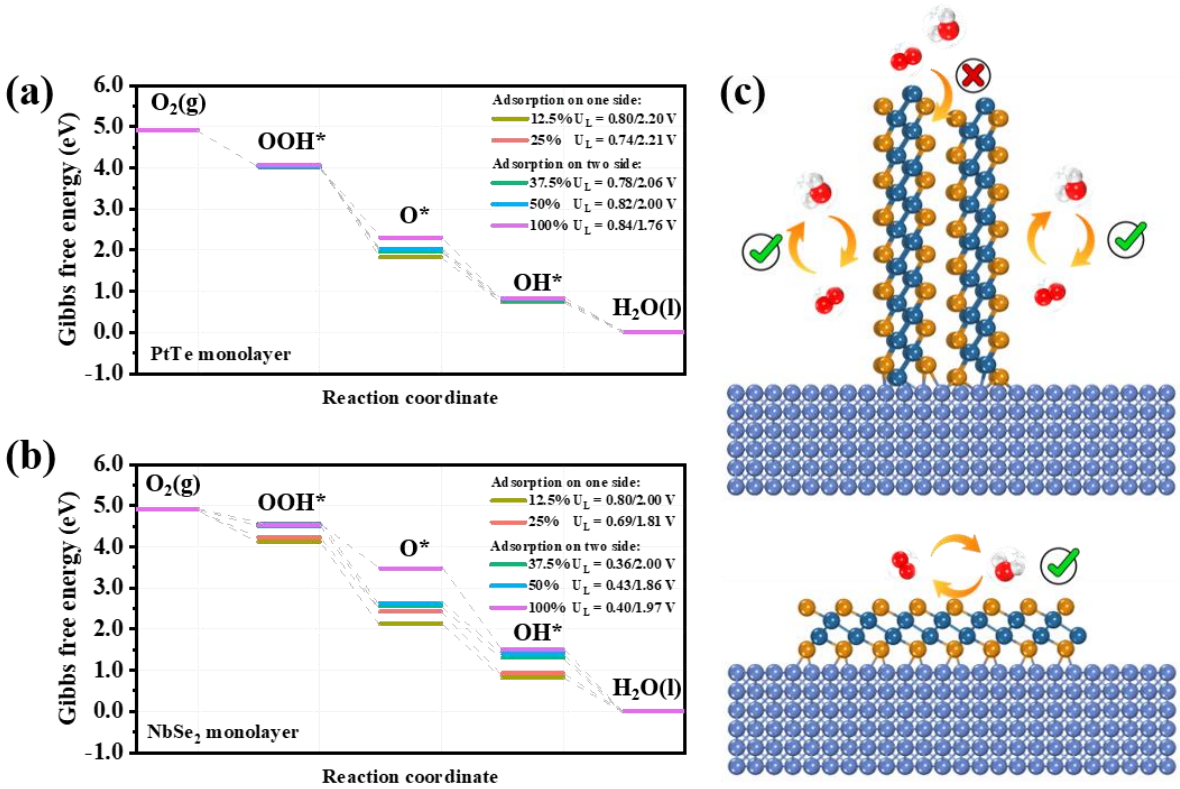

Fig. S71. Reaction pathway and theoretical limiting potential (U_L) of ORR/OER on PtTe (a) and $NbSe_2$ monolayers (b) at different coverage conditions. (c) Schematic illustration of the contact models of 2D materials on catalytic substrates.

References

1. J. P. Perdew, K. Burke and M. Ernzerhof, *Phys. Rev. Lett.*, 1996, **77**, 3865.
2. P. E. Blochl, *Phys. Rev. B*, 1994, **50**, 17953-17979.
3. V. Wang, N. Xu, J.-C. Liu, G. Tang and W.-T. Geng, *Comput. Phys. Commun.*, 2021, **267**, 108033.
4. S. Grimme, *J. Comput. Chem.*, 2006, **27**, 1787-1799.
5. G. K. H. Madsen and D. J. Singh, *Comput. Phys. Commun.*, 2006, **175**, 67-71.
6. T. Stauber, N. M. R. Peres and F. Guinea, *Physical Review B*, 2007, **76**, 205423.
7. J. K. Nørskov, J. Rossmeisl, A. Logadottir, L. Lindqvist, J. R. Kitchin, T. Bligaard and H. Jónsson, *J. Phys. Chem. B*, 2004, **108**, 17886-17892.
8. J. D. Goodpaster, A. T. Bell and M. Head-Gordon, *J. Phys. Chem. Lett.*, 2016, **7**, 1471-1477.
9. H. Xiao, T. Cheng, W. A. Goddard and R. Sundararaman, *J. Am. Chem. Soc.*, 2016, **138**, 483-486.
10. X. Guo, S. Lin, J. Gu, S. Zhang, Z. Chen and S. Huang, *ACS Catal.*, 2019, **9**, 11042-11054.
11. H. Xu, D. Cheng, D. Cao and X. C. Zeng, *Nat. Catal.*, 2018, **1**, 339-348.
12. F. Calle-Vallejo, J. I. Martinez and J. Rossmeisl, *Phys Chem Chem Phys*, 2011, **13**, 15639-15643.
13. K. Mathew, R. Sundararaman, K. Letchworth-Weaver, T. A. Arias and R. G. Hennig, *J. Chem. Phys.*, 2014, **140**, 084106.
14. R. Sundararaman, K. Letchworth-Weaver, K. A. Schwarz, D. Gunceler, Y. Ozhabes and T. A. Arias, *SoftwareX*, 2017, **6**, 278-284.
15. K. F. Garrity, J. W. Bennett, K. M. Rabe and D. Vanderbilt, *Comput. Mater. Sci*, 2014, **81**, 446-452.
16. R. Sundararaman and W. A. Goddard, *J. Chem. Phys.*, 2015, **142**, 064107.
17. R. Sundararaman, W. A. Goddard and T. A. Arias, *J. Chem. Phys.*, 2017, **146**, 114104.
18. Z. Duan and G. Henkelman, *ACS Catalysis*, 2021, **11**, 14439-14447.
19. C. Seitz Linsey, F. Dickens Colin, K. Nishio, Y. Hikita, J. Montoya, A. Doyle, C. Kirk, A. Vojvodic, Y. Hwang Harold, K. Norskov Jens and F. Jaramillo Thomas, *Science*, 2016, **353**, 1011-1014.
20. Z. Wang, X. Guo, J. Montoya and J. K. Nørskov, *npj Comput. Mater.*, 2020, **6**, 160.
21. H. Xiao, T. Cheng and W. A. Goddard, *J. Am. Chem. Soc.*, 2017, **139**, 130-136.
22. J. C. Liu, H. Xiao and J. Li, *J. Am. Chem. Soc.*, 2020, **142**, 3375-3383.
23. G. Henkelman, B. P. Uberuaga and H. Jónsson, *J. Chem. Phys.*, 2000, **113**, 9901-9904.
24. A. M. Patel, S. Vijay, G. Kastlunger, J. K. Nørskov and K. Chan, *J. Phys. Chem. Lett.*, 2021, **12**, 5193-5200.
25. L. Bornstein, *Subvolume A, Pure Substances (Springer, 1999)*, 1999.

26. D. C. Harris, *Quantitative chemical analysis*, Macmillan, 2010.

27. D. R. Lide, *CRC handbook of chemistry and physics*, CRC press, 2004.

27. M. O. Almeida, M. J. Kolb, M. R. V. Lanza, F. Illas and F. Calle-Vallejo, *ChemElectroChem*, 2022, **9**, e202200210.

28. J. A. Gauthier, C. F. Dickens, L. D. Chen, A. D. Doyle and J. K. Nørskov, *J. Phys. Chem. C* 2017, **121,** 11455–11463.

29. D. Y. Kuo, J. K. Kawasaki, J. N. Nelson, J. Kloppenburg, G. Hautier, K. M. Shen, D. G. Schlom and J. Suntivich, *J. Am. Chem. Soc.*, 2017, **139**, 3473-3479.